Reactive nitrogen in the troposphere

Christopher Paul Reed

PhD

University of York

Chemistry

May 2017

Abstract

The remote marine boundary layer at the tropics represents a baseline condition for the Earth's atmosphere. Air in these regions has typically not encountered emissions for days to weeks and thus has been subject only to processing; that is degradation and reaction of species in the air. Understanding the most basic chemistry occurring in the remote marine boundary layer is fundamental to our overall understanding of the atmosphere as a whole.

The source and manifestation of nitrogen oxides, NO_x, in the remote marine boundary layer at the Cape Verde observatory and elsewhere has been intriguing. NO_x observations could often not be reconciled easily with known chemistry. This, when coupled to the difficulty in measuring the very low concentrations present has led to various speculative theories which are thus-far unsubstantiated.

By carefully characterising the NO_2 photolysis–NO chemiluminescence technique for artefacts, interferences, and uncertainties the applicability and limitations of the technique were established. It was found that peroxyacyl nitrates cause an interference of $\sim 5\,\%$ which can lead to significant errors in NO_2 determination, especially in cold or high altitude environments but are insignificant in the remote marine boundary layer at Cape Verde.

Using two years of data collected at Cape Verde and a 0-D model of tropospheric chemistry the budget of NO_x was estimated. Evidence that nitric acid deposited on aerosol, previously thought to be the terminating step in the cycle of NO_x, is able to be released back to the atmosphere as NO_2 and HONO has been shown. This 'renoxification' process likely represents the dominant source of NO_x in the tropical marine boundary layer, counter to previous theory of long range transport of reactive nitrogen species.

The implication of these findings changes our fundamental understanding of NO_x sources and sinks in the remote troposphere. Moreover, by understanding the limitations of NO_2 measurement techniques allows for easier interpretation of sometimes puzzling data without the need for unprovable mechanisms. Additionally, a new technique for quantifying atmospheric HONO was developed by exploiting the limitations of photolytic NO_2 measurement and photolysing differentially at two different wavelengths.

All measurements are wrong, some measurements are useful!

Contents

List of Figures

List of Tables

Declaration

I declare that this thesis is a presentation of original work and I am the sole author. This work has not previously been presented for an award at this, or any other, University. The research described in this thesis is original work, which was undertaken at the University of York during 2013–2016. Except where stated, all of the work contained within this thesis represents the original contribution of the author. Some parts of this thesis have been published in journals; where items were published jointly with collaborators, the author of this thesis is responsible for the material presented here. For each published item the primary author is the first listed author. Publications are listed at the beginning of the chapter to which they relate. All sources are acknowledged as References.

This study was supported by the National Centre for Atmospheric Science (NCAS).

Chapter 1

Introduction

''Look deep into nature, and then you will understand everything better."

Albert Einstein

The chemistry and dynamics of the atmosphere represent an incredibly complex interconnected system. Despite, or because of this intricacy and the atmosphere's inexorable connection with life we study it's structure, composition, and dynamics so that we can better understand how it operates to provide a habitable environment. Although the atmosphere consists of many facets and layers it is the chemistry of the bottom-most portion which contains 75 % of the total mass, and which we inhabit, that concerns this work: this is the troposphere. This chapter provides background to the chemistry of the troposphere, namely NO_x, O_3, and halogen interactions.

After discussing the background science for this thesis, this chapter presents the goals of this work (Sect. 1.5), and concludes with a brief description of the content of the following chapters within this thesis (Sect. 1.6).

1.1 The atmosphere

The chemistry, composition, and climate of the atmosphere of the Earth holds interest, and causes concern, for a great many people. Without an atmosphere, planet Earth would not sustain life (as we know it). The atmosphere forms part of the geosphere; the collection of distinct, but not separate, environments occupying a 150 km thick shell around the planet. Extending from the Karman line 100 km above the ground marking the edge of space, to the deepest point reached by humans beings – a 12.2 km deep borehole. The atmosphere – containing the gases – *atmos* coming from Greek for vapour, is joined by the hydrosphere – containing the water; the cryosphere – where it is cold, namely at the poles; and the lithosphere – containing the rock, practically this is the crust.

Squeezed somewhere between the interface of these four environments exists a thin layer of life we refer to as the biosphere. Encompassing everything from moss growing on the shady side of a tree in the remote jungle, to the zooplankton eaten by deep-sea lantern fish, to human beings, the biosphere interacts with, and depends upon the four other spheres. The atmosphere itself is stratified into several distinct layers; thermosphere, mesosphere, stratosphere, and troposphere which are depicted in Fig. 1.1.

In regards to the interaction of the biosphere and atmosphere we are mostly concerned with the atmosphere immediately affecting, and being affected by the biosphere. This lower-most layer of the atmosphere is termed the troposphere – *tropos* coming from the Greek for change due to the turbulence with this layer driven by differential heating from the sun. It is the troposphere which contains $\sim 75\,\%$ of the mass of the atmosphere (Barry et al., 2009), where the majority of weather occurs, and where the entire biosphere resides. The troposphere is also where all emission into the atmosphere originates, where, driven by solar flux, the most complex chemistry is found.

Much is known about the chemistry of the atmosphere from the effect of injecting halogens into the stratosphere on ozone to the diurnal cycle of CO_2 driven by oxidation. Whilst the general picture of how chemicals interact in the atmopshere is known there remain gaps in our understanding. What drives the diurnal cycle of NO_x and O_3 in the remote marine boundary layer at Cape Verde. The O_3 diel cycle was found to be driven by halogen oxide chemistry (Read et al., 2008), but despite the relationship between NO_x and O_3

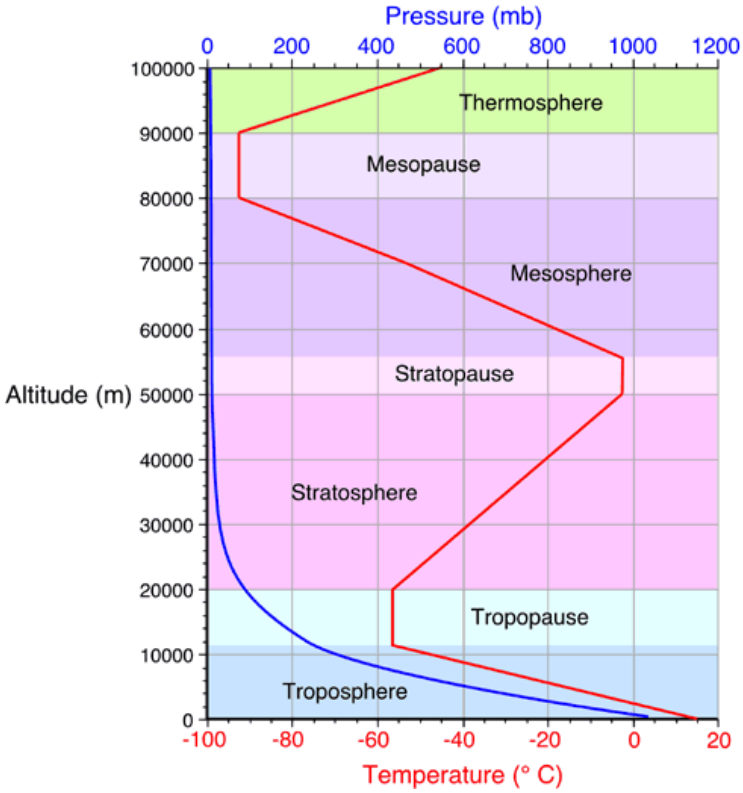

Figure 1.1 – Generalised vertical structure of the atmosphere showing how the various layers are arranged, as well as the pressure and temperature profile (lapse rate) through them.

the source and variability of NO_x still cannot be reconciled through modelling and long term observations. This is not only true for Cape Verde but for the Antarctic (Bauguitte et al., 2012) and Tazmania (Monks et al., 1998). Similarly global models such as GEOS-chem had failed to simulate O_3 well due to our lack of understanding of halogen chemistry until only recently (Sherwen et al., 2016a,b) whilst constraints on reaction rates and poor (Simpson et al., 2015) and new reactions are being proposed (Saiz-Lopez et al., 2016).

1.2 Tropospheric chemistry

The oxidising capacity of the atmosphere is the rate of the self-cleansing process whereby emissions are oxidized by oxidants (such as the hydroxyl radical; OH, or ozone) into water soluble species and eventually removed. The hydroxyl radical is often referred to as the detergent of the atmosphere (Li et al., 2008) due to its reactivity and is considered the most important oxidant in the troposphere. Ozone (O_3), being the main precursor to OH

is considered to be the second most.

$$O_3 + h\nu\,(<320\,nm) \rightarrow O(^1D) + O_2 \tag{1.1}$$

$$O(^1D) + H_2O \rightarrow 2\,OH \tag{1.2}$$

Photolysis of O_3 to form $O(^1D)$ (reaction 1.1) and the subsequent reaction of $O(^1D)$ with water vapour (1.2) results in the formation of two hydroxyl radicals and is the primary source of OH radicals in the troposphere (Levy, 1971; Logan et al., 1981). In the stratosphere O_3 is formed by direct photolysis of molecular oxygen forming atomic oxygen by absorption of an ultra-violet (UV) photon (242 nm, Matsumi and Kawasaki 2003) shown in reactions 1.3 to 1.6 which are referred to as the *Chapman cycle*. This forms the famous 'ozone layer' which prevents harmful high energy UV radiation from reaching the ground.

$$O_2 + h\nu\,(<242\,nm) \rightarrow 2\,O \tag{1.3}$$

$$O + O_2 + M \rightarrow O_3 + M \tag{1.4}$$

$$O_3 + h\nu\,(<310\,nm) \rightarrow O(^1D) + O_2 \tag{1.5}$$

$$O + O_3 \rightarrow 2\,O_2 \tag{1.6}$$

In the troposphere these short wavelengths of light are already filtered out by O_3 and O_2 higher up in the atmosphere so O_3 cannot be formed directly. In the troposphere O_3 is formed by secondary reactions of nitrogen oxides. The marine boundary layer is characterised by relatively low ozone levels due to the greater number of ozone sinks than sources (Cooper et al., 2014), impacting OH concentrations. Changes in ozone sources and sinks therefore mediate CH_4 and CO lifetimes, CH_4 being a potent greenhouse gas and CO being an indirect greenhouse gas perturbing OH-CH_4-O_3 chemistry (Isaksen and Hov, 1987). Therefore, understanding the budget of NO_x in the remote boundary layer is important to our understanding of the wider climate.

1.2.1 NO_x chemistry

Nitrogen oxides, NO and NO_2, collectively termed NO_x, are reactive trace gases emitted into the atmosphere by combustion processes, lightning, and soil bacteria. Combustion, namely burning of fossil fuels accounts for the majority (Jaeglé et al., 2005) of emissions. NO and NO_2 are grouped together as NO_x due to their rapid inter-conversion on a time-scale of around 5 minutes in the troposphere.

Photolysis of NO_2 to NO + O(^{3}P) (1.7) is the fundamental reaction for formation of tropospheric ozone (O_3) in reaction (1.8) where M may typically be N_2 or O_2 (Kley et al., 1981).

$$NO_2 + h\nu\,(<410\,nm) \rightarrow NO + O(^3P) \tag{1.7}$$

$$O_2 + O(^3P) + M \rightarrow O_3 + M \tag{1.8}$$

With the inclusion of reaction 1.9 (an ozone destruction step) reactions 1.7 and 1.8 form a null cycle (Kley et al., 1981).

$$O_3 + NO \rightarrow O_2 + NO_2 \tag{1.9}$$

NO_x is removed from the atmosphere during day-time by reaction with OH forming nitric acid (HNO_3). Formation of nitric acid was traditionally seen as a permanent sink for NO_x as subsequent scavenging by precipitation (wet deposition), or uptake by surfaces (dry deposition) is a permanent sink.

During night-time NO_x is removed by reaction of NO_2 with O_3 forming the nitrate radical NO_3 (1.10) the oxidation chemistry of which is discussed in Sect. 1.2.4. NO_3 forms dinitrogen pentoxide (N_2O_5) by reaction with NO_2, acting as a reservoir species for NO_x (reaction 1.11).

$$NO_2 + O_3 \rightarrow NO_3 + O_2 \tag{1.10}$$

$$NO_3 + NO_2 \rightleftharpoons N_2O_5 \tag{1.11}$$

The formation of N_2O_5 can act as a sink for NO_x by its uptake and subsequent hydrolysis on surfaces to HNO_3 (1.12, Mogili et al. 2006; Riemer et al. 2003) whereby it is either removed from the atmosphere, or photolysed back as HONO and NO_2 as described below in section 1.2.1.1 and in chapter 4.

$$N_2O_{5(ads)} + H_2O \rightarrow 2\,HNO_{3(ads)} \tag{1.12}$$

Further sinks of NO_x are reaction with halogen oxides forming halogen nitrates and is discussed in Sect. 1.2.5 as well as in chapter 4.

1.2.1.1 Renoxification

Recently the possibility of renoxification of the atmopshere by photolysis of aerosol nitrate has been proposed (Ndour et al., 2009; Ye et al., 2016b). Aerosol nitrate has been found

to be photolysed at rates up to ~ 3 orders of magnitude higher than for gas phase nitric acid producing HONO and NO_2 in a characteristic ratio $x : y$ (Reaction 1.13), with that ratio possibly being highly dependent on aerosol pH or hydrocarbon concentration (Ye et al., 2017). Similarly the rate of photolysis is seemingly surface specific also (Ye et al., 2016a)

$$p\text{-}NO_3 + h\nu \rightarrow x\text{HONO} + yNO_2 \tag{1.13}$$

Nitrate photolysis introduces a net source of NO_x via NO_2 and HONO in environments that may be far from other sources of direct emission. In chapter 4 renoxification by nitrate photolysis is tested against observations in the remote marine boundary layer at the Caper Verde Atmospheric Observatory (CVO) using a box model to simulate the NO, NO_2, HONO, O_3, IO, and BrO observations.

1.2.1.2 NO_y chemistry

Odd nitrogen (NO_y) refers to the sum of NO, NO_2 and their oxidation products which are ether emitted directly (e.g. HONO) or form through secondary reaction in the atmosphere. Nitric acid, nitrous acid, the nitrate radical, dinitrogen pentoxide etc. are all classed as NO_y, as are organic nitrate species such as peroxyacetyl nitrate. Organic nitrates are formed by reaction of a peroxy or alkoxy radical with NO_2, which are an intermediate in volatile organic compound (VOC) oxidation as described in Sect. 1.2.2 e.g. reaction 1.18.

$$CH_3CHO + OH \rightarrow CH_3CO + H_2O \tag{1.14}$$

$$CH_3CO + O_2 \rightarrow CH_3C(O)OO \tag{1.15}$$

$$CH_3C(O)OO + NO_2 \rightleftharpoons CH_3COO_2NO_2 \tag{1.16}$$

Reactions 1.14, 1.15, and 1.16 show the mechanism by which peroxyacetyl nitrate (PAN) forms as a product of acetaldehyde (CH_3CHO) oxidation by OH. The organic nitrates formed by these, and analogous reactions, fall into classes of compounds known as alkyl nitrates; ANs, with the general structure $RONO_2$, and peroxyalkyl nitrates; PNs, with the general structure $ROONO_2$. Organic NO_y species act as a reservoir for NO_x in the upper troposphere–lower stratosphere (UTLS) due to their being in thermal equilibrium with NO_2 i.e. reaction 1.16 (Singh et al., 1985, 1995). In the low temperatures of the UTLS the lifetime of ANs and PNs can be long, whereas at the surface their instability to thermal

decomposition means that it is much shorter. For example, the lifetime of PAN is 30 min at 25 °C (Bridier et al., 1991) but is 5.36 years at − 26 °C (Kleindienst, 1994). This way organic NO_y which is formed as a secondary pollutant in the boundary layer and lofted to the UTLS can be transported to the tropics where warming in descending air causes the NO_y to decompose and release NO_2. It is one mechanism by which NO_x reaches the remote marine boundary layer far from any direct emission (Fisher et al., 2016). Other sources of NO_x in the remote marine boundary layer are discussed in chapter 4 whilst the challenges of measuring NO_x accurately in the presence of NO_y is the subject of chapter 2.

1.2.2 O_3 production

The oxidation of VOC, methane, and CO by OH forms HO_2 peroxy radicals and RO_2 organic peroxyradicals (1.17 & 1.18) which can react with nitric oxide, forming nitrogen dioxide (reactions 1.19 & 1.20); resulting in net ozone formation through reactions 1.7 & 1.8 (Monks et al., 1998). The VOC oxidation cycle is closed by the regeneration of OH in reaction 1.20.

$$OH + CO + O_2 \rightarrow HO_2 + CO_2 \tag{1.17}$$

$$OH + CH_4 + O_2 \rightarrow CH_3O_2 + H_2O \tag{1.18}$$

$$CH_3O_2 + NO \rightarrow NO_2 + HCHO + HO_2 \tag{1.19}$$

$$HO_2 + NO \rightarrow NO_2 + OH \tag{1.20}$$

$$Net : \mathrm{VOC} + \mathrm{NO} \xrightarrow{\mathrm{OH}} \mathrm{O_3} + (\mathrm{CO_2/HCHO})$$

In pristine and remote environments where NO_x may be below the so-called compensation point (Jaeglé et al., 1998), peroxy radicals may combine rather than reacting with NO terminating the radical chain. In these regions O_3 destruction occurs as is the case in remote boundary layer at the Cape Verde observatory (Read et al., 2008).

1.2.3 OH production

With the route to tropospheric O_3 described in Sect. 1.2.2, OH is produced through reaction 1.2 (Atkinson, 2000). A minor route to OH production is the photolysis of

formaldehyde (HCHO) produced through VOC oxidation (Perner and Platt, 1979) as shown in reactions 1.21 to 1.23.

$$\mathrm{HCHO} + h\nu\,(<334nm) \rightarrow \mathrm{H} + \mathrm{HCO} \tag{1.21}$$

$$\mathrm{H} + \mathrm{O_2} + M \rightarrow \mathrm{HOO} + M \tag{1.22}$$

$$\mathrm{HOO} + \mathrm{NO} \rightarrow \mathrm{OH} + \mathrm{NO_2} \tag{1.23}$$

Photolysis of nitrous acid (HONO), is another potential source of OH. Although HONO can be made from the direct combination of OH and NO and so can be OH neutral. HONO can also be made form other sources e.g. heterogeneous hydrolysis of NO_2 (Bröske et al., 2003; Ramazan et al., 2004) and as discussed in chapter 4, photolysis of aerosol nitrate (Ye et al., 2016b; Reed et al., 2017) which lead to a net source of OH via HONO, the measurement of which is the subject of chapter 3.

1.2.4 The nitrate radical and night-time oxidation chemistry

The nitrate radical is formed by reaction of NO_2 with O_3. During day-time (1.24) it is rapidly photolysed to NO_2 and $O(^3P)$ (1.25) or NO and O_2 (1.26) with a lifetime of around ~ 5 seconds (Atkinson, 2000).

$$\mathrm{NO_2} + \mathrm{O_3} \rightarrow \mathrm{NO_3} + \mathrm{O_2} \tag{1.24}$$

$$\mathrm{NO_3} + h\nu \rightarrow \mathrm{NO_2} + \mathrm{O}(^3\mathrm{P}) \tag{1.25}$$

$$\mathrm{NO_3} + h\nu \rightarrow \mathrm{NO} + \mathrm{O_2} \tag{1.26}$$

During night-time NO_3 becomes the dominant oxidant species in the troposphere in the absence of a route to form OH. It reaches concentrations ~ 3 orders of magnitude greater than day-time OH (Wayne et al., 1991). Reaction of NO_3 with VOCs can form peroxy radicals, which in turn can form OH as in reactions 1.19 & 1.20 (Carslaw et al., 1997; Geyer et al., 2001; Platt, 1999). However, the rate of reactions between NO_3 and VOCs is generally slower than that of OH + VOC, though not necessarily for unsaturated and functionalised species.

The nitrate radical also appears to play a role in night-time halogen chemistry as discussed in chapter 4 whereby NO_3 reacts with halogen hydroxides forming nitric acid and halogen

oxide as shown in 1.27 where X = Br, I etc..

$$HOX + NO_3 \rightarrow HNO_3 + XO \tag{1.27}$$

1.2.5 Halogen chemistry

Since the discovery of the stratospheric 'ozone hole' in 1985 (Farman et al., 1985) there has been an intense focus on the role of halogen species in the atmosphere. In the troposphere too, halogens play a role in ozone depletion as demonstrated by Read et al. (2008). The mechanism by which halogen molecules, X_2 (where X = Cl, Br, I) catalytically destroy ozone is shown in reactions 1.28 to 1.31.

$$X_2 + h\nu \rightarrow 2\,X \tag{1.28}$$

$$X + O_3 \rightarrow XO + O_2 \tag{1.29}$$

$$XO + h\nu \rightarrow X + O \tag{1.30}$$

$$2\,XO \rightarrow X_2 + O_2 \tag{1.31}$$

The halogen oxide (XO) formed in reaction 1.29 can react with a peroxy radical (1.32) to form a halogen hydroxide (HOX) which can then be photolysed to form OH and re-form the halogen radical (1.33, Burkert et al. 2001; Simpson et al. 2015). This route to the hydroxyl radical means that halogens play a major role in determining the oxidising capacity by affecting the partitioning between O_3, HO_2, and OH oxidants (Bloss et al., 2005; Chameides and Davis, 1980).

$$XO + HO_2 \rightarrow HOX + O_2 \tag{1.32}$$

$$HOX + h\nu \rightarrow OH + X \tag{1.33}$$

Halogen oxides react with NO to form NO_2 affecting the Leighton ratio (Leighton, 1961). Thus perturbation in the Leighton ratio can be used to infer the presence of XO (or another oxidant). This is the subject of chapter 2. Halogen oxides may also act as a sink for NO_x by reaction with NO_2 to form a halogen nitrate, $XONO_2$, as in reaction 1.34. This halogen nitrate, though thermally labile and with a short photolytic lifetime, can be taken up on aerosol and hydrolysed (Sander et al., 1999) forming aerosol nitrate (1.35).

$$XO + NO_2 \rightarrow XONO_2 \tag{1.34}$$

$$XONO_2 + H_2O_{(aer)} \rightarrow HNO_{3(aer)} + X^+ + OH^- \tag{1.35}$$

In chapter 4 formation of halogen nitrates and their subsequent hydrolysis plays a central role in nitrogen cycling. However, as noted in that chapter there is uncertainty around heterogeneous halogen reactions and uptake coefficients (Abbatt et al., 2012) and gas phase chemistry (Simpson et al., 2015).

1.3 Summary

Figure 1.2 shows a simplified version of our current understanding of tropospheric NO_x chemistry coupled with O_3 and OH. Presently, the chemistry shown (and much more not shown) does not accurately reproduce NO_x observations in model simulations though it represents the extent of our current understanding.

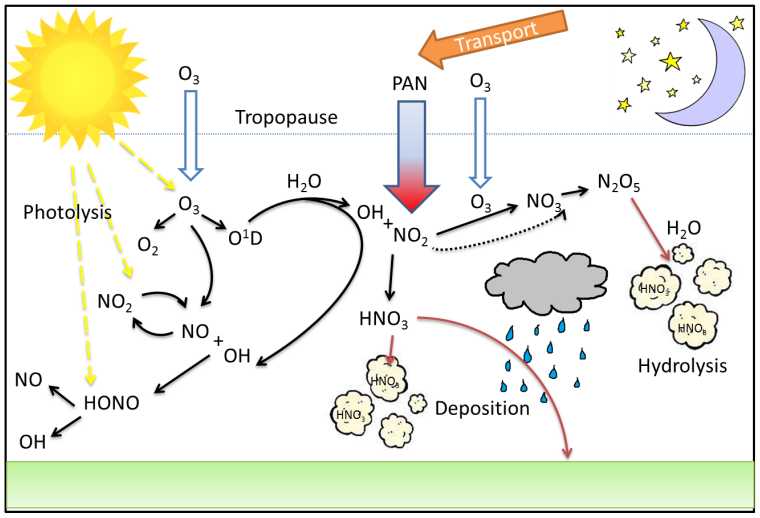

Figure 1.2 – A simplified diagram showing the life cycle of NO_x in the remote boundary layer.

It would appear that there is greater complexity and subtlety associated with tropospheric NO_x chemistry which is currently missing from Fig. 1.2 that this work seeks to discover.

1.4 Techniques

This thesis focusses on the measurement and interpretation of NO, NO_2, and HONO, therefore here a summary of commonly applied remote and *in-situ* methods and approaches to measuring these is presented.

1.4.1 Nitric Oxide, NO

Remote techniques for measuring NO involve either detection of the NO absorption band at 1876 cm^{-1} either by non-dispersive or Fourier transform infra-red spectroscopy (ND-IR and FT-IR respectively) measuring total absorption. Differential optical absorption spectroscopy (DOAS) can be used to measure NO using relative absorption in the deep UV at 52356 cm^{-1} (Dooly et al., 2008). In either case remote absorption techniques provide an integrated measurement over an area defined by the path length of the measurement with sensitivity proportional to that length and any other absorbing species at the same wavelength. As with all spectroscopic techniques the absorption cross-section of the species of interest, and any others species at the same wavelength must be well known in order to be quantitative.

A small number of widely implemented *in-situ* techniques for NO quantification exist, the most widespread being chemiluminescence. NO chemiluminescence exploits the reaction of NO with O_3 and subsequent emission of a photon from the decay of the excited state nitrogen dioxide produced (Drummond et al., 1985). The number of photons produced being directly proportional to the mole fraction of NO in the sample. This photon counting technique is has been extensively in both polluted and pristine environments and is the basis of measurements used in this study. It's success is down to the low limits of detection achievable and the robustness of the technique. Drawbacks include he need to obtain a zero measurement frequently and the need to calibrate or correct for humidity in the sample gas reducing sensitivity. Laser-induced fluorescence (LIF) analysis of NO by absorption of a photon by nitric oxide and then re-radiation at different wavelengths by the excited nitric oxide has also been employed, though much less widespread than NO chemiluminescence. Nitric oxide LIF has compared well with NO chemiluminescence (Hoell et al., 1985, 1987) and is sued extensively in the study of flame chemistry, though does not hold advantage over the simpler NO chemiluminescence in atmospheric applications. A cavity ring down spectroscopy (CRDS) system measuring NO_2 (and by chemical reaction, NO_x) at 404 nm may also quantify NO (Fuchs et al., 2009). In the CRDS system NO_2 is quantified by ring-down time of a cavity pulsed with light at a wavelength absorbed by NO_2. A second cavity measures the same, except that excess O_3 is introduced into the sample prior to detection in order to react NO to NO_2 with greater than 99 % efficiency, thus measuring NO_x. In this way NO can be derived by by subtracting the NO_2 signal from the NO_x

signal. The CRDS system was also compared with NO chemiluminescence and was found to be comparable in performance down to 100 pptV, however chemiluminescence systems still achieve lower limits of detection which is necessary in the pristine environment of the marine boundary layer.

1.4.2 Nitrogen Dioxide, NO_2

Many of the same techniques for quantifying NO_2 are shared with NO, with the exception of infra-red techniques due to the overlap of the absorption spectrum of water vapour with that of NO_2 rendering it unsuitable in atmospheric measurements. Differential optical absorption spectroscopy has been used widely with long-term networks operating across Asia and Russia (**?**). As with spectroscopic techniques for NO the absorption cross-section for NO_2 must be well known as must those of overlapping species in order to be quantitative.

Many more *in-situ* techniques are available for NO_2. LIF (laser-induced fluorescence; Matsumoto and Kajii 2003) and CRDS (cavity ring-down spectroscopy; Osthoff et al. 2006) are common in high sensitivity studies requiring a low limit of detection afforded by those sytems with even commercially available products agreeing well with research grade instruments (**?**). The advantage of direct measurements of NO_2 such as LIF and CRDS being no need to calibrate for any conversion factor or inlet efficiency as with e.g. photolysis-chemiluminescence systems described below and used in this work. Laser based systems often suffer from instability in laser power due to temperature etc. so must still be calibrated periodically (**?**). Limits of detection for NO_2 are similar to that of NO ~ 100 pptV and thus are again unsuitable in the pristine environment.

The most prevalent technique for measuring NO_2 is by NO-chemiluminescence after conversion. Historically conversion was achieved with a heated metal surface e.g. molybdenum, which is able to convert greater than 95 % NO_2. However this method is subject to interferences from other reactive nitrogen compounds which also dissociate to NO at elevated temperature (Dunlea et al., 2007; Grosjean and Harrison, 1985; Winer et al., 1974). This leads to an over reporting of NO_2 though the technique is still used extensively in air quality monitoring where close to emission source due to the robustness of the instruments.

A development of the catalytic conversion-chemiluminescence system is photolytic conversion-

chemiluminescence in which NO_2 is photolysed to NO rather than being converted catalytically by illumination of the sample gas at wavelengths specific to NO_2 (typically 365-405 nm). The advantage being that photolytic conversion is much more selective to NO_2 than heated surfaces (Ryerson et al., 2000), however as described in chapter 2 photolytic conversion is itself not free from interferences and uncertainties. The NO-chemiluminescence method does lend itself to very low limits of detection and unattended operation thus NO_2 detected by photolytic conversion also has a suitably low limit of detection and so is applicable in pristine background conditions.

1.4.3 Nitrous Acid, HONO

HONO by has by far the most number of measurement techniques adapted to its quantification in comparison to NO and NO_2. Three classes of technique exist with their own merits and disadvantages.

Off-line and integrating techniques typically collecting HONO in solution using a denuder or reactive filter before analysis by ion chromatography (Acker et al., 2005, 2006; Febo et al., 1993, 1996; Ianniello et al., 2007). The ion chromatograph instrument being highly sensitive and capable of quantification at pptV or lower levels provides excellent sensitivity to HONO. Sample collection efficiencies and artefacts are much less well defined however.

Remote methods of HONO detection are by DOAS and by infra-red spectroscopy as in chapter 3, as mentioned before with all spectroscopic techniques the cross-section must be known in order to quantity an analyte. With DOAS especially retrieval is challenging as the HONO absorption spectrum is entirely overlapped by NO_2 which is often in much higher abundance in the atmosphere.

Few on-line *in-situ* techniques for HONO exist, however LOPAP (long path absorption photometry, Heland et al. 2001) has been characterised extensively (Clemitshaw, 2004; Kleffmann and Wiesen, 2008; Kleffmann et al., 2006, 2013; Ródenas et al., 2013), commercialized and used widely. LOPAP uses sequential stripping coils with 99 % efficiency to sample HONO in the liquid phase where it is reacted to form an azo dye. The concentration of the dye formed is then proportional to the starting concentration of HONO in the sample gas and can be determined by colorimetry. The second stripping coil quantifies interferences from non-HONO species and is used to correct the signal from the first coil.

The advantage of LOPAP being that interferences are already accounted for in the measurement and that the measurement occurs *in-situ* allowing for the sudy of fast processes such as nitrate photolysis as in chapter 4.

1.5 Aim

This thesis aims to understand better the NO_x budget in the remote marine boundary layer which makes up $\sim 70\,\%$ of the planetary surface. Currently, simulations do not reproduce well the diel NO_x cycle observed in some remote tropospheric locations (Carsey et al., 1997; Monks et al., 1998). Understanding what NO_x chemistry is occurring will result in better overall simulation of the coupled oxidation chemistry, the lifetime of oxidants, and the fate of emissions. This requires the coupling of NO_x, halogen and aerosol chemistry whilst also fully understanding the measurement techniques used, their deficiencies, and strengths. In this way a more comprehensive understanding of tropospheric NO_x chemistry can be reached so that figure 1.2 may be updated to better reproduce the observations.

1.6 Thesis outline

Chapter 2 ("Interferences in photolytic NO_2 measurement: explanation for a missing oxidant?") seeks to explain how uncertainties in NO_x measurements by the chemiluminescence method can lead to erroneous assignment to oxidants. This work was presented as a peer reviewed article in the journal Atmospheric Chemistry and Physics in 2016.

Chapter 3 ("HONO measurement by differential photolysis") shows how interferences in photolytic NO_2 measurements can be exploited in order to quantify the difficult-to-measure nitrous acid. This work was presented as a peer reviewed article in the journal Atmospheric Measurement Techniques in 2016.

Chapter 4 ("Evidence for renoxification in the tropical marine boundary layer") interprets NO_x observations made at the Cape Verde Atmospheric Observatory using a box modelling approach to explain the unusual diel cycle observed. This aided the in-depth study of the measurement technique undertaken in chapters 2 & 3 from which the uncertainties are applied to the analysis. This work was presented as a peer reviewed article in the journal Atmospheric Chemistry and Physics in 2017.

Chapter 5 provides a synopsis of the conclusions from the previous 3 chapters along with final forward looking remarks.

Chapter 2

Interferences in photolytic NO_2 measurements: explanation for an apparent missing oxidant?

This chapter was presented as an article in the journal Atmospheric Chemistry and Physics.

Reed, C., Evans, M. J., Di Carlo, P., Lee, J. D., and Carpenter, L. J.: Interferences in photolytic NO_2 measurements: explanation for an apparent missing oxidant?, Atmospheric Chemistry and Physics, 16, 4707-4724, doi: 10.5194/acp-16-4707-2016, 2016.

''A lie told often enough becomes the truth."

Vladimir I. Lenin

2.1 Abstract

Measurement of NO_2 at low concentrations (tens of ppts) is non-trivial. A variety of techniques exist, with the conversion of NO_2 into NO followed by chemiluminescent detection of NO being prevalent. Historically this conversion has used a catalytic approach (molybdenum); however, this has been plagued with interferences. More recently, photolytic conversion based on UV-LED irradiation of a reaction cell has been used. Although this appears to be robust there have been a range of observations in low-NO_x environments which have measured higher NO_2 concentrations than might be expected from steady-state analysis of simultaneously measured NO, O_3, jNO_2, etc. A range of explanations exist in the literature, most of which focus on an unknown and unmeasured "compound X" that is able to convert NO to NO_2 selectively. Here we explore in the laboratory the interference on the photolytic NO_2 measurements from the thermal decomposition of peroxyacetyl nitrate (PAN) within the photolysis cell. We find that approximately 5 % of the PAN decomposes within the instrument, providing a potentially significant interference. We parameterise the decomposition in terms of the temperature of the light source, the ambient temperature, and a mixing time-scale ($\sim$ 0.4 s for our instrument) and expand the parametric analysis to other atmospheric compounds that decompose readily to NO_2 (HO_2NO_2, N_2O_5, $CH_3O_2NO_2$, $IONO_2$, $BrONO_2$, higher PANs). We apply these parameters to the output of a global atmospheric model (GEOS-Chem) to investigate the global impact of this interference on (1) the NO_2 measurements and (2) the NO_2 : NO ratio, i.e. the Leighton relationship. We find that there are significant interferences in cold regions with low NO_x concentrations such as the Antarctic, the remote Southern Hemisphere, and the upper troposphere. Although this interference is likely instrument-specific, the thermal decomposition to NO_2 within the instrument's photolysis cell could give an at least partial explanation for the anomalously high NO_2 that has been reported in remote regions. The interference can be minimized by better instrument characterization, coupled to instrumental designs which reduce the heating within the cell, thus simplifying interpretation of data from remote locations.

2.2 Introduction

Accurate quantification of atmospheric nitrogen oxide (NO_x, which is predominantly NO + NO_2 but includes small contributions from NO_3, N_2O_5, HONO, HO_2NO_2, etc.) concentrations is crucial for many aspects of tropospheric chemistry. NO_x plays a central role in the chemistry of the troposphere, mainly through its impact on ozone (O_3) and hydroxyl (OH) radical concentrations. O_3 is a greenhouse gas (Wang et al., 1995) that adversely impacts human health (Mauzerall et al., 2005; Skalska et al., 2010) and leads to ecosystem damage (Ainsworth et al., 2012; Ashmore, 2005; Hollaway et al., 2012). It is produced through the reaction of peroxy radicals (HO_2 and RO_2) with NO (Dalsøren and Isaksen, 2006; Lelieveld et al., 2004). The OH radical is the primary oxidizing agent in the atmosphere (Crutzen, 1979; Levy, 1972) as it controls the concentration of other key atmospheric constituents such as methane (CH_4), carbon monoxide (CO), and volatile organic compounds (VOCs). It is both produced through the reaction of NO with HO_2 and is lost by its reaction with NO_2. NO_2 itself also poses a public health risk (Stieb et al., 2002). Thus, understanding the sources, sinks, and distribution of NO_x is of central importance to understanding the composition of the troposphere.

During the daytime there is fast cycling between NO and NO_2, due to the rapid photolysis of NO_2 and the reaction of NO and O_3 to form NO_2 (Kley et al., 1981).

$$NO_2 + h\nu\,(< 410\,\text{nm}) \rightarrow NO + O(^3P) \tag{2.1}$$

$$O_2 + O(^3P) + M \rightarrow O_3 + M \tag{2.2}$$

$$O_3 + NO \rightarrow O_2 + NO_2 \tag{2.3}$$

Placing NO_2 into steady state and assuming that these three reactions are the only chemistry occurring leads to the Leighton relationship, ϕ (Leighton, 1961), in Eq. 2.4.

$$1 = \frac{k_1\,[NO]\,[O_3]}{j_{NO_2}\,[NO_2]} = \phi \tag{2.4}$$

The quantities in the relationship are readily measured and deviations from unity have been interpreted to signify missing (i.e. non-ozone) oxidants of NO. These perturbations have been used to infer the existence of oxidants such as peroxy radicals, halogen oxides, and the nitrate radical in the atmosphere, which have subsequently been confirmed by direct measurement (Brown et al., 2005; Mannschreck et al., 2004; Trebs et al., 2012; Volz-Thomas et al., 2003).

The concentration of NO_x varies from > 100 ppb (parts per billion) next to roads (Carslaw, 2005; Pandey et al., 2008) to low ppt (parts per trillion) in the remote atmosphere (Lee et al., 2009). Direct transport of NO_x from polluted to remote regions is not efficient, because NO_x is removed from the atmosphere on a time-scale of around a day by the reaction of NO_2 with OH and the hydrolysis of N_2O_5 on aerosol surfaces (Brown et al., 2004; Dentener and Crutzen, 1993; Riemer et al., 2003). Instead, reservoir species such as peroxyacetyl nitrate are made in polluted regions (where concentrations in both NO_x and peroxyacetyl precursors such as acetaldehyde are elevated) and are subsequently transported to remote regions, where they thermally break down to release NO_x (Fischer et al., 2014; Moxim et al., 1996; Roberts et al., 2007).

$$CH_3CHO + OH^\bullet + O_2 \rightarrow CH_3C(O)OO^\bullet + H_2O \tag{2.5}$$

$$CH_3C(O)OO^\bullet + NO_2 + M \rightleftarrows CH_3C(O)O_2NO_2 + M \tag{2.6}$$

The equilibrium between peroxyacetyl radicals, NO_2, and PAN (Reactions 2.5 and 2.6) is highly temperature-sensitive. Thus, the PAN lifetime changes from 30 min at 25 °C (Bridier et al., 1991) to 5.36 years at −26 °C (Kleindienst, 1994).

Measurements of NO_x species in the remote atmosphere have been made over the last 40 years. Multiple *in-situ* techniques are available such as LIF (laser-induced fluorescence; Matsumoto and Kajii 2003), CRDS (cavity ring-down spectroscopy; Osthoff et al. 2006), and QCL (quantum cascade laser; Tuzson et al. 2013). However, probably the most extensively used approach has been based on the chemiluminescent reaction between NO and O_3. This exploits the reaction between NO and O_3 (Reaction 2.7), which generates a electronically excited NO_2^* ($^2B_1$) molecule which decays to its ground state through the release of a photon (Reaction 2.8, Clough and Thrush 1967; Clyne et al. 1964).

$$NO + O_3 \rightarrow NO_2^* \tag{2.7}$$

$$NO_2^* \rightarrow NO_2 + h\nu\,(> 600\,\text{nm}) \tag{2.8}$$

This forms the basis of the chemiluminescence analysis of NO (Drummond et al., 1985; Fontijn et al., 1970; Kelly et al., 1980; Peterson and Honrath, 1999). The number of photons emitted by the decay of excited NO_2^* to NO_2 is proportional to the NO present before reaction with O_3 (Drummond et al., 1985). The photons emitted are detected by a cooled photomultiplier tube (PMT) with the sample under low pressure (to maximize the fluorescence lifetime of the NO_2^*) in order to yield a signal which is linearly proportional to

the number density of NO in the sample gas (Fontijn et al., 1970). Quenching of the NO_2 excited state occurs due to a range of atmospheric compounds; N_2, Ar, CO, CO_2, CH_4, O_2, He, H_2, and H_2O (Clough and Thrush, 1967; Drummond et al., 1985; Zabielski et al., 1984). Quenching is minimized by operating at high vacuum to reduce collision probability. However, quenching still occurs; thus, it is necessary to calibrate the detectors response (sensitivity) to a known concentration of NO regularly. Changing ambient humidity in the sample has a marked effect on drift in sensitivity and necessitates being corrected for, sample drying, or sample humidifying to mitigate.

With NO chemiluminescence analysers it is also possible to analyse NO_2 regarding whether it is first converted to NO, either catalytically (typically heated molybdenum) as in Reaction (2.9) (Villena et al., 2012) or by converting NO_2 into NO photolytically (Ryerson et al., 2000), exploiting Reaction (2.1).

$$\mathrm{Mo} + 3\,\mathrm{NO_2} \rightarrow \mathrm{MoO_3} + 3\,\mathrm{NO} \tag{2.9}$$

To measure NO and NO_2, the sample flows through the NO_2 to NO converter (of either type) to the reaction chamber, where the $NO + O_3$ reaction occurs and the decay of NO_2^* to NO_2 allows the concentration of $NO + NO_2$ in the air to be measured. Then, the sample flow is switched to bypass the NO_2 to NO converter. Now, only NO present in the sample is detected in the chemiluminescence reaction. The NO signal is then subtracted from the $NO + NO_2$ (NO_x) signal, giving the NO_2 signal. Both techniques for converting NO_2 to NO can be subject to interference. Catalytic conversion has been well documented to have positive responses to NO_y species such as nitrous and nitric acid as well as organic nitrates (Dunlea et al., 2007; Grosjean and Harrison, 1985; Winer et al., 1974). Photolytic conversion has been demonstrated to be affected by a negative interference from the photolysis products of VOCs reacting with NO within the photolysis cell (Villena et al., 2012) and has a possible positive interference from thermal decomposition of NO_y (McClenny et al., 2002).

Measurements of NO and NO_2 have been made in a range of low-NO_x locations using the chemiluminescence technique (Huntrieser et al., 2007; Lee et al., 2009; Peterson and Honrath, 1999; Zhang et al., 2008). Measurement of NO_x by the NO chemiluminescent technique in these locations can be challenging (Yang et al., 2004), often operating close to the limit of detection (LOD). Corrections may be necessary for oxidation of NO to NO_2 in the inlet by O_3 and, more problematically, by peroxy radicals produced by, for

example, PAN decomposition within the inlet. This oxidation acts to perturb the observed Leighton relationship in two ways: by release of NO_2 and by oxidation of NO by peroxy radicals to NO_2. Where NO and NO_2 are measured by one channel by switching the UV elements on and off periodically, there may be a greater discrepancy in the Leighton ratio as NO is oxidized to NO_2 by peroxy radicals produced from the thermal decomposition of PAN within the still warm, but not illuminated, NO_2 converter. Small corrections for a NO offset are typically made by assuming it is equivalent to a stable night-time value in remote regions (Lee et al., 2009), whilst the NO_2 offset is usually deduced from sampling a source of zero air (which may be used for NO if a stable night-time value is not obtainable). Correction for changing NO_2 photolytic conversion efficiency due to O_3 in the photolysis cell (see Sect. 2.3.2, Eq. 2.10) might also be appropriate when O_3 varies greatly or calibration in ambient air is not possible, i.e. in zero air, which contains no O_3.

Yang et al. (2004) identified a statistical source of error when determining NO and NO_2 by chemiluminescence. Yang et al. (2004) demonstrate that uncertainties in averaging signals which fall below ~ 10 times the 1σ limit of detection result in large errors in the $NO_2 : NO$ ratio, with extreme bias exhibited when signals fall below a signal-to-noise ratio ~ 5. This work shows that using weighted geometric mean of PMT counts to determine NO and NO_x (and hence NO_2), rather than the un-weighted or arithmetic mean, results in the least measurement bias. This error is in addition to any artefact signal biasing either NO or NO_2, as well as uncertainties in, for example, the NO_2 conversion efficiency.

Some measurements made in remote (low-NO_x) locations, such as Antarctica and over the open ocean have at times identified an unexplained imbalance in the Leighton relationship (Bauguitte et al., 2012; Frey et al., 2013, 2015; Hosaynali Beygi et al., 2011). Measured NO_2 concentrations are higher than would be expected from the observed NO, O_3, and $j\mathrm{NO}_2$ along with reasonable concentrations of other oxidants (peroxy radicals, halogen oxides). Various explanations have been posited in order to overcome the apparent oxidation gap, typically relying on an unmeasured oxidant, or pushing known chemistry into theoretical realms by theorizing high turnover of short-lived species (Cantrell et al., 2003; Frey et al., 2013, 2015; Hosaynali Beygi et al., 2011). An alternative explanation would be an unknown interference on the NO_2 measurement increasing its apparent concentration, if this interference has a similar diurnal concentration profile.

Here we explore the potential of PAN (as a probe for other NO_y species) to interfere with

chemiluminescence NO_2 measurements. In Sect. 2.3 we provide details of the experimental studies undertaken. In Sect. 2.4 we describe the results of experiments introducing differing concentrations of PAN into NO_2 converter/chemiluminescence systems. In Sect. 2.5 we analyse the potential for errors with different NO_x systems to investigate the interference on the measurement of NO_2 from PAN. In Sect. 2.6 we evaluate the impact of this interference on NO_2 measurements and on the Leighton relationship through the use of a global model. Lastly, we provide conclusions in Sect. 2.7.

2.3 Experimental details

In Sect. 2.3.1 we describe the two chemiluminescence instruments used for the analysis. The NO_2 converters are described in Sect. 2.3.2. In Sect. 2.3.3 the LIF instrument used to provide a reference analysis is described. We describe our protocol for production of PAN by acetone photolysis in Sect. 2.3.4. We provide details of the zero-air generation in Sect. 2.3.5. Then in Sect. 2.3.6 we describe the experimental methodology of PAN interference tests and Sect. 2.3.7 describes residency time tests.

2.3.1 Instrumentation

Chemiluminescent measurements were performed using dual-channel Air Quality Design Inc. (Golden, Colorado, USA) instruments equipped with UV-LED-based photolytic NO_2 converters – commonly referred to as blue light converters (BLCs). Two similar instruments were employed: the "laboratory" NO_x analyser (Sect. 2.3.1.1), on which the majority of the experiments were performed, and the "aircraft" NO_x analyser (Sect. 2.3.1.2), on which only temperature-controlled BLC experiments were performed.

Both instruments feature independent mass-flow-controlled sample flows on each channel (NO and NO_x). The wetted surfaces of the instrument are constructed of 1/4 in. PFA tubing, with the exception of 316 stainless steel unions/MFC internals.

Both instruments are calibrated for NO by internal, automatic standard addition. Calibration for NO_2 converter efficiency is by internal automatic gas-phase titration of NO with O_3 to form NO_2 with the NO signal measured with the BLC lamps active and inac-

tive as described by Lee et al. (2009). Artefacts in both NO and NO_2 are measured whilst sampling zero air.

2.3.1.1 Laboratory NO_x analyser

The laboratory NO_x analyser from Air Quality Design Inc. (AQD) is a custom dual-channel instrument designed for fast response and very low limit of detection (LOD) of 2.5 pptV averaged over 1 min. The dual-channel design means that there are effectively two separate NO chemiluminescence instruments working in parallel. Both channels have identical flow paths and share identical duplicate equipment: ozonizers, MFCs, PMTs, etc. Both channels share the same vacuum pump – an Edwards XDS 35i. One channel is equipped with a BLC immediately in front of the MFC flow control/low-pressure side of the system. It is possible to analyse NO with one channel and NO_x with the other to provide a constant, fast measurement (1 Hz) of NO and NO_2. Alternatively, a single channel can be used with the BLC in a switching mode so that it is active for only 40 % of the duty cycle to provide NO and NO_2 measurement – the other 60 % of the duty cycle is devoted to NO (40 %) and measuring zero (20 %). In this case the second channel might be used for NO_y by connection of a catalytic converter to the inlet as is the set-up at the Cape Verde Atmospheric Observatory GAW station (Lee et al., 2009). In these experiments both modes were used in order to replicate different instrument designs: a switching mode with a 40 % duty cycle of the NO_2 converter and a total sample flow of 1 standard L min^{-1}, and a parallel mode with a 100 % duty cycle of the NO_2 converter with a total sample flow of 2 standard L min^{-1}. Chemiluminescent zero is determined for 30 s every 5 min. A chemiluminescent zero is acquired by increasing the $NO + O_3$ reaction time by diverting the sample flow to a pre-reactor, where greater than 99 % of NO is reacted. The pre-reactor is a PFA volume immediately prior to the detection cell through which usually only O_3 flows but which, during zero, both the sample gas and O_3 flow. In this way, photon counts arising from slower ($\sim$2 orders of magnitude) alkene + O_3 reactions are accounted for and subtracted from the NO signal.

The nominal sensitivity of the instrument is 3.5 and 4.0 counts s^{-1} ppt^{-1} ($\pm$ 5 %) on channel 1 (NO) and channel 2 (NO and NO_x) respectively. The $\pm$ 5 % uncertainty arises from the error in the NO standard concentration, the error of the sample and standard mass flow controllers, and the reproducibility of the sensitivity determination. Sensitivity drift

was mitigated by performing all experiments under an overflow of stable zero air; thus, NO changes in, for example, humidity, which affects chemiluminescent quenching, occurred. The 1 min LOD (2σ) is ~ 2.5 pptV.

2.3.1.2 Aircraft NO_x analyser

The aircraft NO_x analyser, also from AQD, operates similarly to the lab NO_x analyser, with some alterations to make it suited to aircraft operation. These changes do not affect its use on the ground. It can therefore be considered analogous to the lab NO_x analyser with the exception of the BLC. This is of a non-standard design that uses six more powerful UV diodes which require active Peltier/forced air cooling in order to maintain an operating temperature close to ambient. The special requirements for this NO_2 converter are primarily because of the high sample flow rates needed to measure NO_x fluxes on an airborne platform at reduced pressure. However, in this study the sample flow rate was a constant 1 standard L min^{-1} per channel at ambient temperature and pressure.

The nominal sensitivity of the instrument is 8.3 and 11.6 counts s^{-1} ppt^{-1} ($\pm 5\,\%$) on channel 1 (NO) and channel 2 (NO_x) respectively. The 1 min LOD (2σ) is ~ 1.0 pptV.

2.3.2 NO_2 converters

Photolytic converters for the two chemiluminescent systems were supplied by AQD and manufactured according to their proprietary standards (Buhr, 2004, 2007). Other photolytic NO_2 systems have also been developed with variations in design, but operating similarly (Pollack et al., 2011; Sadanaga et al., 2010). Experiments with either NO_2 converter were carried out at ambient temperature and pressure: 20 °C, 1 atm.

Photolytic converters employ Reaction 2.1 to convert NO_2 to NO over a narrow wavelength band, thus providing a more selective NO_2 measurement to that provided by molybdenum catalysts (Ridley et al., 1988; Ryerson et al., 2000). The conversion efficiency is determined by Eq. 2.10, where t is the residence time within the photolysis cell. Here k[Ox] is the concentration and rate constant of any oxidant that reacts with NO to form NO_2 (Ryerson

et al., 2000).

$$\mathrm{CE} = \left[\frac{jt}{jt + k\,[\mathrm{Ox}]\,t}\right]\left[1 - \exp^{(-jt - k[\mathrm{Ox}]t)}\right] \tag{2.10}$$

The rate constant of photolysis of NO_2 (j), and thus the rate of production of additional NO beyond that in the original sample, is given in Eq. 2.11.

$$j(T) = \int_{\lambda\ \mathrm{min}}^{\lambda\ \mathrm{max}} F\,(\lambda)\,\sigma\,(\lambda,\,T)\,\phi\,(\lambda,\,T)\,\mathrm{d}\lambda \tag{2.11}$$

In Eq. 2.11 j is the rate constant (s^{-1}), F is the spectral photon flux (photons $cm^{-2}\,s^{-1}$,nm^{-1}), σ is the absorption cross section of NO_2 (cm^2), ϕ is the quantum yield (dimensionless) of NO_2 photo-dissociation, and T is the temperature (Burkholder et al., 2015). The j value of the converter is practically determined by the irradiant photolysis power of the UV-emitting elements and how efficiently the power is used.

2.3.2.1 Standard BLC

Standard BLCs consist of two ends housing the UV LEDs (1 W, 395 nm, UV Hex, Norlux Corp.) within a heat sink to which a cooling fan is attached. The ends are bolted to a central section with rubber gaskets forming an airtight seal. Within the centre section a propriety Teflon-like material block is housed which serves as a highly UV-reflective (> 0.95) cavity through which the sample gas flows (Buhr, 2007). On two of the opposing sides of the centre section are 1/4 in. Swagelok fittings acting as an inlet and outlet for the sample gas.

The volume of this illuminated sample chamber is 16 mL, which, with a standard flow rate of 1 standard L min^{-1}, gives a sample residence time of 0.96 s. Additional lamp end units were also supplied by AQD.

The conversion efficiency of the standard BLC with a sample flow of 1 standard L min^{-1} was between 22 and 42 % ($j = 0.2 - 0.6\,s^{-1}$) depending on the combination of lamp units used, whilst the external temperature of the converter was typically 34 to 45 °C. All experiments were carried out with sample gas at ambient temperature and pressure: 20 °C, 1 atm.

2.3.2.2 High-powered BLC

The high-powered BLC of the aircraft instrument is designed to operate at a higher flow rate (1.5 standard L min^{-1}) and lower pressure ($\sim$ 300 Torr), and therefore lower residence time, to that of the standard BLC to allow fast time resolution measurements from an aircraft. For this reason a greater number (six) of more powerful UV LEDs (2 W, 395 nm, Nichia Corp.) are used in order that the conversion efficiency is acceptable under these conditions. The lamps are placed evenly along two sides of a cylindrical cavity of the same highly UV reflective Teflon with inlets at opposing ends. The high-powered BLC lamps are actively (Peltier) cooled to 47 °C, and without Peltier cooling reached 77 °C. It was therefore possible to control the internal temperature of the BLC by varying the power supplied to the Peltier elements via the temperature controller.

The volume of this illuminated sample chamber is 10 mL, which, with a standard flow rate of 1 standard L min^{-1}, gives a sample residence time of 0.60 s, resulting in a conversion efficiency of 93 % ($j = 6.5\,s^{-1}$).

2.3.3 TD-LIF analyser

Laser-induced fluorescence (LIF) provides a direct NO_2 measurement, as opposed to chemiluminescence with conversion. A direct method of NO_2 determination to compare with the BLC NO_2 converters is desirable in order to properly know the source of any "artefact" NO_2 signal.

The thermal dissociation laser-induced fluorescence (TD-LIF) system is a custom instrument developed for aircraft and ground-based observations of NO_2, peroxy nitrates ($\sum$PNs), alkyl nitrates ($\sum$ANs), and HNO_3. A detailed description of the TD-LIF instrument can be found in Di Carlo et al. (2013), with a short description given here. The instrument uses LIF to detect NO_2 concentrations directly (Dari-Salisburgo et al., 2009; Matsumoto and Kajii, 2003; Matsumoto et al., 2001; Thornton et al., 2000) and, coupled with a thermal dissociation inlet system, allows measurement of $\sum$PNs, $\sum$ANs, and HNO_3 after conversion into NO_2 (Day et al., 2002). The TD-LIF comprises four main parts: the laser source, the detection cell system, the inlet system, and the pumps. The laser source is a Nd:YAG double-pulse laser (Spectra-Physics, model Navigator I) that emits light at

532 nm with a power of 3.8 W, a repetition rate of 15 kHz, and 20 ns pulse width. The detection cell system comprises four identical cells, one for each compound class, to allow simultaneous measurements. Each cell is formed by a cube and two arms where the laser beam passes through the sample air flow in the centre of the cell. Perpendicular to both (laser beam and air flow) there is the detector that is a gated photomultiplier with lens and long-pass filters to optimize the fluorescence detection, minimizing the non-fluorescence light that reaches the detector (Di Carlo et al., 2013; Dari-Salisburgo et al., 2009). The pump system includes a Roots blower coupled to a rotary vane pump to maintain a flow of $6\,\mathrm{L\,min^{-1}}$. The common inlet system is split into four channels: one at ambient temperature to measure NO_2, and the last three heated at 200, 400, and 550 °C to thermally dissociate $\sum$PNs, $\sum$ANs, and HNO_3 respectively into NO_2 (Di Carlo et al., 2013). To minimize quenching due to atmospheric molecules, and therefore increase the sensitivity of the TD-LIF, each cell is kept at low pressure (3–4 Torr). This increases the fluorescence lifetime of NO_2^* and facilitates the time gating of the photomultiplier to further reduce the background (Dari-Salisburgo et al., 2009). The TD-LIF is routinely checked for background by an overflow of zero air in the detection cells and is calibrated by standard addition of a known amount of NO_2 from a cylinder (NIST traceable) diluted in zero air – the flow of both zero air and NO_2 being MFC- controlled. The time resolution of the measurements is 10 Hz and the detection limits are 9.8, 18.4, 28.1, and 49.7 pptV ($1\,\mathrm{s}, S/N = 2$) for NO_2, $\sum$PNs, $\sum$ANs, and HNO_3 cells respectively (Di Carlo et al., 2013).

2.3.4 PAN preparation

In order to test the sensitivity of the instrument to peroxyacetyl nitrate (PAN) interferences, it was prepared by means of the photolysis of acetone and NO in air as described by Meyrahn et al. (1987) and later by Warneck and Zerbach (1992); Flocke et al. (2005). Reactions 2.12 – 2.16 show the reaction sequence by which PAN is formed by acetone

photolysis (Singh et al., 1995).

$$(CH_3)_2CO + h\nu \rightarrow CH_3CO^{\bullet} + CH_3^{\bullet} \tag{2.12}$$

$$CH_3^{\bullet} + O_2 + M \rightarrow CH_3O_2^{\bullet} + M \tag{2.13}$$

$$CH_3O_2^{\bullet} + NO \rightarrow CH_3O^{\bullet} + NO_2 \tag{2.14}$$

$$CH_3O^{\bullet} + O_2 + M \rightarrow CH_3C(O)O_2^{\bullet} + M \tag{2.15}$$

$$CH_3C(O)O_2^{\bullet} + NO_2 + M \rightarrow CH_3C(O)O_2NO_2 + M \tag{2.16}$$

Here, NO_2 reacts stoichiometrically with the peroxyacetyl radical to form PAN. In practice, an excess of acetone is used to ensure that NO reacts completely. A dedicated "PAN generator", as used by Whalley et al. (2004), was employed to produce a consistent source of $>95\,\%$ pure PAN (Flocke et al., 2005; Mills et al., 2007). The generator consists of flow control elements for the NO standard gas, the acetone flow, and the zero-air diluent flow; a thermostated (30 °C) acetone permeation oven consisting of a reservoir of HPLC grade acetone (ACS grade, Acros) with a silicone permeation tube placed in the head-space through which zero air flows; and a Pyrex glass photolysis cell illuminated by UV light centred at 285 nm (Pen-Ray mercury lamp, UVP). The Pyrex functions to filter wavelengths below 290 nm within the photolysis cell, thus minimizing PAN photolysis (Mills et al., 2007).

A minor product also found in the photolysis of acetone is methyl nitrate, $MeONO_2$, which is typically approximately 1 % of the total yield (Mills et al., 2007). The proposed origin of the methyl nitrate (Williams et al., 2014) is shown in Reaction 2.17 and formaldehyde, which is formed as a major by-product is shown in Reaction 2.18 (Singh et al., 1995; Warneck and Zerbach, 1992).

$$CH_3O_2^{\bullet} + NO \rightarrow CH_3ONO_2 \tag{2.17}$$

$$CH_3O^{\bullet} + O_2 \rightarrow CH_2O + HO_2 \tag{2.18}$$

Methyl nitrate is also found in the atmosphere through oceanic emission (Moore and Blough, 2002) and as a product of the thermal decomposition of PAN (Fischer and Nwankwoala, 1995; Roumelis and Glavas, 1992; Warneck and Zerbach, 1992).

All flow rates within the PAN generator were calibrated using a Gilian Gilibrator-2 air flow calibrator (Sensidyne). The PAN generator is capable of continuously producing 0.1 – 20.0 ppbV PAN. Linearity and mixing ratio of the PAN output was confirmed by a

PAN-GC equipped with an ECD detector as described by Whalley et al. (2004), and also by complete reduction back to NO using a heated (325 °C) molybdenum catalyst (Thermo Environmental). The LIF instrument, described in Sect. 2.3.3, was used to quantify NO_2 produced directly in the PAN generator, which other authors (Flocke et al., 2005) have found to be the main impurity, with the results presented in Sect. 2.3.6 showing that $\leq 1\,\%$ NO_2 is emitted directly.

2.3.5 Zero air

Zero air was generated from dried ($-40\,T_d$) compressed air by subsequent filtering through a cartridge of molecular sieve (13×, Sigma Aldrich) to ensure a consistent humidity throughout all experiments and was regenerated by heating to 250 °C for 24 h when necessary. A second filter cartridge placed after the molecular sieve was packed with Sofnofil (Molecular Products) and activated charcoal (Sigma Aldrich) in order to remove ozone, NO_x, and VOCs which may be present in the compressed air. Zero air generated from the compressed air and filter cartridges system and zero air from an Eco Physics AG PAG 003 pure air generator (the industry standard) were both sampled by the NO chemiluminescence analyser. No difference in the counts of the NO analyser as observed between the two sources of zero air, both showing levels of NO below the LOD (< 2.5 pptV). Thus the NO content of both sources of zero air was considered to be insignificant and comparably low.

The NO_2 content of any zero air used is critical (more so than NO) in this study. In order to determine the NO_2 content of the zero-air sources, a direct measurement of NO_2 was required in order to avoid biasing the experimental procedure. The LIF instrument described in Sect. 2.3.3 was used to compare the zero-air sources (Table 2.1).

Zero air from both the PAG 003 and the filter stack was sampled by the NO_2 LIF analyser. Additionally, high-grade bottled zero air (BTCA 178, BOC speciality gases) was analysed for NO_2. Table 2.1 shows the photomultiplier counts per second whilst sampling 1.5 standard L min^{-1} of zero air. The dark counts of the PMT in the absence of laser light are typically less than 3 counts s^{-1}. The counts recorded are therefore the sum of any NO_2 fluorescence and scattered laser light. It is clear that the Sofnofil–carbon filter system has an advantage over both the PAG 003 and BTCA 178 zero-air sources in that a lower

signal for NO_2 fluorescence was observed. Typical sensitivity of the LIF NO_2 channel was $\sim 180\,\mathrm{counts\,s^{-1}\,ppb^{-1}}$; thus, a $4-4.5\,\mathrm{counts\,s^{-1}}$ improvement in zero background equates to $22-25\,\mathrm{ppt}$ improvement in accuracy. Consequently, all dilution, zeroing, and PAN generation utilized the Sofnofil–carbon filter system.

Table 2.1 – Comparison of the NO_2 observed from measurement of three zero-air sources (Eco Physics AG PAG 003, BOC speciality gases BTCA 178, and Sofnofil–carbon–13× molecular sieve filters) by LIF. The average of ten 1 min averages is shown in pptV, normalized to the lowest reading, in raw PMT counts $\mathrm{s^{-1}}$ as well as the standard deviation of those averages.

	PAG 003	BTCA 178	Sofnofil–carbon
Normalized concentration (pptV)	23.06	26.17	–
Signal ($\mathrm{counts\,s^{-1}}$)	88.10	88.66	83.95
Standard deviation	1.64	1.56	1.81

2.3.6 Experimental procedure

The NO_x analysers were first calibrated for sensitivity/converter efficiency whilst sampling zero air by overflowing the inlet from the internal source prior to the experiment for at least 2 h. This is because the PAN from the generator is in zero air which has a very low dew point ($-40\,T_\mathrm{d}$) and the sensitivity of the NO_x analyser is reduced by high humidity in ambient sample gas. This means that switching the NO_x analyser from sampling ambient (humid) air to zero air causes the sensitivity to rise slowly and the humidity inside of the reaction cell to decrease. After establishing an NO flow (4.78 ppm NO in N_2, BOC speciality gases) of $0.5\,\mathrm{mL\,min^{-1}}$ into the PAN generator, the acetone flow was then adjusted to $\sim 10\,\mathrm{mL\,min^{-1}}$ and the diluent flow of zero air adjusted to achieve the desired output mixing ratio. The internal zero air of the NO_x analyser was then shut off so that the NO_x analyser was sampling zero air from the PAN generator. Note that the total flow from the PAN generator always exceeded the sample requirements of the NO_x analyser with excess flow vented to the atmosphere. The system was then allowed to stabilize until a consistent NO value was recorded on the NO_x analyser. Next, the acetone photolysis lamp of the PAN generator was switched on so that acetone was photolysed in the presence of NO to form PAN. Complete NO conversion to PAN was indicated by the fact that in all cases the NO signal measured by the NO_x analyser fell to $\sim 0\,\mathrm{ppbV}$ after the acetone–NO mixture was illuminated by the photolysis lamp; $> 99.5\,\%$ conversion was

reported by Mills et al. (2007) with the same system. The diluent flow from the PAN generator was then varied to achieve PAN mixing ratios of between 0.2 and 1.3 ppbV. The corresponding NO_2 signal was recorded once stable. This procedure was repeated for various combinations of BLC lamps/assemblies and analyser operation modes.

In order to investigate any interference from un-reacted acetone, the NO_x analyser was allowed to sample the output of the PAN generator with the photolysis lamp off, i.e. a flow of acetone and NO gas. No additional NO_2 signal relative to zero air was observed during these experiments at any mixing ratio of NO.

To investigate any interference from un-reacted peroxy radicals left over from photolysis of excess acetone, produced in Reaction 2.12, the NO_x analyser was allowed to sample acetone that had been photolysed within the PAN generator in the absence of NO. NO was then added downstream of the photolysis cell at the NO_x analyser inlet. In this way, any peroxy radicals exiting the PAN generator will cause a loss of NO and a production of NO_2 which can be quantified. No loss of NO or production of NO_2 was observed, indicating that peroxy radicals from acetone photolysis within the PAN generator do not have a long enough lifetime (self-reaction or surface loss) before entering the BLC to cause an interference or "PERCA-like" (PEroxy Radical Chemical Amplifier; Clemitshaw et al. 1997) chemistry within the BLC.

It should be noted that sampling acetone does cause a small increase in the chemiluminescent zero count (a few hundred counts on a signal of $\sim$4000) of the NO_x analyser as acetone does react with ozone; this chemiluminescence interference is known (Dunlea et al., 2007) and is accounted for in the measurements by the chemiluminescent zero taken every 5 min described in Sect. 2.3.1.1.

To test whether the PAN generator produced any NO_2 directly (i.e. rather than as a consequence of decomposition of PAN to NO_2 within the BLC), a direct measurement of NO_2 was employed using the TD-LIF described in Sect. 2.3.3. The measured signal relative to pure zero air was measured in the LIF NO_2 channel when sampling various mixing ratios of PAN from the generator as shown in Fig. 2.1. It is evident that the NO_2 signal observed while sampling PAN from the generator lies within the noise of the zero signal measurement. In this case each point represents a 10 min average, as does the zero measurement. With an averaging time of 10 min the theoretical limit of detection is estimated

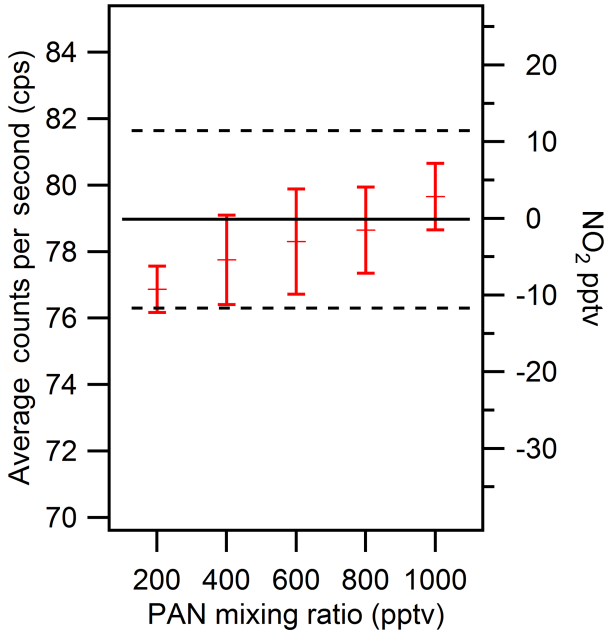

Figure 2.1 – The average raw counts per second (left) and pptV (right) recorded by a LIF instrument when sampling various mixing ratios of PAN (in red) and zero air (black). The variance of the zero-air signal is also shown (dashed black). The average signal while sampling PAN falls within the noise of the zero signal.

to be less than 0.1 pptV – taking a 10 Hz LOD of 9.8 pptV, and averaging 6000 points (i.e. 10 min), the precision improves by a factor of approximately $1/\sqrt{n}$, where n is the number of points averaged

It was therefore determined that only PAN could be an interfering species in the BLC from the PAN generator. The small percentage of methyl nitrate which may be produced is discounted due to it being less thermally labile that PAN itself. Additionally, the percentage interference observed is significantly greater than any expected or reported methyl nitrate yield from PAN synthesis by acetone photolysis i.e. 1 % (Mills et al., 2007). In the following discussion we address the possibility of photolytic and thermal dissociation of PAN or methyl nitrate to NO_2 and subsequently NO within the photolytic converter.

2.3.7 Residence time

The residence time of PAN in the 2.7 m PFA inlet linking the PAN generator to the NO_x analysers (shown in Table 2.2) was varied by varying the flow rate. This was achieved by altering the sample flows through the each of the NO_x analyser channels (which share

a common inlet). Residence times were 2.10 and 1.05 s^{-1} for one- and two-channel operation respectively.

2.4 Impact of PAN on NO_2 measurements

In this section we describe experiments investigating the impact of PAN on the two NO_2 instruments' measurements. In Sect. 2.4.1 and 2.4.2 we explore the interference in the laboratory instrument with a range of BLC converters, eliminating any possibility for inlet effects in Sect. 2.4.3, and in Sect. 2.4.4 we explore the interference in the aircraft instrument which has an active cooling of the converter. In Sect. 2.5.1 we investigate whether photolytic decomposition of PAN could lead to the interferences, and in Sect. 2.5.2 we investigate whether thermal decomposition could be the source.

2.4.1 Standard BLC and laboratory NO_x analyser in constant mode

PAN was introduced to the laboratory NO_x analyser, equipped with a BLC as described in Sect. 2.3.2.1, diluted in zero air through a range of mixing ratios. The resulting mixing ratio recorded by the analyser is presented in the following sections. Figure 2.2 shows that the artefact NO_2 signal is proportional to increasing PAN mixing ratios. An artificial signal corresponding to 8 to 25 % of the initial PAN mixing ratio was generated. The percentage conversion of PAN to NO_2 is on average highest at the lowest converter efficiency and vice versa. Potential reasons for this effect are addressed in Sect. 2.5.2.

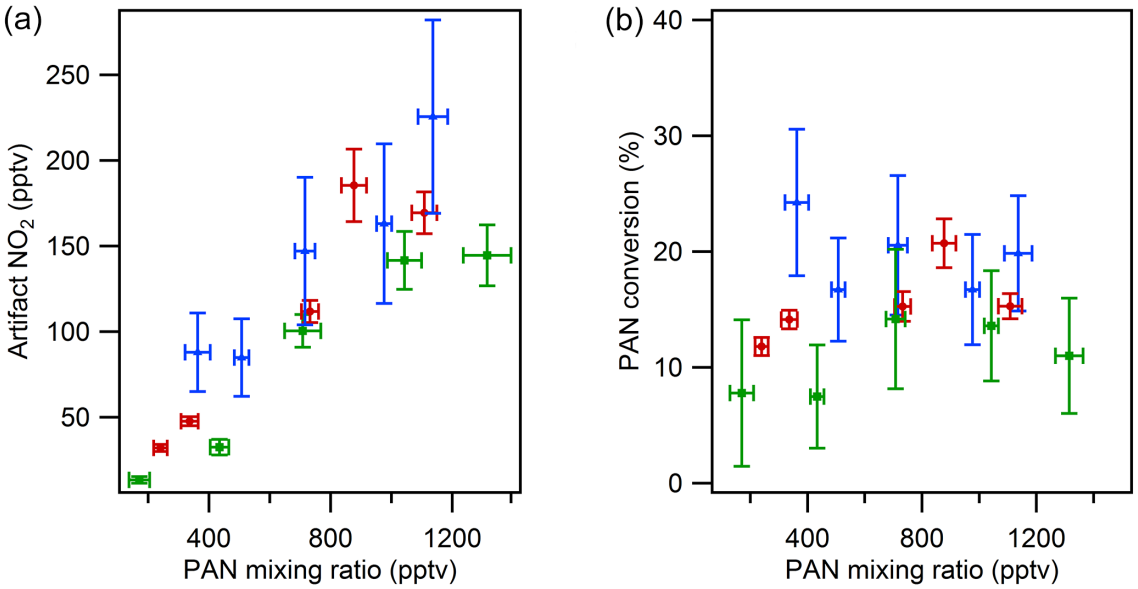

Figure 2.2 – The measured NO_2 artefact signal **(a)** of the supplied PAN mixing ratio, and as a percentage **(b)**, for three BLC units operating in constant mode separated by NO_2 conversion efficiency. Green: 41 ; red: 35 %; blue: 22 %.

2.4.2 Standard BLC and laboratory NO_x analyser in switching mode

Figure 2.3 shows the artefact NO_2 signal resulting from PAN using the same three BLC units operated in switching mode (40 % duty cycle). The percentage PAN conversion observed is lower in all cases than in the corresponding constant mode. This is likely due to the lower lamp temperature as a result of operating only 40 % of the time. The relationship between conversion efficiency and signal is not as clearly evident here as for constant mode operation (Fig. 2.2). It is possible that the greater variation in the measurement due to the lower amounts of NO_2 produced obscured any trend; however, it is clear that there is still a significant proportion of PAN measured as NO_2 – an average of 5.8 %.

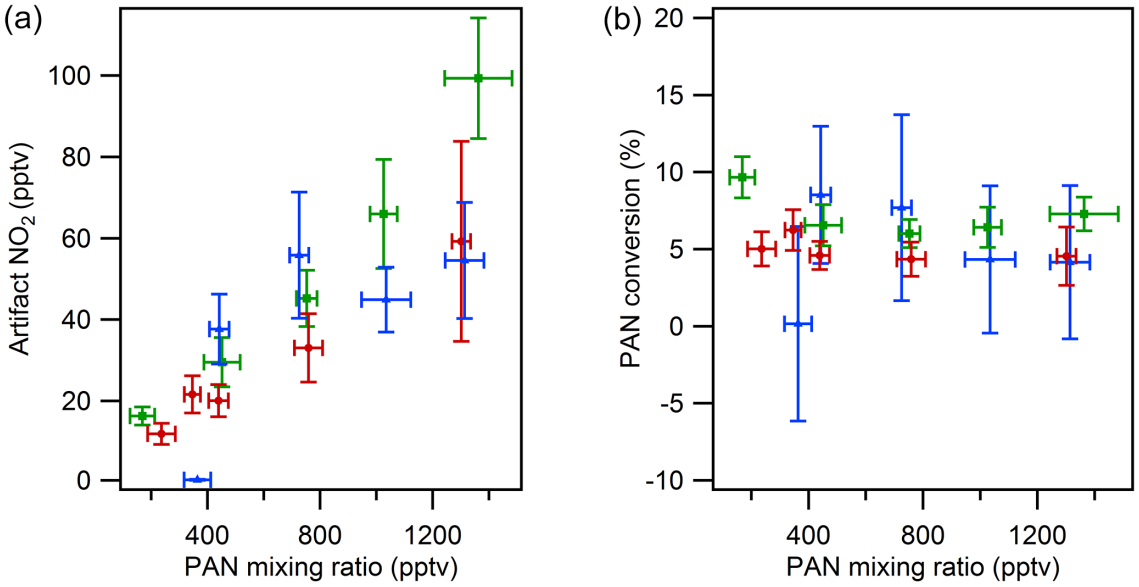

Figure 2.3 – The measured NO_2 artefact signal as a function of the supplied PAN mixing ratio **(a)**, and as a percentage **(b)**, for three BLC units operating in switching mode separated by NO_2 conversion efficiency. Green: 41 %; red: 35 %; blue: 22 %.

2.4.3 Inlet residence time effects

It is not clear from either Fig. 2.2 or 2.3 whether the PAN decomposition occurs within the BLC exclusively or within the inlet of the system, as has been claimed previously (Fehsenfeld et al., 1987). Previous studies (Fehsenfeld et al., 1990; Ridley et al., 1988; Sadanaga et al., 2010) have also reported a small PAN interference with photolytic converters, while some have found the contribution to the NO_2 signal from PAN to be negligible (Ryerson et al., 2000). Others (Val Martin et al., 2008) acknowledge the possibility for interference and estimate a small (2 to 4 pptV) positive bias. The photolytic converter designs in these studies vary greatly in their implementation and do not have the same ubiquity as BLCs used here, i.e. within the GAW network (Penkett et al., 2009).

Table 2.2 – Effect of varying the residence time of PAN (1.0 ppb) within a 2.7 m PFA inlet on artefact NO_2 in switching mode.

	Inlet residence time (s^{-1})			
	0.84	1.05	1.40	2.10
NO_2 (%)	5.4	5.4	5.2	5.3

Table 2.2 demonstrates that the residence time of PAN within the inlet does not affect

the signal arising from PAN decomposition in our system. This rules out any significant contribution from PAN decomposition in the inlet to any artefact signal. The inlet in this case consists of ~ 2.7 m 1/4 in. PFA tubing shielded from light and held at 20 °C. In other applications – for example if the inlet is heated, contaminated, or has a very long residence time – it is quite possible that significant PAN decomposition occurs.

From these experiments it is evident that a significant NO_2 signal is observed when sampling PAN diluted in zero air. The signal seen corresponds to around 8 to 25 % of the PAN supplied, which represents a significant interference. The possibility of thermal decomposition within the inlet was ruled out.

2.4.4 High-powered and actively cooled photolytic NO_2 converter

Figure 2.4 shows the difference in NO_2 signal between the cooled and un-cooled high-powered BLC described in Sect. 2.3.2.2. In all of the cooled cases the NO_2 measured was significantly lower than in the un-cooled case; this accounts for any increased artefact (the signal recorded when sampling zero air) in the un-cooled case. The conversion efficiency was 93 % for $NO_2 \rightarrow$ NO.

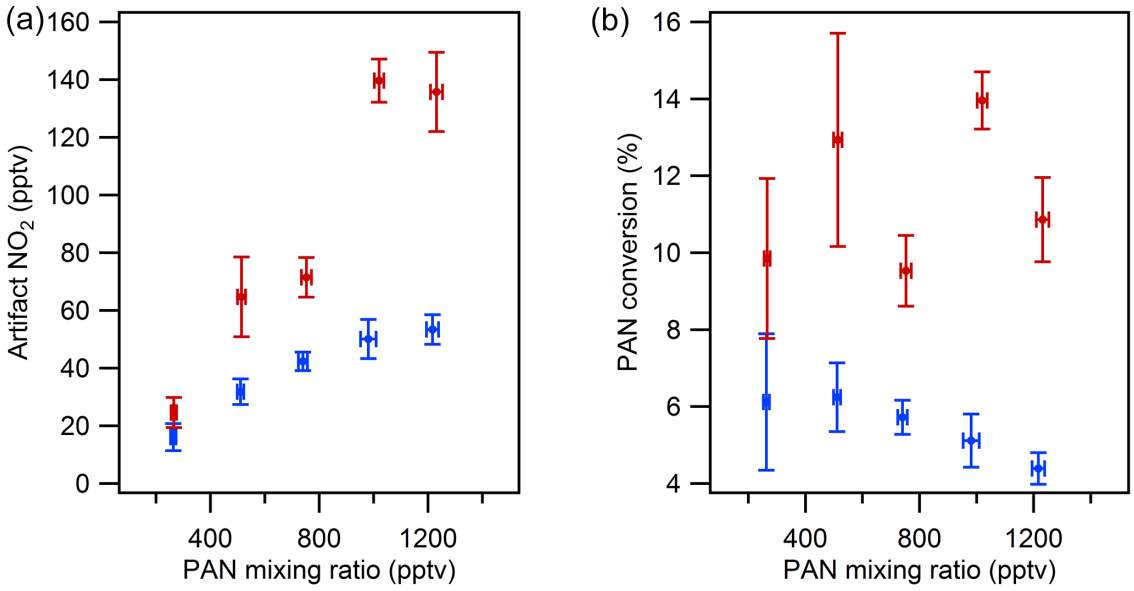

Figure 2.4 – The measured NO_2 artefact signal as a function of the supplied PAN mixing ratio **(a)**, and as a percentage **(b)**, for the cooled (blue) and un-cooled (red) high-powered BLC.

The effect of actively cooling the BLC lamps is significant, as apparent in the much lower NO_2 concentrations measured whilst sampling a range of PAN mixing ratios (Fig. 2.4). It

is therefore evident that there is a significant effect of cooling the UV LEDs which acts to mitigate any signal arising from PAN.

2.5 Results

2.5.1 Possible photolytic interferences of BLCs

There exists potential for photolytic interferences in photolytic converters, e.g. HONO, depending on their spectral overlap. Here we investigate this possibility with BLCs by taking the spectral output of a range of LED units against the absorption cross sections of various atmospheric compounds.

Spectral radiograms of the UV-LED elements of standard BLCs were obtained using an Ocean Optics QE65000 spectral radiometer coupled to a 2π quartz collector. The spectrometer and collector optics were calibrated using an NIST traceable light source (OL FEL-A, Gooch and Housego) and ultra-linear power supply (OL 83A, Gooch and Housego). The light source is a 1000 W quartz–halogen tungsten coiled-coil filament lamp with spectral irradiance standard F-1128. The lamp was operated at 8 A DC (125 V), with the lamp–collector distance fixed at 50 cm. Calibration was carried out in a light-sealed chamber. Spectra of the BLC UV-LED lamps were taken within the same light-proof chamber with the same distance between the lamp and collector.

Figure 2.5 shows the spectral emission of six different BLC UV-LED units. These units ranged in age from new to nearing the end of their service life – i.e. the conversion efficiency of the whole BLC unit had fallen below acceptable limits. As the LED units age, the relative intensity of their outputs declines; this decrease in intensity can be due to dimming of the overall output or failure of individual array elements determined by visual inspection during operation. It should be pointed out, however, that the light intensity of the UV LEDs is not directly proportional to the NO_2 conversion efficiency of the complete whole BLC. Rather, the conversion efficiency is strongly dictated by the condition of the reflective Teflon-like cavity. For example, disabling one of the two lamps in a BLC does not reduce the conversion efficiency by half but by a much smaller percentage. Additionally, replacing the UV-LED elements of a converter whose conversion efficiency has dropped below 30 % with new lamps will not lead to a recovery of the conversion.

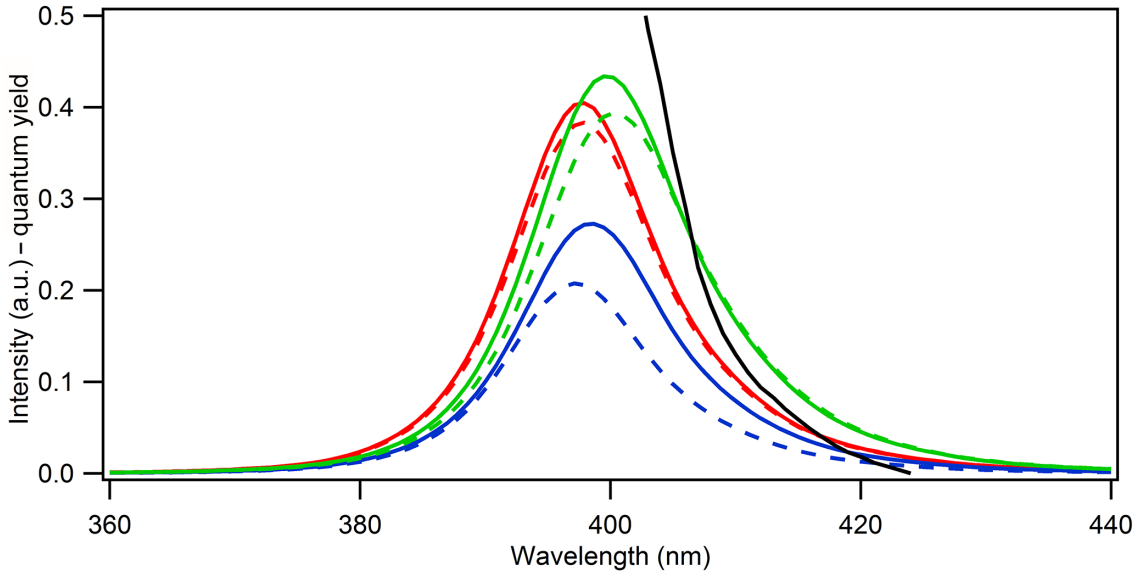

Figure 2.5 – Spectral output vs. wavelength of two new, previously unused BLC lamps (no. 1, solid green; no. 2, dashed green), two used lamps (no. 3, solid red; no. 4, dashed red) still within acceptable conversion efficiency, and two which fall below acceptable limits (no. 5, solid blue; no. 6, dashed blue). The NO_2 quantum yield is shown in black.

Scrupulous cleaning of the reflective cavity with solvent and mild abrasion of the surface will, however, recover the conversion efficiency considerably. This is because Teflon-like block is a bulk reflector, that is, the UV penetrates up to ~ 1 cm into the material. It is this reflective property that makes most efficient use of the light and achieves high conversion efficiency at low residence times. Adsorption of any UV absorbing material on the surface reduces the reflectivity dramatically. Additionally, the Teflon block is somewhat porous and so contaminants may penetrate into the bulk (or at least below the surface). Solvent may remove most of the contaminants (though strong solvents can damage the block); however, those which have moved below the surface can only be removed by removing the contaminated layer of Teflon. The porosity also gives rise to the artefact NO_2 signal as new material off-gases (as can other surfaces, e.g. LED lens). Sample gas may also diffuse into, and out of, the bulk very slowly giving a small memory effect as NO_x and NO_y exchange with the sample stream.

Figure 2.6 depicts the absorption cross sections of atmospheric nitrogen compounds taken from Burkholder et al. (2015) against the measured spectral output of UG5 UV-passing filter glass (Schott, 1997) used in lamp-type photolytic converter (PLC) optics (e.g. Eco Physics AG PLC 760), and the averaged measured spectral output of six individual BLC

UV-LED arrays of varying running hours. Also shown is the NO_2 quantum yield (Gardner et al., 1987; Koepke et al., 2010). It can be discerned that the UV-LED output overlaps fully with the NO_2 absorption band and the NO_2 quantum yield and is therefore photon-efficient. It is also shown that there is minimal overlap with HONO and no overlap in the spectrum at all with PAN. It has been shown that there is no overlap with methyl, ethyl, or isopropyl nitrate (Carbajo and Orr-Ewing, 2010; Talukdar et al., 1997) – methyl nitrate being a minor impurity in PAN synthesis. There is only very minor overlap in the PLC optics spectrum with PAN, methyl ethyl, and isopropyl nitrate. PLC optics exhibit a great deal of overlap with HONO, which the UV LEDs do not. Both systems suffer some overlap with NO_3 radicals and $BrONO_2$, more so in the case of PLC optics than for UV LEDs. It is evident that PAN is unable to be photolysed in a BLC, nor in other types of photolytic converters, due to the narrow spectral output of UV not having overlap with the PAN absorption spectrum. Other species such as HONO, $BrONO_2$, and NO_3 radicals may constitute a photolytic interference.

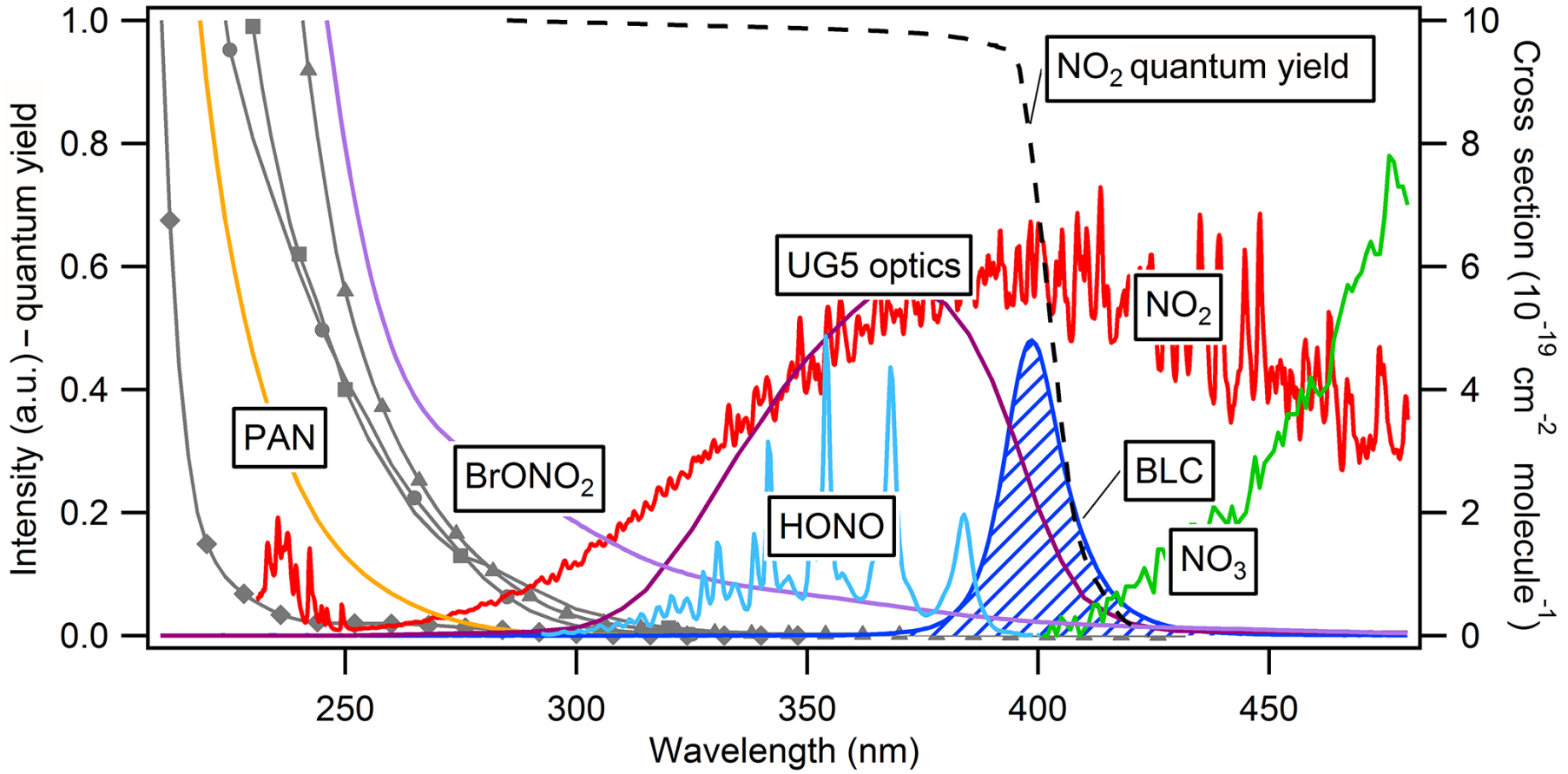

Figure 2.6 – Absorption cross section (red) and quantum yield (dashed black) of NO_2, presented with the spectral output of UG5 optical filtering (purple) and an average of the six BLC lamps used in this study output (dark blue). Interfering species are shown – NO_3 radicals (green), HONO (light blue), and $BrONO_2$ (lilac) – which are overlapped significantly by the UG5 optics – completely in the case of HONO, whilst much less overlap is exhibited by the UV LEDs of the BLC. Also shown is PAN (gold), which is clearly not overlapped by either UG5 or BLC light sources. Additional non-interfering species – $ClONO_2$ (triangles), N_2O_5 (squares), HO_2NO_2 (circles), and HNO_3 (diamonds) – shown for reference.

2.5.2 Possible thermal interferences in BLCs

The thermal and electronic characteristics of the standard BLC lamps were found in bench tests and are summarized in Table 2.3. Each lamp was run constantly whilst recording the surface temperature and power draw of the light-emitting element. The surface temperature was recorded once a stable maximum had been reached and maintained for at least 10 min – representative of using a BLC in constant mode. The ambient temperature during the experiments was 20 °C.

Table 2.3 – Peak surface temperature and current drawn by BLC lamps in a bench test at 20.0 °C showing converter efficiency, current, and surface temperature.

Lamp no.	Converter efficiency (%) ±1	BLC lamp surface temperature (°C) ±0.05	Current draw (A) ±0.0005
1	41	79.8	0.969
2		75.3	0.953
3	35	77.6	0.933
4		74.0	0.931
5	22	76.2	0.916
6		56.4	0.567

Table 2.3 describes the power draw and surface temperature of three BLC UV-LED lamp pairs measured during tests, along with their $NO_2 \rightarrow NO$ converter efficiencies when assembled as a complete BLC. The surface temperature of the individual lamps correlates positively with the power drawn by each lamp ($R^2 = 0.96$) and indeed with output intensity (Fig. 2.2), but with each lamp pair there is only weak correlation ($R^2 = 0.43$) between converter efficiency and temperature. It is worth noting that the power consumption is a combination of the light output, heat dissipation, and power to the cooling fan. It is clear, however, that the temperature experienced by the sample gas within the NO_2 converter is significantly above ambient. In fact, the entire NO_2 conversion cavity is heated by the lamps, leading to external temperatures of the converter of between 34 and 45 °C. It is known that the major product from thermal decomposition of PAN is NO_2 (Reaction 2.19; Roumelis and Glavas 1992; Tuazon et al. 1991). The NO_2 produced thermally within the converter may then be photolysed to NO and thus be measured as

NO_x and attributed to atmospheric NO_2.

$$CH_3C(O)OONO_2 \rightleftharpoons CH_3C(O)OO^{\bullet} + NO_2 \tag{2.19}$$

A model of the gas-phase thermal decomposition of PAN over a range of temperatures within the BLC with a residence time of 0.96 s is shown in Fig. 2.7. The model run was conducted in FACSIMILE kinetic modelling software (MCPA Software Ltd.) using rate constants from IUPAC evaluated kinetic data (Atkinson et al., 2006).

The model output indicates that measurable PAN decomposition to NO_2 occurs above $\sim 50\,^{\circ}C$. At the maximum LED surface temperature recorded (80 °C), the model predicts $\sim 30\,\%$ decomposition of PAN to NO_2. However, as only the two UV-LED lamps are at such an elevated temperature, we can expect a temperature gradient/heating rate within the BLC so that the average temperature seen by the sample gas over the 0.96 s residence is somewhat lower. We assume that only gas-phase decomposition occurs, rather than any surface enhanced heterogeneous process; however, as the BLC has Teflon, stainless steel, rubber, conformal coating, etc. contacting the sample gas (some of which maybe heated to an extent), it is a possibility. Ryerson et al. (2000) found no measurable heterogeneous PAN decomposition on the quartz surface of their converter. It is expected that, in a switching mode with only 40 % duty cycle of the lamps, the LED surface temperature would be lower also. This is borne out when using the external surface temperature of the BLC as a proxy – the temperature was lower in switching mode than in constant mode for the same conversion efficiency. It is shown more clearly in the inset that an average temperature of 60 °C would cause a 4.6 % decomposition of PAN and account for the NO_2 measured during experiments with the standard BLCs. Therefore, together with the spectral measurements reported in Sect. 2.5.1, it seems highly unlikely that the source of the artefact signal is through direct photolysis of PAN, leaving thermal decomposition, modelled in Fig. 2.7, the remaining explanation.

In Sect. 2.4.1 the percentage conversion of PAN to NO_2 was found to be, on average, highest at the lowest converter efficiency and vice versa. The fact that the converter temperatures are very similar at different converter efficiencies (Table 2.3) suggests that the percentage of PAN thermally dissociated in each case is similar. An explanation for the inverse relationship between percentage conversion of PAN to NO and conversion efficiency (Fig. 2.2) lies in the way that the NO_2 concentration is derived, which is an inverse function of the assumed conversion efficiency as in Eq. 2.10, where converter efficiency is

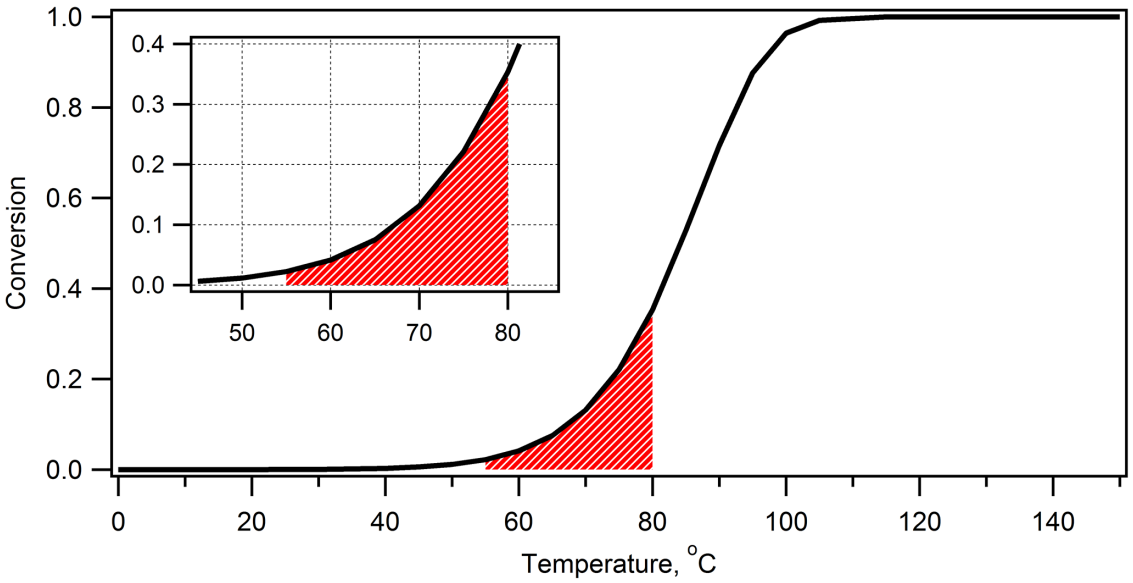

Figure 2.7 – Model of thermal decomposition of PAN to NO_2 with a residence time of 0.96 s at temperatures between 0 and 150 °C. Inset is detail of 45 to 85 °C. The red shaded area corresponds to the temperature range of the UV LEDs of a BLC. Kinetic data from IUPAC (Atkinson et al., 2006).

expressed fractionally. If in fact the conversion efficiency of PAN to NO in the converter was not related to the measured NO_2 to NO conversion efficiency but instead a constant value, then the apparent relationship between CE and percent conversion would disappear. This explanation is consistent with the fact that, when the average conversion percentage in Fig. 2.2 is normalized to conversion efficiency, the percentage for the three BLCs is remarkably similar (Table 2.4) to the average PAN decomposition of 4.6 % needed to produce the spurious signal observed. Above a threshold temperature of 25 °C, the NO_2 formed in Reaction 2.19 may be vibrationally excited (likely NO_2 ($^2A_1$)) through the dissipation of internal energy from the parent PAN molecule (Mazely et al., 1995); this NO_2^* is then more readily photolysed to NO within the BLC than ground-state NO_2. The discussion above suggests that a similar proportion of the NO_2 evolved from thermal dissociation of PAN is converted to NO within the BLC, leading to the apparent inverse correlation between conversion efficiency and PAN "artefact". Consequently, the lower $NO_2 \rightarrow NO$ conversion efficiency of a BLC, the greater the positive error in NO_2 when PAN is present.

Table 2.4 – The average percentage conversion of PAN to NO_2 measured, and normalized to the converter efficiency of each BLC.

	Converter efficiency (%) ±1		
	41	35	22
Measured %	10.8	15.9	19.6
Normalized %	4.4	5.2	4.3

2.6 Atmospheric implications

We have shown that a significant proportion of PAN can be decomposed under the normal operating conditions of a BLC equipped NO chemiluminescence instrument, leading to a spurious increase in measured NO_2 of 8 to 25 % of the PAN supplied. The UV-LED light source was found to reach a temperature of 56 to 80 °C in normal operation, with the surface temperature correlating positively with power draw and output intensity. The elevated temperature of the UV LEDs causes a positive bias in NO_2 by thermal decomposition of PAN.

The positive bias in NO_2 measurements by NO chemiluminescence using BLCs has implications for remote background sites. Figure 2.8 shows the thermal decomposition profiles of many common NO_y species. Whereas only a small fraction of PAN is found to convert to NO_2 at the operating temperatures ($\sim$ 5 % at 60 °C) of the instrument, a number of more thermally labile compounds exist.

The degree of gas-phase thermal decomposition within the instrument will depend upon the thermal profile of the air ($T(t)$) as it passes through the instrument. This can be parameterized as a mixing time-scale (τ s) for temperature from the ambient temperature (T_0) to that of the BLC (T_{BLC}) as in Eq. 2.20.

$$T(t) = T_0 + (T_{\mathrm{BLC}} - T_0) \exp\left(-\frac{t}{\tau}\right) \tag{2.20}$$

The time constant for which thermal equilibrium is reached within the cell, τ, is calculated as 0.42 s from the observed PAN decomposition of 4.6 %, at 20 °C ambient temperature, a BLC temperature of 75 °C, and a 1 s residence time. This allows calculation of the potential interference from other thermally labile NO_y compounds.

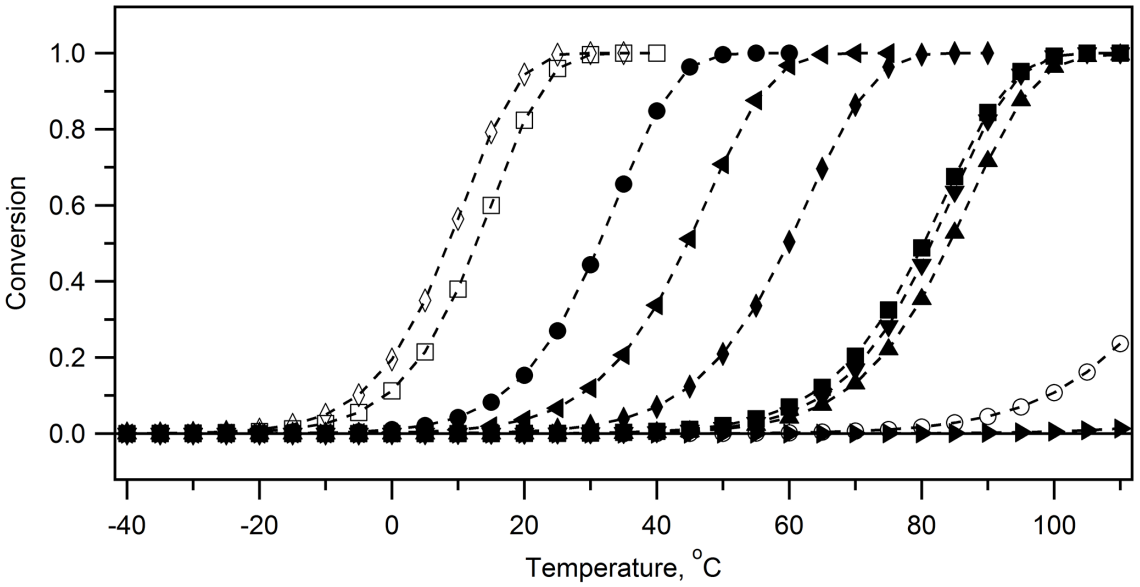

Figure 2.8 – Thermal decomposition profiles of $IONO_2$, ♦; $BrONO_2$, ◯; $ClONO_2$, ►; HO_2NO_2, •; N_2O_5, ◄; $C_2H_5O_2NO_2$, ◇; $CH_3C(O)CH_2O_2NO_2$, □; MPAN, ■; PAN, ▲; and PPN, ▼. Calculated from IUPAC recommended kinetic data (Atkinson et al., 2004, 2006, 2007) using FACSIMILE kinetic modelling software (MCPA Software Ltd.) based on 1 s residence time. Note that $CH_3O_2NO_2$ is not shown but has the same profile as $CH_3C(O)CH_2O_2NO_2$.

Given a first-order loss of the PAN-like compound and a temperature profile within the instrument as described in Eq. 2.20, we have Eq. 2.21:

$$\frac{\mathrm{d[PAN]}}{\mathrm{d}t} = -k(T)[\mathrm{PAN}] = -k(t)[\mathrm{PAN}]. \tag{2.21}$$

Given the laboratory observations of the temperature dependence of the rate constant (typically $k(T) = A\exp(-B/T)$), and the parameterized temperature within the instrument ($T(t)$), the fraction of the compounds that will have decomposed can be found by numerical integration.

Figure 2.9 uses output from the GEOS-Chem model (version 9.2, `http://www.geos-chem.org`; Bey et al. 2001) run at 2° × 2.5° resolution, plus updates described in Sherwen et al. (2016a), to provide an estimate of the interference on NO_2 from the decomposition of NO_y species within a BLC photolytic converter. The species used for this analysis are PAN, MPAN, PPN, $IONO_2$, $BrONO_2$, N_2O_5, $CH_3O_2NO_2$, and HO_2NO_2. Thermal decomposition information are taken from IUPAC evaluated kinetic data (Atkinson et al., 2004, 2006, 2007). Interferences are calculated for each month of a 1-year simulation and the maximum value shown. The estimate assumes a BLC conversion efficiency of 100 % $NO_2 \rightarrow NO$ and thus does not include the extra signal from the photolysis of $NO_2^* \rightarrow NO$

with converters where conversion is less than unity – in this case a multiplying factor exists.

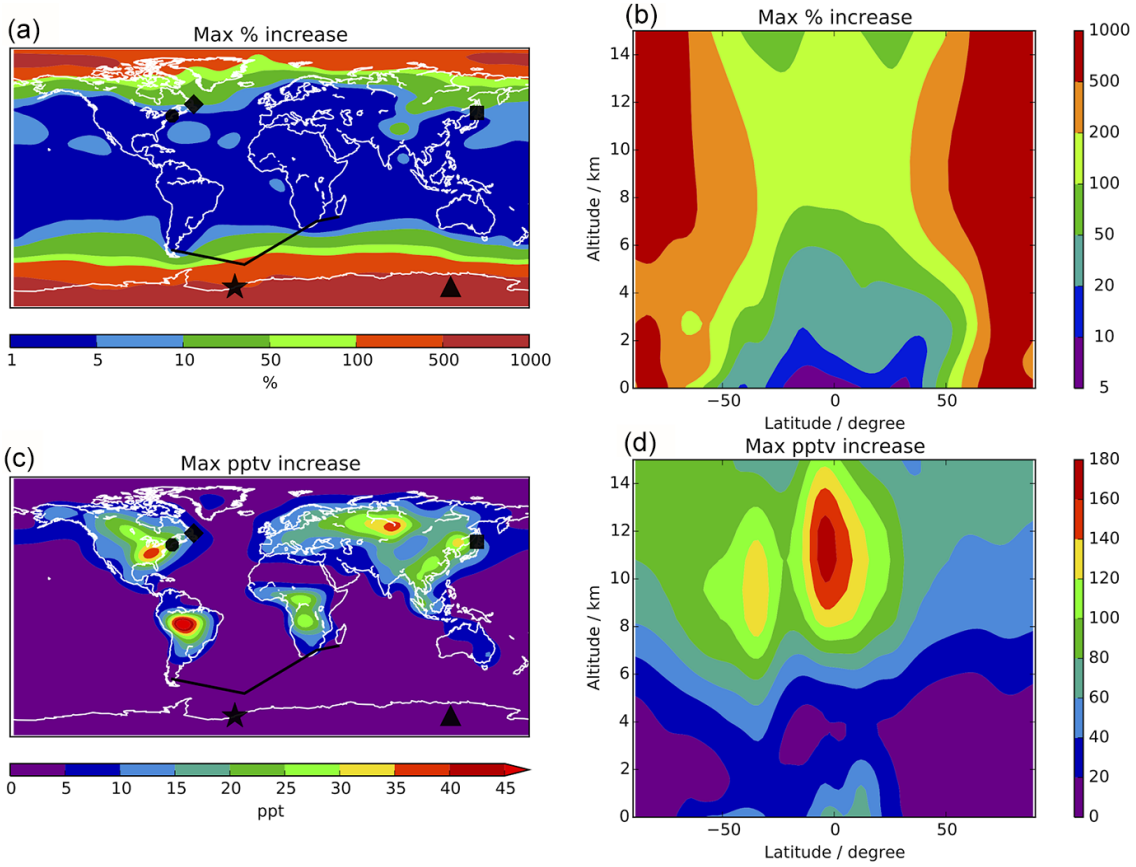

Figure 2.9 – GEOS-Chem model output showing the monthly maximum percentage over-reporting of NO_2 determined by BLC/chemiluminescence **(a)** zonally and **(b)** by altitude in any month of a 1-year simulation. Panels **(c)** and **(d)** show the same in absolute pptV values. Surface values are the maximum over-reporting in any month; zonal values are the maximum over-reporting in any month and in any of the longitudinal grid boxes. The MD160 cruise track of Hosaynali Beygi et al. (2011) is also shown in panels **(a)** and **(c)**, as are the locations of the studies of Bauguitte et al. (2012), ★; Frey et al. (2013, 2015), ▲; Griffin et al. (2007), ●; Kanaya et al. (2007b), ■; and Yang et al. (2004), ♦.

Figure 2.9 shows that in extreme circumstances NO_2 may be over-reported by many hundreds of percent. These are in regions that typically have low NO_x concentrations and are cold (polar), or in the upper troposphere. Here, the concentration of compounds such as PAN and HO_2NO_2 are high relative to NO_x and it is not surprising that thermal decomposition can have an impact. Upper tropospheric overestimates of NO_2 concentrations could be as high as 150 pptV, which we find due to $CH_3O_2NO_2$ abundance, which has previously been identified as a possible interference in NO_2 measurement by LIF and

chemiluminescence (Browne et al., 2011; Nault et al., 2015).

The NO_2 bias shown in Fig. 2.9 impacts the modelled Leighton ratio. In Fig. 2.10 the model is sampled every daylight hour for every surface grid box for the month of March. The calculation shown in red is the Leighton ratio calculated from the modelled concentrations of NO, NO_2, jNO_2, O_3, T, HO_2, RO_2, BrO, and IO. The model values are in general close to 1. In blue the same calculation is performed but including the interferences on the NO_2 channel. The instrumental decomposition of NO_y over a range of BLC lamp temperatures between 20 and 95 °C is shown (described by τ of 0.42 s and a residency time of 1 s). Here there are significant interferences.

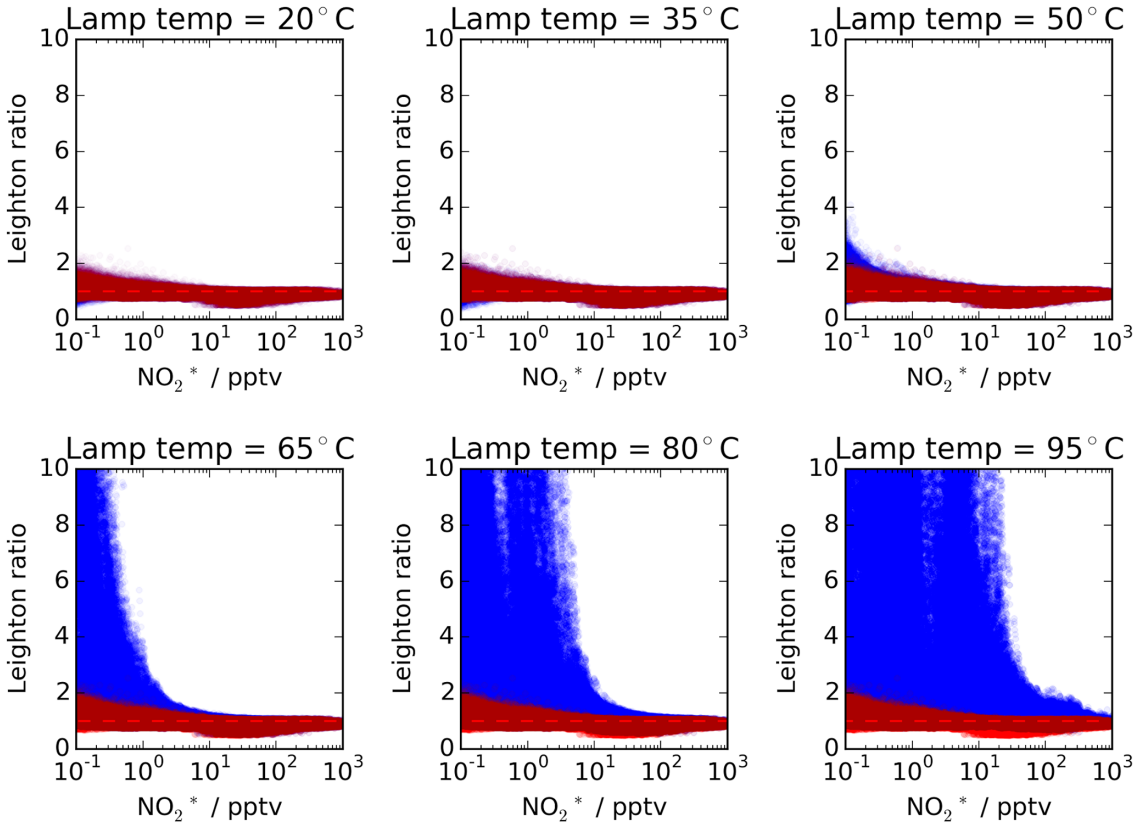

Figure 2.10 – Leighton ratio calculated for each surface model grid-box for each daylight hour for March by the GEOS-Chem model as a function of the grid box NO_2 concentration. The instrument interference is characterized by a numerical solution of Eq. 2.21 with $\tau = 0.42$ s and a residence time of 1 s. Red shows the values calculated without the interference on the NO_2 concentration and blue indicates the values calculated with the interference. The interferences are calculated for different lamp temperatures, 20 to 95 °C.

As shown in Fig. 2.10 the Leighton ratio can be extremely perturbed from what would be predicted for NO_2 converters which operate above ambient temperature. This is especially

true in low-NO_x environments.

Unusual Leighton relationships have been seen in a range of previous studies (Bauguitte et al., 2012; Cantrell et al., 1997, 2003; Frey et al., 2013, 2015; Griffin et al., 2007; Hosaynali Beygi et al., 2011; Kanaya et al., 2007b; Yang et al., 2004), leading to either hypothesizing (a) an unknown, unmeasured, selective oxidant "compound X" or (b) theoretical mechanisms by which NO is converted to NO_2, which may be accounted for, in part, by a previously unaccounted for instrument bias our study has suggested. It is noteworthy that the studies of Bauguitte et al. (2012), Cantrell et al. (2003), Frey et al. (2013, 2015), Griffin et al. (2007), Hosaynali Beygi et al. (2011), Kanaya et al. (2007b), and Yang et al. (2004) were all in locations where we predict a significant interference (indicated in Fig. 2.9), impacting on the observed Leighton relationship and complicating interpretation. However, whether specific NO_2 measurements have been influenced by a thermally labile NO_y bias will depend on the specific instrument conditions and geometries.

2.7 Conclusions

Measurements of NO_2 collected using some types of photolytic converter and chemiluminescence systems may be significantly biased in low-NO_x environments. Thermal decomposition of NO_y species within the NO_2 converter can produce spuriously high readings; this is especially true in pristine environments and at high elevations, where the NO_y to NO_x ratio may be high. Over-reporting of NO_2 has been shown to lead to apparent gaps in oxidation chemistry which cannot be explained with any available measurements. Unexplained high $NO_2 : NO$ ratios in such regions have led to theorization of an unknown "compound X" which selectively oxidises NO to NO_2.

Our study suggests a need for characterization of individual NO_x instruments using the BLC/NO chemiluminescence technique (or similar) with respect to interference from thermally decomposing NO_y species. A convenient method for this would be with a pure PAN source, or any other readily available NO_y species.

In order to mitigate overestimation of the NO_2 mixing ratio by thermally dissociating PAN and other compounds, it is imperative to avoid heating of the sample above ambient. This can be achieved by separating the gas flow from contact with the UV-emitting elements,

and by cooling the photolysis cell. Reducing the residence time of the sample gas within an instrument where it may not be possible to maintain ambient temperature of the sample is an alternative, i.e. where the ambient temperature is infeasibly low. This can be achieved by operating at reduced inlet pressure, with the additional benefit of faster response time. It is desirable to have the highest possible $NO_2 \rightarrow NO$ conversion efficiency, i.e. unity, to minimize uncertainty in NO_2 and to remove any multiplying effect of more easily photolysable vibrationally excited NO_2. It would also seem prudent that the sample gas should contact only chemically inert, non-porous materials in order to mitigate any heterogeneous processes or memory effect – quartz being an ideal material for photolysis cells.

Chapter 3

HONO measurement by differential photolysis

This chapter was presented as an article in the journal Atmospheric Measurement Techniques.

Reed, C., Brumby, C. A., Crilley, L. R., Kramer, L. J., Bloss, W. J., Seakins, P. W., Lee, J. D., and Carpenter, L. J.: HONO measurement by differential photolysis, Atmospheric Measurement Techniques, 9, 2483-2495, doi: 10.5194/amt-9-2483-2016, 2016.

''There is no harm in repeating a good thing."

Plato

3.1 Abstract

Nitrous acid (HONO) has been quantitatively measured *in-situ* by differential photolysis at 385 and 395 nm, and subsequent detection as nitric oxide (NO) by the chemiluminescence reaction with ozone (O_3). The technique has been evaluated by Fourier transform infra-red (FT-IR) spectroscopy to provide a direct HONO measurement in a simulation chamber and compared side by side with a long absorption path optical photometer (LOPAP) in the field. The NO–O_3 chemiluminescence technique is robust, well characterized, and capable of sampling at low pressure, whilst solid-state converter technology allows for unattended *in-situ* HONO measurements in combination with fast time resolution and response.

3.2 Introduction

Nitrous acid (HONO) is a major source of hydroxyl (OH) radicals in the boundary layer (Elshorbany et al., 2009; Kim et al., 2014b; Levy, 1973). HONO can be formed homogeneously through reaction of nitric oxide (NO) with OH, heterogeneously through several pathways, or emitted directly (Kleffmann, 2007; Lammel and Cape, 1996; Spataro and Ianniello, 2014; Su et al., 2011). HONO is formed heterogeneously on surfaces through the reaction of NO_2 with H_2O (Bröske et al., 2003). This heterogeneous formation of HONO is a net source of OH radicals in the troposphere and is an important mediator of air quality, particularly in polluted environments (Finlayson-Pitts et al., 2003; Gutzwiller et al., 2002; Lee et al., 2016). Combustion sources of HONO are direct emission from on-road vehicle exhausts (Rappenglück et al., 2013), aircraft and diesel emissions (Lee et al., 2011a), and biomass burning (Roberts et al., 2010). Emission from snowpack as also been documented (Beine et al., 2008; Zhou et al., 2001), and more recently biogenic sources of HONO have been identified from nitrite-producing bacteria (Oswald et al., 2013; Su et al., 2011) and soil crusts (Weber et al., 2015).

In urban areas HONO can be the major net source of OH (discounting radical cycling driven by e.g. NO), contributing up to 80 % of daytime OH production in winter and 50 % in summer (Elshorbany et al., 2009; Kleffmann, 2007; Villena et al., 2011). However, the sources of HONO and the many processes by which it forms are not well understood (Kleffmann et al., 2006; Sörgel et al., 2011; Spataro and Ianniello, 2014; Villena et al., 2011). There is a clear need for *in-situ* measurement of HONO in order to better understand its chemistry and emissions. Currently, methods of detecting HONO are either remotely through differential optical absorption spectroscopy (DOAS, Febo et al. 1996; Hendrick et al. 2014; Stutz et al. 2010) or by filter/denuder sampling (Acker et al., 2005, 2006; Febo et al., 1993, 1996; Ianniello et al., 2007). A variety of *in-situ* techniques exist: namely, quantum cascade–tuneable infra-red laser differential absorption spectrometry (QC-TILDAS, Lee et al. 2011b), ion drift chemical ionization mass spectrometry (ID-CIMS, Levy et al. 2014), ambient ion monitor–ion chromatography (AIM-IC, Markovic et al. 2012; VandenBoer et al. 2014), stripping coil–visible absorption photometry (SC-AP, Ren et al. 2011), negative-ion proton-transfer chemical ionization mass spectrometry (NI-PT-CIMS, Roberts et al. 2010), incoherent broadband cavity-enhanced absorption

spectroscopy (IBBCEAS, Pusede et al. 2014), and, as used in this study, long path absorption photometry (LOPAP, Heland et al. 2001). LOPAP has been characterized quite extensively by other authors (e.g. Clemitshaw 2004; Kleffmann and Wiesen 2008; Kleffmann et al. 2006, 2013; Ródenas et al. 2013).

Here, we demonstrate the exploitation of a known HONO interference for photolytic NO_2 conversion systems (Pollack et al., 2011; Ryerson et al., 2000; Sadanaga et al., 2010, 2014; Villena et al., 2012) to provide a simple photolytic technique for quantitative analysis of HONO.

3.3 Experimental details

The differential photolytic HONO technique, henceforth referred to as pHONO, was developed from an existing fast NO_x analyser, described in Sect. 3.3.1. The photolytic converter is described specifically in Sect. 3.3.2. Characterisation and calibration are described in Sects. 3.3.3 and 3.3.4. The precision, limit of detection, artefacts, interferences, and uncertainties are described in Sects. 3.3.5 and 3.3.6.

3.3.1 Differential photolysis instrument

Measurements were performed using a dual-channel Air Quality Design Inc. (Golden, Colorado, USA) instrument equipped with a UV-LED-based photolytic NO_2 converter – commonly referred to as a blue-light converter (BLC) as described in chapter 2.

Briefly, a dual-channel NO chemiluminescence analyser operates in parallel with duplicated independent equipment. The two channels share a common inlet allowing for parallel calibration. One channel is equipped with a photolytic NO_2 converter so that NO_x can be determined with that channel whilst also measuring NO concurrently. This allows for fast (1 Hz or greater) determination of NO and NO_2. A chemiluminescent zero is taken every 5 min by increasing the $NO + O_3$ reaction time. Practically, the sample flow is diverted to a PFA volume so that $> 99\,\%$ of NO is converted, any residual chemiluminescence signal arises therefore from slower (~ 2 orders of magnitude) $O_3 +$ alkene reactions (Drummond et al., 1985).

In order to be able to also measure HONO, the NO_x channel was redesigned so that the photolytic converter (Sect. 3.3.2) operates in a switching mode. That is, the two lamps of different wavelengths operate alternately on a 50 % duty cycle. The lamps switch every 30 s, allowing for 1 min time resolution data.

3.3.2 NO_2–HONO photolytic converter

Photolytic converters were based on those supplied by Air Quality Design and manufactured according to their proprietary standards (Buhr, 2004, 2007), and they are described in chapter 2. Two UV-LED arrays are positioned at opposing ends of a cavity which is highly reflective to UV. Sample gas is introduced at one end of the illuminated cavity, exiting at the other. NO in the sample exiting the converter is enhanced over the original by photolysis of NO_2 or HONO, thus by calibration of the conversion efficiency these can be quantified.

Modifications were made to the control of the UV-LED elements to allow independent switching of the lamps. The wavelength of one lamp was changed from standard (395 nm) to 385 nm in order to overlap better with the HONO absorption spectrum, whilst the actual UV-LEDs (3 W, LED Engin, Inc.) are more efficient and higher powered than those used in chapter 2.

The volume of the illuminated sample chamber is 16 mL, which, with a standard flow rate of 1 standard L min^{-1}, gives a sample residence time of 0.96 s, assuming plug flow, at standard atmospheric temperature and pressure (SATP). The $NO_2 \rightarrow NO$ conversion efficiency of the standard BLC with the sample flow of 1 standard L min^{-1} was ~ 89 % with both lamps illuminated. Individual lamp conversion efficiencies were 72.9 and 81.3 % $\pm$ 0.1 for the 385 and 395 nm lamps, respectively. Determination of the conversion efficiency is detailed in Sect. 3.3.3.

3.3.3 Characterisation

Spectral radiograms of the UV-LED output were obtained using the same procedure and equipment described in chapter 2 using an Ocean Optics QE65000 spectral radiometer coupled to a 2π quartz collector within a light-sealed chamber. Figure 3.1 shows the

measured spectral emission of two UV-LED units of two different wavelengths, 385 and 395 nm. Also shown is the absorption cross section of HONO, $BrONO_2$, and the NO_2 quantum yield (Burkholder et al., 2015).

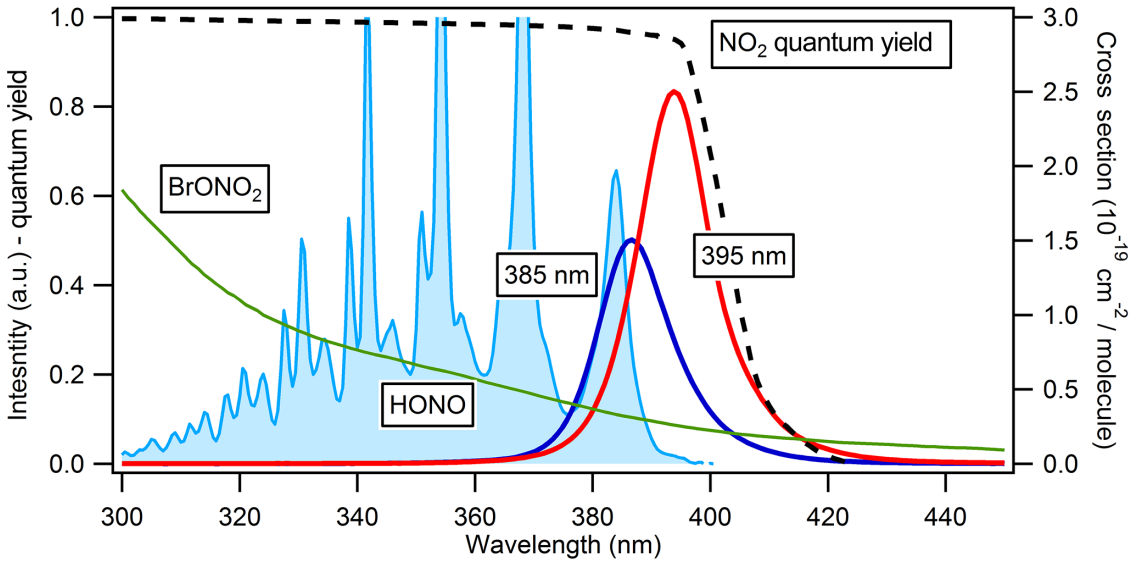

Figure 3.1 – The measured spectral output of two UV-LED elements, nominally 385 nm output in dark blue and 395 nm in red. The HONO absorption spectrum is shown in light blue, whilst the NO_2 quantum yield is shown in dashed black. The absorption cross section of $BrONO_2$ is shown in green.

It is clear that there is greater overlap, calculated to be 30 %, of the HONO absorption features with the 385 nm LED than at 395 nm. In reaction 3.2 we see that NO is produced stoichiometrically through the photolysis of HONO. In this way, illuminating an air sample at either wavelength yields a signal, which we shall denote as $NO_2^\dagger$ and which represents the sum of contributions from NO_2 and HONO (Reactions 3.1 + 3.2) in differing proportions depending upon wavelength.

$$NO_2 + h\nu\,(<410\,\text{nm}) \rightarrow NO + O(^3P) \tag{3.1}$$

$$HONO + h\nu\,(<390\,\text{nm}) \rightarrow NO + OH \tag{3.2}$$

The difference in $NO_2^\dagger$ signal measured at 385 and 395 nm corresponds to the difference in conversion efficiency of HONO and NO_2 between the two wavelengths. Differences in NO_2 conversion efficiency of each lamp may be readily calibrated for and so taken into account (see Sect. 3.3.4). The difference in $NO_2^\dagger$ signal measured at 385 and 395 nm can

therefore be used to calculate the HONO present in the sample Eq. 3.3:

$$\frac{{NO_2}^{\dagger}{}_{385} - {NO_2}^{\dagger}{}_{395}}{\text{HONO CE}_{385} - \text{HONO CE}_{395}} = [\text{HONO}] \tag{3.3}$$

Apparent HONO conversion efficiency (CE), HONO CE_{385}–HONO CE_{395}, is determined experimentally as described in Sect. 3.3.4.

3.3.4 HONO and NO_2 conversion efficiencies

The NO_2–HONO converter system was calibrated for both NO_2 and HONO conversion efficiency. NO_2 conversion efficiencies were determined following the procedure outlined by Lee et al. (2009). Conversion efficiency is the proportion of reactants (NO_2 or HONO) from Reactions 3.1 and 3.2 which are photolysed to NO. This is dependent on the $j\text{NO}_2$ and jHONO of the UV source, the residence time, and the concentration of oxidants of NO in the photolysis cell as described by Eq. 3.4, (Ryerson et al., 2000). Here t is the residence time within the photolysis cell, and $k[\text{Ox}]$ is the concentration and rate constant of any oxidant that reacts with NO. Typically this would be ozone, however, OH formed from HONO photolysis must also be considered.

$$\text{CE} = \left[\frac{jt}{jt + k\,[\text{Ox}]\,t}\right]\left[1 - \exp^{(-jt - k[\text{Ox}]t)}\right] \tag{3.4}$$

The NO + OH back reaction occurs after an air sample has exited the photolytic converter but before entering the high vacuum of the analyser, causing a decrease in signal from HONO as discussed in Sect. 3.3.6. A similar reaction of $\text{NO} + \text{O}_3$ also occurs, however this is ~ 3 orders of magnitude slower than NO + OH (Atkinson et al., 2004) and insignificant on the short (0.11 s) time-scale in our instrument.

The sensitivity of a detector in counts per second per part per trillion (cps / ppt) is determined by adding a 7.5 mL min^{-1} mass-flow-controlled flow (MFC) of NO calibration gas (4.78 ppm NO in N_2, BOC) to the inlet of the analyser whilst sampling an overflow of zero air free from NO_x, VOC, and ozone. This equates to a calibration concentration of 12.5 ppbV NO per channel. Zero air was generated by scrubbing dried (-40 T_d) compressed air using Sofnofil (Molecular Products) and activated charcoal (Sigma Aldrich) traps. As described in chapter 2, this combination results in the lowest NO_2 signal. The sensitivity was ~ 6.8 and ~ 6.4 (± 5 %) cps / ppt for the NO and NO_x channels, respectively. In order to determine the NO_2 converter efficiency, a portion of the NO added to the inlet

is first titrated to NO_2 by reaction with ozone, typically generating 10.0 ppbV NO_2. Ozone is generated by illuminating a small flow ($\sim 10\,mL\,min^{-1}$) of O_2 with a broad-output low-pressure mercury UV lamp (BHK Inc.) The analyser signal (photomultiplier counts in Hz) is then recorded with neither UV-LED illuminated and then with each illuminated in turn to determine the increase in signal arising for each lamp. The conversion efficiency (CE) is then determined as in Eq. 3.5, where, when calibrating in zero air or at high mixing ratios relative to the measurement, ambient (Amb) values may be neglected. Ambient signals must be considered when calibration and measurement levels are comparable, and in a changing background.

$$CE = 1 - \frac{(NO.Hz_{Untitrated} - NO.Hz_{Amb.1}) - (NO_x.Hz_{Illuminated} - NO_x.Hz_{Amb})}{(NO.Hz_{Untitrated} - NO.Hz_{Amb.2}) - (NO.Hz_{Titrated} - NO.Hz_{Amb.3})} \quad (3.5)$$

The NO_2 conversion efficiency was determined to be 72.9 % ($j = 1.3\,s^{-1}$) and 81.2 % ($j = 1.7\,s^{-1}$) ± 0.1 for the 385 and 395 nm lamps, respectively.

Calibration for HONO was achieved by sampling a permeation source over a range of dilutions using methods modified from Taira and Kanda (1990) and Febo et al. (1995). Nitrous acid was generated by the reaction of hydrochloric acid with sodium nitrite salt as described by Febo et al. (1995), shown in Reaction 3.6.

$$HCl + NaNO_2 \rightarrow HONO + NaCl \quad (3.6)$$

In order to achieve a continuous source of HONO, a permeation tube (Kin-Tek, HRT-010.00-BLANK/U) was filled with HCl (37 %, Fluka, AR grade) and placed in a thermostated (30 to 55 °C) permeation oven (Kin-Tek, 585) with $NaNO_2$ salt (Fluka, AR grade). The permeation oven was flushed with 1.5 standard $L\,min^{-1}$ zero air. The reaction is limited by HCl which permeates at a low rate thus allowing low concentrations (< 50 ppb) of HONO to be generated continuously.

As side products of Reaction 3.6 can also be produced, the output of the permeation source was continuously analysed for impurities. In Reaction 3.7 NO and NO_2 can be formed by the gas phase self-reaction of HONO. In Reaction 3.8, HNO_3 can be formed by reaction between adsorbed and gas phase HONO.

$$2\,HONO_{(g)} \rightarrow NO + NO_2 + H_2O \quad (3.7)$$

$$HONO_{(ads)} + NO_2 \rightarrow HNO_3 + NO \quad (3.8)$$

To quantify HONO without any direct measurement and close the nitrogen balance, NO, NO_2, and total NO_y ($NO + NO_2 +$ other reactive oxidized nitrogen species such as HNO_3, HONO, PAN) were measured continuously. The differential photolysis instrument itself was used to quantify the NO. NO_2 was measured directly using an EPA certified Teledyne API T500U which uses Cavity Attenuated Phase Shift (CAPS) spectroscopy from Aerodyne Research Inc. (Kebabian and Freedman, 2007; Kebabian et al., 2005, 2008), to avoid any HONO interference which would have been present in a photolytic measurement. This is because the T500U uses a 450 nm band-pass for NO_2, whereas HONO absorbs only below 390 nm as shown in Fig. 3.1. Glyoxal is a possible interference in the CAPS technique as it also absorbs in the 440–460 nm range (Volkamer et al., 2005), however all VOC are scrubbed from the zero air during calibration. The nitrate radical (from particulate nitrate) is also an interference in the CAPS technique as it absorbs above ~ 400 nm (Stark et al., 2007), however the T500U is fitted with a high-efficiency particulate air (HEPA) filter to mitigate this. Nitric acid which absorbs below 340 nm (Rattigan et al., 1992) is also not an interference. Total NO_y was quantified using a Thermo Environmental 42c TL NO_x analyser equipped with a molybdenum catalytic converter which has been shown to quantify NO_y species such as HONO and HNO_3 (Clemitshaw, 2004; Fehsenfeld et al., 1987; Villena et al., 2012; Williams et al., 1998). The TEI 42c TL and Teledyne API T500U were calibrated either directly with an NO standard or by gas phase titration of NO to NO_2 using a Monitor Europe S6100 Multi Gas Calibrator. Production of HNO_3 (Reaction 3.8) would be indicated by an enhancement in NO over NO_2, as NO and NO_2 are produced stoichiometrically through the self-reaction of HONO (Reaction 3.7, whereas HNO_3 production consumes NO_2 and produces NO. Thus, HNO_3 can be indirectly quantified by the $NO : NO_2$ ratio, and was found to be a minimal contribution to total NO_y. As such, HONO can reasonably be presumed to be equivalent to $[NO_y] - ([NO] + [NO_2] + [HNO_3])$. Measured quantities are shown in Table 3.1.

The stability of the HONO permeation source was recorded over a 12 h period using NO_x measured by the differential photolysis analyser (the most sensitive measurement available) as a proxy for NO, NO_2, and HONO. The stability was found to be ± 0.01 ppb h^{-1}, with a standard deviation of 0.4 ppb. The uncertainty in the HONO source is determined by a combination of the accuracy of the NO, NO_2, and NO_y measurements and their respective calibrations. The NO calibration uncertainty, due to MFC flows and standard gas accuracy is 5 %, similarly for the CAPS NO_2 and Thermo 42i TL NO_y. This results in an overall

Table 3.1 – Showing the distribution of NO_y species NO, NO_2, HNO_3, and HONO produced from the HONO permeation source.

No.	NO_y ppb measured	NO ppb measured	NO_2 ppb measured	HNO_3 ppb calculated	HONO ppb calculated
1	20.40	3.34	2.64	0.35	14.08
2	19.29	2.96	2.35	0.30	13.68
3	16.82	2.59	2.10	0.26	11.89
4	14.95	2.27	1.87	0.20	10.62
5	13.40	2.05	1.73	0.16	9.45
6	12.15	1.86	1.58	0.14	8.57
7	11.09	1.70	1.46	0.12	7.81
8	10.17	1.60	1.35	0.11	7.14
Percent	–	15.5	12.8	1.3	70.4

uncertainty in [HONO] of 8.7 %.

In Fig. 3.2 the observed conversion of HONO, that is the difference between HONO conversion by the 385 and 395 nm lamps, is shown. As can be seen HONO conversion is consistently 6.54 ± 0.21 % more at 385 nm than 395 nm. The fact that the "apparent HONO conversion" (HONO CE_{385} – HONO CE_{395} in Eq. 3.3) is constant as a function of HONO means that the determination of [HONO] should be a linear function of the difference in $NO_2^\dagger$ signal at 385 and 395 nm.

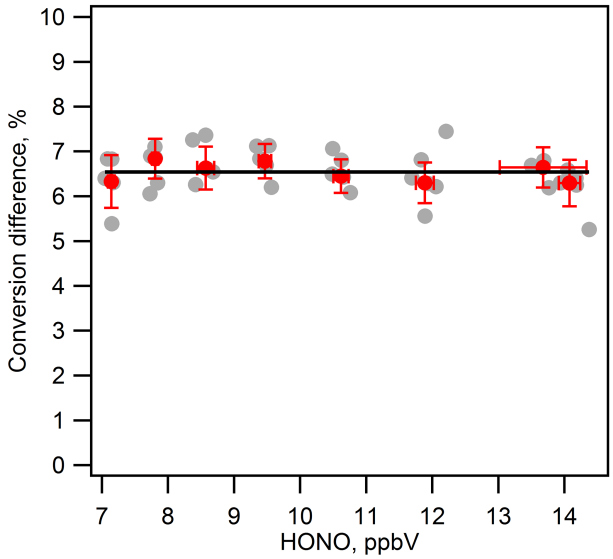

Figure 3.2 – Difference in HONO conversion between 385 and 395 nm UV-LEDs over a range of dilutions. Median values are in red, whilst all data are shown in grey. Linear fit is in black, error bars show standard deviation of the mean values.

3.3.5 Measurement precision and limit of detection

The precision of NO chemiluminescence detection is the ability to discriminate signal from photon counting noise. The photon counting noise is taken as the standard deviation of the pre-chamber zero signal (determined every 5 min as described in Sect. 3.3.1) in Hz (counts per second) divided by the sensitivity in cps pptV^{-1}. The average zero count rate was $\sim$ 3000 Hz on both channels with a 1 σ standard deviation of $\sim$75 Hz, giving a precision for NO of 11.0 and 11.7 pptV for 1 s data with sensitivities of 6.8 and 6.4 cps pptV^{-1} for channels 1 and 2, respectively. The precision for NO_2 and HONO (channel 2) must be divided by their conversion efficiencies. This results in a precision for NO_2 of 16.0 and 14.4 pptV for 1 s data at 385 and 395 nm, respectively. The HONO precision is calculated from the (constant) differential conversion efficiency as 179.9 pptV for 1 s data.

The limit of detection is defined as the precision multiplied by $1/\sqrt{n}$, where n is the number of data points (Lee et al., 2009). For 1 min data the LOD for NO is 1.4 pptV. As the NO_x channel operates on a 30 s switching cycle, the 1 min data are actually only averaged over 30 s. Thus, the 1 min NO_2 limit of detection is 2.6 pptV (calculated from the CE of the 395 nm lamp), and the limit of detection of HONO is 32.8 pptV averaged over 1 min. However the HONO limit of detection must also account for the NO_2 limit

of detection at both 385 and 395 nm, resulting in an overall HONO LOD of 38.3 pptV averaged over 1 min.

3.3.6 Measurement artefacts, interferences, and uncertainties

It is noted that at both 385 and 395 nm there is potential photolytic interference from $BrONO_2$ (or in fact any other compounds which photolyse to give NO at either wavelength), with similar spectral overlap (Fig. 3.1). Assuming a quantum yield of 1 integrated over all wavelengths for $BrONO_2$, 21.5 ppt of $BrONO_2$ at 385 nm and 18.1 ppt at 395 nm would be required to produce a 1 ppt error in the NO_2–HONO signal. Due to the low abundance (< 10 pptV) of $BrONO_2$ in the lower atmosphere (Yang et al., 2005), interference is therefore likely to be minimal (Pollack et al., 2011). The difference in conversion for the different lamps equates to a maximum error in HONO determination of 3.4 % [$BrONO_2$]: typically much less than 1 pptV.

Thermal interferences can also become apparent if the photolytic converter raises the temperature of the sample gas above ambient (see chapter 2). Thermally labile NO_y compounds, e.g. peroxyacetyl nitrate, may decompose within the converter, resulting in a positive signal when measuring in NO_x mode. This will be true at either 385 or 395 nm wavelengths. Under the reasonable assumption that the temperature of the photolysis cell is the same at both wavelengths, then, as shown in chapter 2, the interference scales with NO_2 conversion efficiency. In this case the difference in thermal interference at 385 nm is 10.2 % greater than at 395 nm owing to having a lower NO_2 conversion efficiency. This represents a small bias in the HONO measurement, which can be eliminated by having NO_2 conversion efficiencies equal at both wavelengths as was the case during field measurements in Sect. 3.4.2. When NO_2 conversion efficiencies are equal, thermal interferences affect only the NO_2 measurement, when they are unequal, some uncertainty proportional to the difference in NO_2 CE is introduced.

Zero offset artefacts have been shown to manifest in photolytic converters (Gao et al., 1994; Del Negro et al., 1999; Pollack et al., 2011; Ryerson et al., 2000). That is, when sampling NO_x-free synthetic air, a non-zero signal is observed when the photolytic converter is illuminated. This is attributed to NO_x production from species adsorbed on the walls of the photolytic converter once illuminated by UV (Pollack et al., 2011). These artefacts

were accounted for during calibration by sampling an overflow of NO_x-free zero air whilst recording the analyser signal when the photolysis cell was illuminated at 385 and 395 nm. The artefacts were found to be 368 and 319 ($\pm 5\,\%$) pptV, respectively. There was 0 pptV artefact in NO. UV-induced artefacts vary with time (Ryerson et al., 2000) and have intrinsic uncertainty in their determination, they thus contribute to overall measurement uncertainty.

This spurious artefact signal can be minimized by periodic cleaning of the inside of the photolysis cell (Pollack et al., 2011; Ryerson et al., 2000), by choice of cell material (see chapter 2), and by lensing the UV light so as not to illuminate the walls of the cell – sacrificing some conversion efficiency (Ridley et al., 1988).

The effect of the back reaction of OH + NO to reform HONO before detection of NO, thus reducing the NO signal in the NO_x–HONO measurement in the presence of HONO, is another possible source of uncertainty. As a greater proportion of HONO is photolysed at one wavelength respective to another, the sample inside and exiting the converter necessarily has differing OH concentrations. The effect on the NO signal detected was calculated using a box model in FACSIMILE kinetic modelling software (MCPA Software Ltd.). Kinetic data for O_x, HO_x, and NO_x reactions are taken from IUPAC Evaluated Kinetic Data (Atkinson et al., 2004). The box model was initiated with the NO, NO_2 HONO, and HNO_3 concentrations shown in Table 3.1. NO, NO_2, O_3, and OH concentrations at the outlet of the photolysis cell after 1 s illumination at each wavelength were calculated. The residence time between an air sample exiting the photolysis cell and entering the high vacuum of the NO analyser through the ~ 25 cm of 1/4 in. PFA tubing is 0.11 s. The air sample is a mixture of mostly NO, O_3, OH, and unconverted NO_2. The absence of UV irradiation results in chemistry analogous to night-time NO_x chemistry with the addition of a significant OH source. The interference from the OH + NO reaction was determined as the decrease in [NO] during the 0.11 s residence time as a percentage of measured [HONO]. The discrepancy was calculated to vary linearly with [HONO] from -0.97 to $-2.10\,\%$ over the range of calibrations, with differences between lamps well within the accuracy of the calibration. The degree of interference from OH in NO_2 and HONO determination was found to be a function of $k([\mathrm{OH}] + [\mathrm{NO}])$ on the time-scale here (0.11 s). Reducing the residence time after the photolysis cell would reduce the error in HONO and NO_2 (in the presence of HONO). Conversely, a system with a suitably long residence time

between the photolysis cell and detector may experience little-to-no HONO interference as the $OH + NO$ back reaction begins to dominate. There is of course a trade-off in that the data must be corrected for ambient ozone affecting the $NO : NO_2$ ratio. It is important to note that there can never be any negative interference in NO_2 caused by the presence of HONO, only positive or none.

Outside of calibration the effect of the OH back reaction with NO is likely to be less significant due to the presence of volatile organic compounds (VOCs) which also react with OH with comparable rates to NO. It is therefore difficult to know the absolute HONO conversion of each UV-LED without very accurate OH reactivity/VOC concentration measurements. Due to these unknowns, it would not be possible to correct the NO_2 signal for HONO interference as might be hoped.

Additional uncertainties arise in the HONO measurement from sampling a changing $NO_2^\dagger$ background. Changes in signal when illuminating a sample at 385 nm cannot be attributed to NO_2 or HONO without also knowing the corresponding signal at 395 nm which necessarily is measured at different time. This uncertainty can be reduced by increasing the differential conversion (which was 6.54 % in our system). We make the first order assumption that the NO_2 or HONO background changes on slower time-scales than the instrument response, and that it does not change over the course of two 30 s cycles.

Thus, the uncertainty in the differential conversion is a combination of the uncertainty in the HONO calibration source (8.7 %), the uncertainty of the sensitivities (5 %), NO_2, and HONO conversion efficiencies (5 %), and the uncertainty in the artefact (5 %). This results in an overall root sum of squares uncertainty of 15.8 % in [HONO].

3.4 Results and discussion

The pHONO instrument was evaluated in an atmospheric simulation chamber (Sect. 3.4.1) and compared in the field side by side with LOPAP (Sect. 3.4.2).

3.4.1 Chamber measurements

The Highly Instrumented Reactor for Atmospheric Chemistry (HIRAC) is a simulation chamber facility based at the School of Chemistry, University of Leeds (Glowacki et al., 2007a). HIRAC is a cylindrical stainless-steel chamber with a total volume of $\sim 2.25\,\mathrm{m}^3$, containing four fans for mixing throughout the chamber, and with a total mixing time of $\sim 60\,\mathrm{s}$. The stainless-steel structure of HIRAC allows for pressure-dependent experiments to be carried out, over the range of ~ 0–$1000\,\mathrm{mbar}$. Numerous sample ports are located around the chamber allowing the attaching of instruments or introduction of gas. A multi-pass Fourier transform infra-red (FT-IR) instrument (Bruker IFS/66, 128.52 m path length) is present to allow spectra of the gas within the chamber to be taken (Glowacki et al., 2007b). HIRAC is also capable of operating over a range of temperatures (-40 to $70\,^{\circ}\mathrm{C}$).

Experiments were carried out at ambient temperature ($20\,^{\circ}\mathrm{C}$) and pressure ($1000\,\mathrm{mbar}$), whilst the chamber was kept dark. HIRAC was filled with 80 % N_2 (BOC, UHP, 99.998 %) and 20 % O_2 (BOC) before HONO was synthesized external to the chamber following a modified procedure described previously by Taira and Kanda (1990). A 1 % aqueous sodium nitrite solution was added drop-wise to a 30 % aqueous solution of sulphuric acid. The resulting Reaction 3.9 produces HONO, which was added directly to the chamber via a continuous flow of N_2 over the reaction mixture. This is analogous to the permeation source, however, side products need not be considered due to the direct HONO measurement afforded by FT-IR.

$$2\,\mathrm{NaNO_2} + \mathrm{H_2SO_4} \rightarrow 2\,\mathrm{HONO} + \mathrm{Na_2SO_4} \tag{3.9}$$

FT-IR spectra were taken at 60 s intervals with a spectral resolution of $1\,\mathrm{cm}^{-1}$, whilst the differential photolysis analyser sampled from the chamber. Dilution of the HONO–NO–NO_2 mixture was achieved by partial evacuation of the chamber and subsequent refilling with synthetic air (N_2/O_2). The average HONO concentration determined from the average of two distinct absorbance lines at $1264\,\mathrm{cm}^{-1}$ (*trans*-HONO, Q-branch) and $853\,\mathrm{cm}^{-1}$ (*cis*-HONO, Q-branch) in the FT-IR using absolute line strength data from Barney et al. (2000). The absorptivity data were $5.22 \pm 0.52 \times 10^{-19}\,\mathrm{cm}^2\,\mathrm{molecule}^{-1}$ ($1264\,\mathrm{cm}^{-1}$, *trans*-HONO) and $9.00 \pm 0.90 \times 10^{-19}\,\mathrm{cm}^2\,\mathrm{molecule}^{-1}$ ($853\,\mathrm{cm}^{-1}$, *cis*-HONO). Barney et al. (2000) showed there to be discrepancies between various published line strengths, as did

Lee et al. (2012), thus there is some inherent uncertainty in the absolute [HONO] determined by FT-IR. Some of the spectra used in quantification are shown in Fig. 3.3.

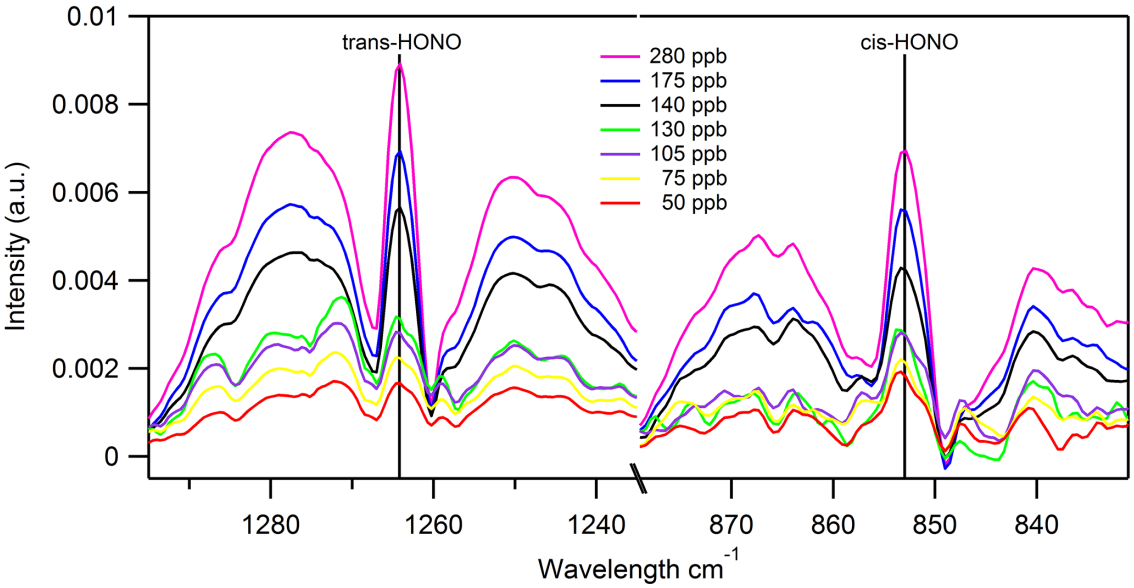

Figure 3.3 – FT-IR spectra of dominant HONO absorbance lines at 1264 and 853 cm^{-1} over a range of concentrations.

Figure 3.4 shows the strong positive correlation between the HONO measured by differential photolysis and by FT-IR within the HIRAC chamber up to $\sim$140 ppbV, deviating at higher mixing ratios. Systematic offset between the pHONO and FT-IR can be attributed to uncertainties in the FT-IR line strength data for HONO and the uncertainty in the pHONO calibration as indicated by the x (15.8 %) and y (10.0 %) error bars. However, the data lie close to or on the 1 : 1 correlation line when these uncertainties are included. Studies have also shown there to be large discrepancies between different published line strengths for HONO (Barney et al., 2000; Lee et al., 2012), which constitutes a greater uncertainty in [HONO] derived by FT-IR of up to +33 % and −25 to −30 % (Barney et al., 2000) depending on the particular cross section used.

Figure 3.4 shows that at lower HONO mixing ratios, $<$ 140 ppb, there is better agreement between the pHONO and FT-IR measurements, whereas the response of the differential photolysis technique appears to be suppressed at high [HONO]. This is a result of how a photolytic converter operates as expressed by Eq. 3.4 in Sect. 3.3.4. Having two LEDs with different HONO absorption overlap results in two values for j(HONO). Using the $j(\mathrm{NO_2})$ values already found (1.3 and 1.7 s^{-1}) as an easily determined proxy for j(HONO), the change in conversion with oxidant concentration can be approximated.

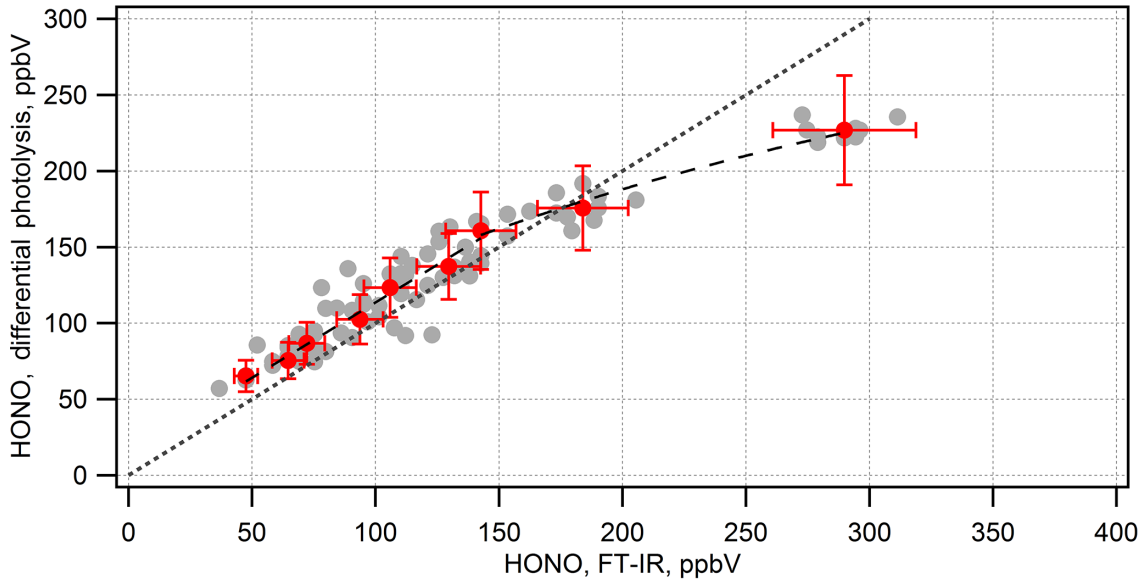

Figure 3.4 – HONO determined by FT-IR (y axis) versus HONO measured by the photolytic/chemiluminescence differential photolysis instrument (x axis). Median values at each dilution are in red, all values are shown in grey. The 1 : 1 line is shown for reference as well as an exponential fit above 140 ppbV HONO. Error bars show the 15.8 % calibration uncertainty of the pHONO instrument and the 10.0 % uncertainty in the FT-IR cross section (Barney et al., 2000).

Figure 3.5 shows how the percentage conversion of any precursor that dissociates to NO, in this case HONO and NO_2, changes with increasing oxidant concentration. In the case of O_3 the total conversion decreases linearly with increasing [Ox], whilst the difference between the two remains constant (9 %). Conversely, with OH, conversion decays exponentially in total, and as a difference between two LEDs of different j. This effect can be seen clearly above 150 ppbV HONO in Fig. 3.4. Below 140 ppbV a constant difference in conversion of 6.54 % is a reasonable approximation.

The high HONO mixing ratios within HIRAC, necessary to be detected by FT-IR (LOD $\sim$40 ppb), were several orders of magnitude higher than would be expected in the atmosphere where ppt (Beine et al., 2006; Ren et al., 2010; Zhang et al., 2009, 2012) to low ppb (Acker et al., 2006; Febo et al., 1996; Hendrick et al., 2014; Kanaya et al., 2007a; Stutz et al., 2004) are typical. Thus, this non-linearity at high [HONO] is unlikely to pose a serious limitation of the differential photolysis method, with the possible exception of areas with very high NO_x backgrounds. This could be partially mitigated by having greater photolysis power at 385 nm, in combination with moving to shorter wavelengths with better overlap with the HONO absorption cross section. It is clear in Fig. 3.1 that

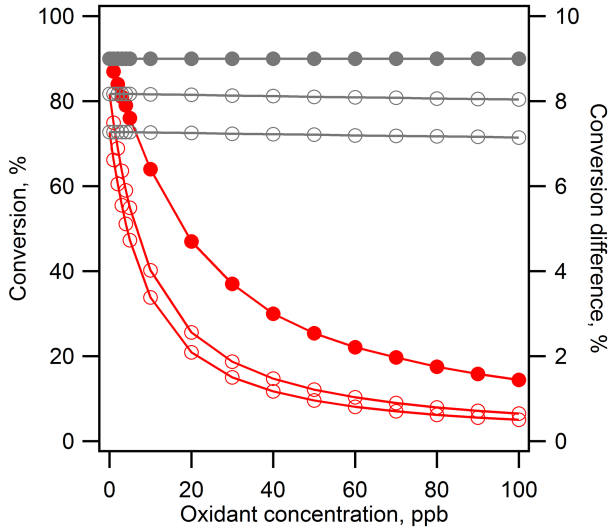

Figure 3.5 – Simulated conversion (open circles) and difference in conversion (closed circles) for photolytic converters with different j in the presence of OH (red) and O_3 (grey) oxidants.

the 385 nm UV-LED has significantly lower light output than at 395 nm, this is reflected in their respective NO_2 conversion efficiencies (72.9 and 81.3 %). Alternatively, separate 385 and 395 nm converters can be employed working in parallel, thus doubling the number of UV-LEDs and doubling the photolysis power at each respective wavelength. This would also allow for fast measurement simultaneously, i.e. 1 Hz or faster. Alternatively, the lower conversion efficiency at high [HONO] could be calibrated for, though, as shown in the following section, in typical atmospheric conditions no calibration or correction was required.

3.4.2 Field measurements

The Weybourne Atmospheric Observatory (WAO, Penkett et al. 1999) is a regional Global Atmosphere Watch (GAW) station located on the North Norfolk coast, UK 52°57′01.5″ N 1°07′19″ E). The WAO has a long history of atmospheric measurements stretching back to its inception in 1994. During summer 2015, the WAO was host to the Integrated Chemistry of Ozone in the Atmosphere (ICOZA) campaign, ostensibly measuring ozone production rates. As part of the campaign a long path absorption photometer (LOPAP-03, QUMA Elektronik & Analytik GmbH, Heland et al. 2001) was deployed in order to measure HONO. Alongside the LOPAP, the NO, NO_2, HONO (differential photolysis) instrument described in Sect. 3.3.1 measured at a 1 min time resolution.

During the ICOZA campaign, a high variation of HONO concentrations (up to ~ 500 pptV) were observed by the LOPAP between 29 June and 7 July, providing an ideal opportunity for comparison between the two methods. The pHONO was deployed with replacement UV-LEDs with greater output. Both the 385 and 395 nm lamps had the same photon flux, indicated by identical individual NO_2 conversion efficiencies ($\sim 89\,\%$), in the expectation that better HONO conversion, and therefore sensitivity, would be achieved. The estimated increase in overlap with the HONO adsorption spectrum of the new 385 nm LED was 45 %, compared to 30 % calculated for the original LED. Thus lamps were installed as is without calibration to mitigate the fall in output over time that affects the LEDs, particularly the 385 nm LED. The decreasing output is believed to be a result of the power control circuitry of the LEDs which does not limit the current draw immediately after power is supplied, only after a few seconds. This means every time the lamp is switched on it outputs its maximum (with corresponding heat), which, when used in a $30\,s^{-1}$ switching mode as here, shortens the life considerably.

The pHONO instrument sampled from an inlet box (also housing a NO_y converter) located ~ 4 m from ground level on the sampling tower at Weybourne. The sample point was connected to the instrument by a 12 m 1/4 in. PFA line (Swagelok) which was shared by the CAPS NO_2 instrument, thus the flow rate was ~ 3 standard $L\,min^{-1}$, resulting in a residence time of ~ 3 s. The LOPAP instrument, which has its own inlet, sampled from the roof of a specially converted van located 20 m away up-slope. Consequently, both instruments sampled at a similar height and there was clear, unobstructed line of sight between them. The pHONO inlet was only ~ 1 m above the Weybourne observatory roof, which may have contributed to the turbulent dynamics observed in the data especially during daytime. The pHONO instrument was calibrated for NO sensitivity in ambient air twice nightly at 00:00 and 04:00 LT, NO offset was taken between these times by assuming it is equivalent to a stable night-time NO value in remote regions away from any source, where NO should be zero in the presence of ozone (Lee et al., 2009). NO_2 conversion efficiencies were determined in zero air once per week. Limits of detection were 1.5 and 1.9 ppt averaged over 1 min for NO and NO_2, respectively. The LOPAP was operated and calibrated according to the standard procedures described in (Kleffmann and Wiesen, 2008), with a detection limit of 3 pptV and time resolution of 5 min. Zero measurements using high-purity N_2 (N5 grade, BOC) were performed every 12 h on the LOPAP.

Figure 3.6 shows the HONO time series from both the LOPAP and pHONO instruments during the 8 days of concurrent HONO measurements.

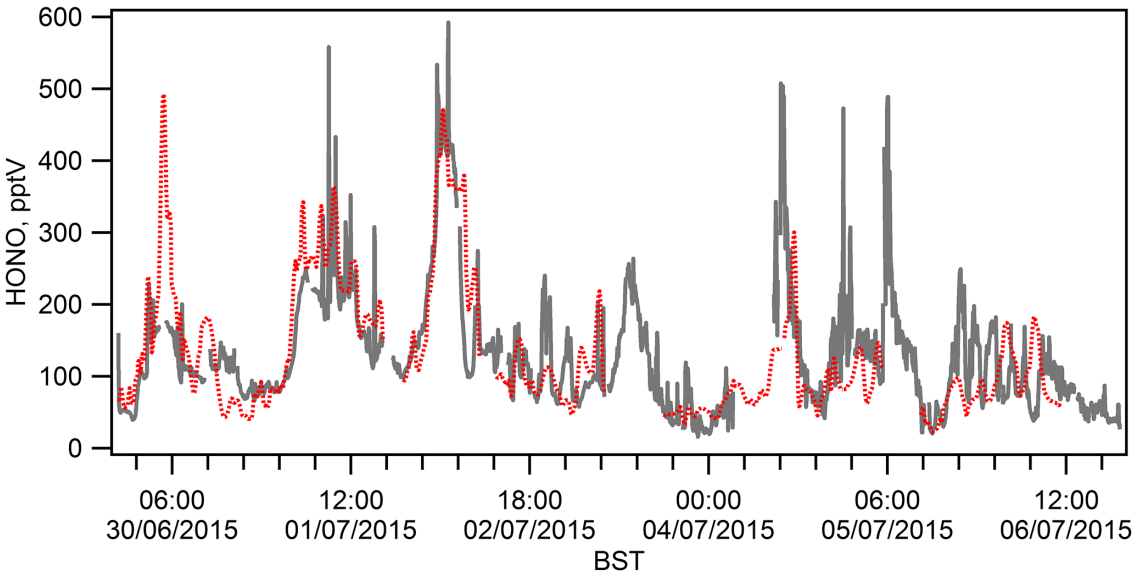

Figure 3.6 – HONO time series during July 2015 at the Weybourne Atmospheric Observatory (WAO) measured by LOPAP (grey) and pHONO (red).

There is reasonable agreement ($R^2 = 0.58$, $y = 0.82x$) between the established LOPAP method of HONO measurement and that provided by the pHONO instrument without correction or calibration (Fig. 3.6). During the high-ozone and high-HONO events observed on the first and second of July especially there is very good agreement ($R^2 = 0.70$, $y = 0.83x$) between the two. Gaps in the data represent times where the pHONO limit of determination was reached – where there are too few points in the averaging window after statistical analysis of the data to be meaningful, e.g. < 2 points in a 5 min averaging window. This is because in real atmospheric conditions the pHONO instrument is hampered by the time resolution at which data are collected, i.e. if there is strong turbulence, meaning the NO_2 or HONO concentration varies rapidly on a time-scale shorter than that at which data are collected, then wide scatter is observed as was the case at Weybourne. Strong boundary layer transport meant that the NO_2 measurement varied by up to 1.5 ppb in a minute, this was most evident during the mornings. The limitation is because of the way the data must be processed by interpolating between measurements and subtraction of the 395 nm signal form the 385 nm signal. Decreasing the time between photolysis switching (from 30 s) would obviously decrease this effect, but, ultimately, separate 385 nm (or lower) and 395 nm analyser channels are required. Consequently the data analysis routine

for the pHONO data includes tests for the variability of the data, discarding points which show $> 5\,\%$ variation from the subsequent point. Data failing this test are discarded and result in gaps, this is the effective limit of determination. The data are then treated with a *robust* locally weighted scatter plot smoothing (LOESS, Cleveland 1979) algorithm to remove extreme values. The gaps in the time series of LOPAP (Fig. 3.5) were due to the removal of zero measurements and false spikes due to bubbles passing the detector.

Figure 3.7 demonstrates the level of agreement in the measured HONO concentration by the LOPAP and pHONO methods between 29 June and 7 July. In Fig. 3.7, the data have been fitted by orthogonal distance regression (Boggs et al., 1987), which allows for errors in both x and y data but which has been shown to possibly overestimate the slope (Carroll and Ruppert, 1996), and by simple linear regression. In either case a strong positive correlation is exhibited, suggesting the replacement UV-LEDs had the desired effect without the application of corrections for the HONO conversion efficiency. The slopes of 0.82 and 1.02 suggest that the new 385 nm lamp was able to convert the majority of HONO. The discrepancy suggests that up to $\sim 18\,\%$ of HONO was converted by the 395 nm lamp. The scatter evident in Fig. 3.7 is attributed to atmospheric dynamic effects resulting in a rapidly changing NO_2 background on time-scales faster than the response of the instrument ($30\,s^{-1}$), leading to a coefficient of determination of 0.58. Non-zero intercepts indicate a small systematic offset may be present in the pHONO instrument, though more likely is an effect of scatter on the regressions. Disagreement between the two methods (e.g. 30 June) is likely due to local contamination from diesel-powered agricultural and construction equipment operating nearby, and by the exhaust of the fluorescence assay by gas expansion (FAGE) instrument (Whalley et al., 2013). The FAGE can discriminate HO_2 and RO_2 by complete reaction of HO_2, with NO necessitating high NO concentrations. The exhaust is vented through a vat of Sofnofil sorbent which removes most NO_x but may also oxidise NO to HONO, which then may be sampled differently by the pHONO instrument and LOPAP due to their relative locations to the FAGE exhaust.

Accuracy and uncertainty in unstable conditions could be improved by measuring at the two different wavelengths concurrently, rather than consecutively. In the same way photolytic NO_2 measurement is improved by measuring concurrently with NO, rather than consecutively. This would require three chemiluminescent analysers in parallel, with two photolytic converters. However, in ambient indoor air quality monitoring, where

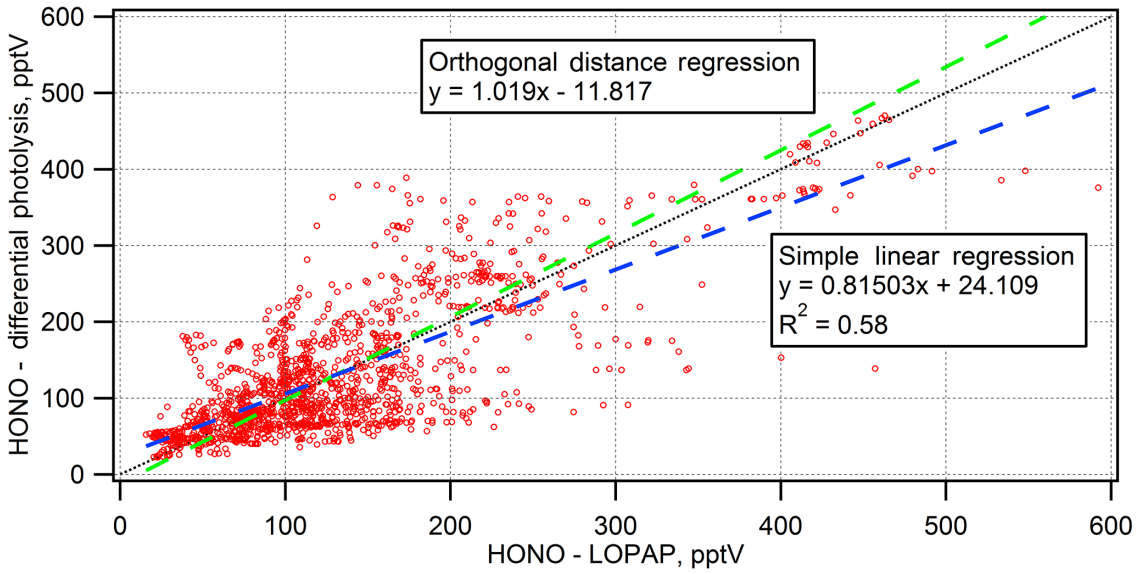

Figure 3.7 – Correlation between HONO measured by LOPAP (x axis) and pHONO (y axis). The simple linear regression is shown in blue, and the orthogonal distance regression in green. The $1:1$ line is shown for reference.

HONO is seen as increasingly important (Gligorovski, 2016), a simple single-channel, dual-wavelength design might be appropriate and useful.

3.5 Conclusions

An instrument for *in-situ* determination of HONO photolytically has been developed, characterized, and deployed in the field as a proof of concept. During an atmospheric simulation chamber comparison, the HONO measured correlated well with FT-IR measurement. During field tests the photolytic HONO instrument agreed reasonably ($R^2 = 0.58$, $y = 0.82x$) well with the established LOPAP instrument, though the limitations of having a two-channel sequential measurement were apparent at times, this would be easily overcome in a three-channel concurrent system. Calibration would gain from a pure HONO source, currently the pHONO calibration requires an independent, direct NO_2 measurement and NO_y measurement.

Chapter 4

Evidence for renoxification in the tropical marine boundary layer

This chapter was presented as an article in the journal Atmospheric Chemistry and Physics.

Reed, C., Evans, M. J., Crilley, L. R., Bloss, W. J., Sherwen, T., Read, K. A., Lee, J. D., and Carpenter, L. J.: Evidence for renoxification in the tropical marine boundary layer, Atmospheric Chemistry and Physics, 17, 4081-4092, doi: 10.5194/acp-17-4081-2017, 2017.

"It doesn't matter how beautiful your theory is, it doesn't matter how smart you are. If it doesn't agree with experiment, it's wrong."

Richard P. Feynman

4.1 Abstract

We present 2 years of NO_x observations from the Cape Verde Atmospheric Observatory located in the tropical Atlantic boundary layer. We find that NO_x mixing ratios peak around solar noon (at 20–30 pptV depending on season), which is counter to box model simulations that show a midday minimum due to OH conversion of NO_2 to HNO_3. Production of NO_x via decomposition of organic nitrogen species and the photolysis of HNO_3 appear insufficient to provide the observed noontime maximum. A rapid photolysis of nitrate aerosol to produce HONO and NO_2, however, is able to simulate the observed diurnal cycle. This would make it the dominant source of NO_x at this remote marine boundary layer site, overturning the previous paradigm according to which the transport of organic nitrogen species, such as PAN, is the dominant source. We show that observed mixing ratios (November–December 2015) of HONO at Cape Verde ($\sim$ 3.5 pptV peak at solar noon) are consistent with this route for NO_x production. Reactions between the nitrate radical and halogen hydroxides which have been postulated in the literature appear to improve the box model simulation of NO_x. This rapid conversion of aerosol phase nitrate to NO_x changes our perspective of the NO_x cycling chemistry in the tropical marine boundary layer, suggesting a more chemically complex environment than previously thought.

4.2 Introduction

The chemical environment in the remote marine boundary layer (MBL) is characterized by very low concentrations of nitrogen oxides ($NO_x = NO + NO_2$) i.e. 10 to < 100 pptV (Carsey et al., 1997; Lee et al., 2009; Monks et al., 1998), high concentrations of water vapour, and the presence of inorganic halogen compounds, resulting in net daytime ozone (O_3) destruction (Dickerson et al., 1999; Read et al., 2008; Sherwen et al., 2016b; Vogt et al., 1999). This MBL loss of ozone plays an important role in determining the global budget of ozone and the overall oxidizing capacity of the region. Understanding the concentrations of NO_x in these environments is thus important for determining the global ozone budget, alongside wider atmospheric chemical impacts.

NO_x in the remote MBL has been attributed to (a) long-range transport and decomposition of species such as peroxy acetyl nitrates (PAN), organic nitrates, or HNO_3 (Moxim et al., 1996), (b) shipping emissions (Beirle et al., 2004), (c) a direct ocean source (Neu et al., 2008), and (d) its direct atmospheric transport (Moxim et al., 1996). However, more recently the possibility of "renoxification" by rapid nitrate photolysis on a variety of surfaces has garnered attention. Photolytic rate enhancements have been reported on aerosol nitrate (Ndour et al., 2009; Ye et al., 2016b), urban grime (Baergen and Donaldson, 2016, 2013), natural and artificial surfaces (Ye et al., 2016a), and in laboratory-prepared organic films and aqueous solutions (Handley et al., 2007; Scharko et al., 2014; Zhou et al., 2003).

The oxidation of NO_2 to HNO_3 by OH is the predominant sink for NO_x in the remote MBL - reaction 4.1. NO_x can also be converted into aerosol phase nitrate via the hydrolysis of N_2O_5 (Reaction 4.2, Evans and Jacob 2005), but this is a slow gas phase process in these low-NO_x environments. NO_x can be returned through HNO_3 photolysis (Reaction 4.3) or reaction with OH (Reaction 4.4), but in general these processes are again slow in the gas phase and so HNO_3 can deposit to the surface, be washed out by rain, or taken up by

aerosol (Reaction 4.5).

$$NO_2 + OH + M \rightarrow HNO_3 + M \tag{4.1}$$

$$N_2O_5 + H_2O_{(aer)} \rightarrow 2\,HNO_{3(aer)} \tag{4.2}$$

$$HNO_3 + h\nu \rightarrow OH + NO_2 \tag{4.3}$$

$$HNO_3 + OH \rightarrow NO_3 + H_2O \tag{4.4}$$

$$HNO_{3(g)} + \text{aerosol} \rightarrow HNO_{3(aer)} \tag{4.5}$$

More recently the production and subsequent hydrolysis of halogen nitrates ($IONO_2$, $BrONO_2$, $ClONO_2$) have been suggested to be a potentially important sink for NO_x in the marine boundary layer

In this paper we investigate the budget of NO_x in the remote MBL using observations of NO_x and HONO collected at the Cape Verde Atmospheric Observatory during 2014 and 2015. We use a 0-D model of NO_x, HO_x, halogen, and VOC (volatile organic compounds) chemistry to interpret these observations and investigate the role that different NO_x source and sink terms play.

4.3 Methodology

The Cape Verde Atmospheric Observatory (CVO), a WMO Global Atmospheric Watch (GAW) station, is located in the tropical North Atlantic (16.864, −24.868) on the island of São Vicente and is exposed to air travelling from the north-east in the trade winds (Carpenter et al., 2010). In general, the air reaching the station has travelled many days over the ocean since exposure to anthropogenic emissions; thus the station is considered representative of the remote marine boundary layer (Read et al., 2008). A large range of compounds are measured at the CVO (Carpenter et al., 2010), but we focus here on the NO and NO_2 continuous measurements, alongside HONO measurements that were made for 10 days in winter 2015.

4.3.1 NO and NO_2 observations

NO and NO_2 are measured by NO chemiluminescence (Drummond et al., 1985) coupled to photolytic NO_2 conversion by selective photolysis at 385–395 nm as described in chap-

ters 2 & 3 as well as by Lee et al. (2009), Pollack et al. (2011), and Ryerson et al. (2000). A single photomultiplier detector switches between 1 min of chemiluminescent zero, 2 min of NO, and 2 min of NO_x measurement.

Air is sampled from a common 40 mm glass manifold (QVF) which draws ambient air from a height of 10 m above ground level. The manifold is downward-facing into the prevailing wind at the inlet and fitted with a hood. The manifold is shielded from sunlight outside and thermostated within the lab to 30° C to prevent condensation. Air is drawn down by centrifugal pump at $\sim$750 litres per minute resulting in a sample flow speed of $10\,\mathrm{m\,s^{-1}}$ and a residence time to the NO_x instrument of 2.3 s. Humidity and aerosol are reduced by two dead-end traps at the lowest points of the manifold inside and outside the lab, which are drained off regularly. Manifold sample flow, humidity, and temperature are recorded and logged continuously.

Air is sampled a 90° to the manifold flow through 1/4 inch PFA tubing at 1 standard litre per minute, being filtered through a 47 mm, 0.22 μm mesh filter before entering the NO_x analyser.

The humidity of the sample gas is further reduced by a Nafion dryer (PD-50T-12-MKR, Permapure), fed by a constant sheath flow of zero air (PAG 003, Eco Physics AG), which is also filtered through a Sofnofil (Molecular Products) and activated carbon (Sigma Aldrich) trap. This reduces sample humidity variability, which affected NO sensitivity through chemiluminescent quenching (Clough and Thrush, 1967), where sample humidity can vary from 60 to 90 % (Carpenter et al., 2010). Calibration for NO sensitivity and NO_2 converter efficiency occurs every 73 h by standard addition to ambient air as described by Lee et al. (2009); in this way correction for humidity affecting sensitivity and O_3 affecting NO_2 conversion efficiency is unnecessary. Sensitivity drift between calibration is < 2 %, within the overall uncertainty of the measurement. Zero air is also used to determine the NO_2 artefact signal which can arise when NO_x-free air is illuminated at UV wavelengths due to the photolysis of HNO_3, etc., adsorbed on the walls of the photolysis cell (Nakamura et al., 2003; Pollack et al., 2011; Ryerson et al., 2000). NO artefact correction is made by assuming that it is equivalent to a stable night-time NO value in remote regions (Lee et al., 2009), away from any emission source, where NO should be zero in the presence of O_3. Chapter 2 showed that thermal interferences in NO_2 using this technique may cause a bias in cold or temperate remote regions but that in warm regions, such as Cape

Verde, the effect is negligible. Photolytic interferences such as $BrONO_2$ and HONO and inlet effects may also alter the retrieved NO or NO_2 (see chapters 2 & 3). These effects are considered to be sufficiently small, as found in chapters 2 & 3, that the concentrations of NO and NO_2 can be determined within an accuracy of 5 and 5.9 % respectively at the (very low) levels present at CVO. The instrument having a zero count rate of ~ 1700 Hz with 1σ standard deviation of that signal (~ 50 Hz), this gives a precision of 7.2 pptV for 1 s data with typical sensitivity over the measurement period of 6.9 cps pptV^{-1}. The resultant limits of detection for NO and NO_2 are 0.30 and 0.35 pptV when averaged over 1 h.

4.3.2 HONO observations

Between 24 November and 3 December 2015, a long-path absorption photometer (LOPAP, Heland et al. 2001) was employed at CVO to provide an *in-situ* measurement of nitrous acid. The LOPAP has its own thermostated inlet system with reactive HONO stripping to minimize losses so does not sample from the main lab manifold. The LOPAP inlet was installed on the roof of a container lab ~ 2.5 m above ground level, unobstructed from the prevailing wind. Calibration and operation of the LOPAP was carried out in line with the standard procedures described by Kleffmann and Wiesen (2008). Specifically at CVO, the sampling conditions were set in order to maximize the sensitivity of the LOPAP, using a gas sampling flow rate of 2 standard litres per minute. A two-point calibration was performed using a standard solution of nitrite (NO_2^-) at concentrations of 0.8 and 10 μg L^{-1}. To account for instrument drift, baseline measurements using an overflow of high-purity N_2 were performed at regular intervals (8 h). The detection limit of the LOPAP (2σ) was calculated by the variability during a typical baseline measurement under N_2 and was found to be 0.2 pptV. The relative error of the LOPAP was conservatively set to 10 % of the measured concentration.

4.3.3 Box model

We use the Dynamically Simple Model of Atmospheric Chemical Complexity (DSMACC) atmospheric chemistry box model (Emmerson and Evans, 2009) is used to interpret the NO_x observations. It use the Kinetic Pre-Processor (KPP-2.1, Damian et al. 2002) to solve

ordinary differential equations generated from the reactions and their kinetic information (Sandu and Sander, 2006). Rate information is assimilated from; Master Chemical Mechanism for near explicit organic reactions (MCMv3.3.1, Bloss et al. 2005; Jenkin et al. 1997, 2003, 2015; Saunders et al. 2003); inorganic rates are taken from IUPAC (Atkinson et al., 2004, 2007) and JPL (Burkholder et al., 2015) evaluated databases and are detailed in tables below; clear sky photolysis rates are calculated by the Tropospheric Ultraviolet and Visible model (TUV, www2.acom.ucar.edu/modeling/tuv-download; Madronich 1993).

We focus on the summer season (June, July, and August) as this has the largest data coverage ($N = 153$) and is out of the dust season, which extends through winter and spring (Carpenter et al., 2010; Fomba et al., 2014; Ridley et al., 2014) and coincides with the lowest NO_y mixing ratios (Carpenter et al., 2010). The model is run for day 199 at 16.864° N, −024.868° W. We initialize the model with the mean observed H_2O, CO, O_3, VOCs (Carpenter et al., 2010; Read et al., 2012), and $100\,\mu m^2\,cm^{-3}$ aerosol surface area (Carpenter et al., 2010). We also initialize the model with 1.5 pptV of I_2 and 2.5 pptV of Br_2 to provide ∼1.5 pptV of IO and ∼2.5 pptV BrO during the day, consistent with the levels measured over 9 months at the CVO during 2007 (Mahajan et al., 2010b; Read et al., 2008). We use the average diurnal cycle of the measured HONO concentrations, described above. Terms for entrainment of free tropospheric O_3 and PAN allow for their mixing down over a time-scale of 1 day to balance their loss. Solar radiation at this location in the tropics shows little seasonal variation, hence photolysis rates are similar in summer and autumn. This measurement period was also free of dust influence. We assume clear-sky conditions for photolysis. The meteorological parameters pressure, temperature, relative humidity, and boundary layer height are set to median values reported by Carpenter et al. (2010). Boundary layer height is fixed at 713 m as no overall seasonal or diel pattern is evident in the boundary layer height at Cape Verde (Carpenter et al., 2010). This is expected at a site representative of the marine boundary layer, which has almost no island effects (except for very rare instances of wind outside the north-westerly sector, which are excluded). Thus, we discount any influence from boundary layer height changes on the diurnal cycles presented.

The unconstrained model is run forwards in time until a stable diurnal cycle is attained, i.e. ∼3 days. The base case chemistry has only gas phase sources plus gas phase and deposition sinks for NO_x as described in appendix A where a full description of the model

chemistry is provided.

4.4 Results and discussion

4.4.1 Diurnal cycles in NO_x and HONO

Figure 4.1 shows the measured mean diurnal cycles of NO, NO_2, NO_x, and O_3 observed in each season (meteorological spring, summer, autumn, and winter) during 2014 and 2015. Every season shows a strong diurnal cycle in NO, peaking after solar noon at around $\sim$13:00 to 14:00. The diurnal cycle of NO_2 is much less pronounced but also exhibits weak maxima in the early afternoon. Overall this leads to a maximum in NO_x during the day. This behaviour is consistent throughout the year and air mass, though not necessarily on a "day-to-day" basis.

The observed diurnal cycle in NO_x is hard to explain with conventional chemistry. The increase in night-time NO_x suggests a continuous source, but the maximum around noon suggests a photolytic source. Given that the predominant NO_x sink is reaction with OH to form HNO_3, it would be expected that there would be a minimum in NO_x during the day rather than a maximum. Similar observations have been reported previously (Monks et al., 1998) at the Cape Grim Baseline Air Pollution station ($-40.683°$ S, $144.670°$ W), a comparably remote site in the Southern Hemisphere, and during the Atlantic Stratocumulus Transition Experiment (ASTEX) cruise ($\sim 29°$ N, $24°$ W), which reported similar daytime NO_x production (Carsey et al., 1997). The observed behaviour in the CVO NO_x was historically attributed to atmospheric thermal decomposition of NO_y species (Lee et al., 2009).

Figure 4.2 shows the average diurnal cycle at CVO of measured HONO concentrations. The data exhibit a strong daytime maximum peaking at noon local time (solar noon $\sim$13:20) and reaching near zero at night, indicating a photolytic source. HONO is lost through deposition, photolysis, and reaction with OH, whilst night-time build-up is often observed (Ren et al., 2010; VandenBoer et al., 2014; Zhou et al., 2002); here, HONO appears to reach a steady-state concentration of ~ 0.65 pptV throughout the night. This pseudo steady-state behaviour of nocturnal HONO has previously been reported in the polluted marine boundary layer by Wojtal et al. (2011), albeit with much higher HONO

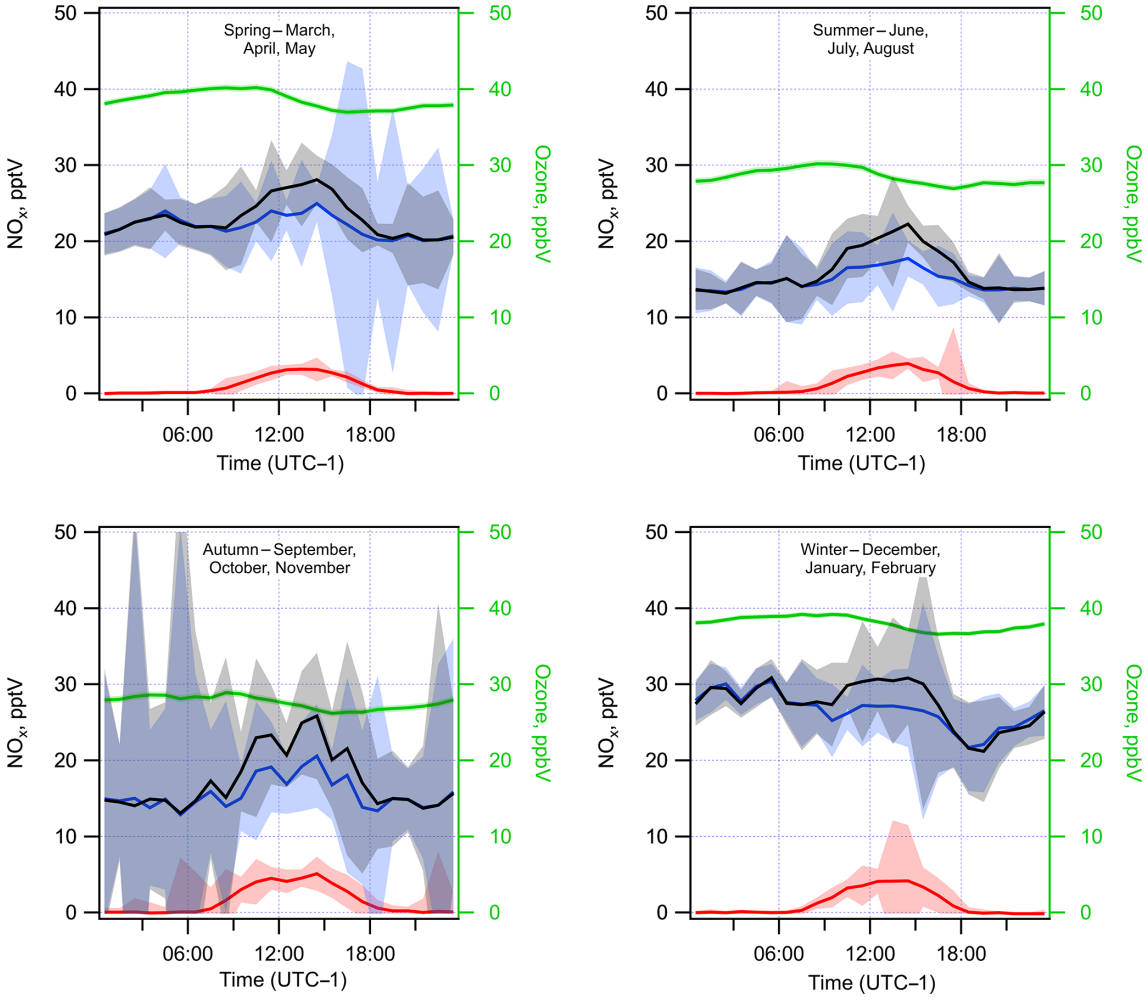

Figure 4.1 – The observed seasonal diurnal cycles in NO, NO_2, NO_x, and O_3 at the CVO GAW station during 2014 and 2015. NO is shown in red, NO_2 in blue, NO_x in black, and O_3 in green. Shaded areas indicate the standard error of data.

mixing ratios.

Daytime production of HONO is similarly hard to reconcile if its formation is by the homogeneous $OH + NO$ reaction (or other gas phase HO_x-NO_x chemistry, e.g. Li et al. 2014). With NO mixing ratios below 5 pptV, OH measured peaking at ~ 0.25 pptV during the RHaMBLe campaign (Carpenter et al., 2010; Whalley et al., 2010), and a maximum noontime jHONO of $1.2 \times 10^{-3}\,s^{-1}$, a steady-state HONO mixing ratio of ~ 0.04 pptV is found ($k_{(OH+NO)} = 7.4 \times 10^{-12}\,mol\,cm^{-3}\,s^{-1}$). An additional daytime source of HONO must be present to explain the observed concentrations.

Both the long-term NO_x and the short-term HONO observations made at CVO are cannot be explained with purely gas phase chemistry. Both datasets show daytime maxima

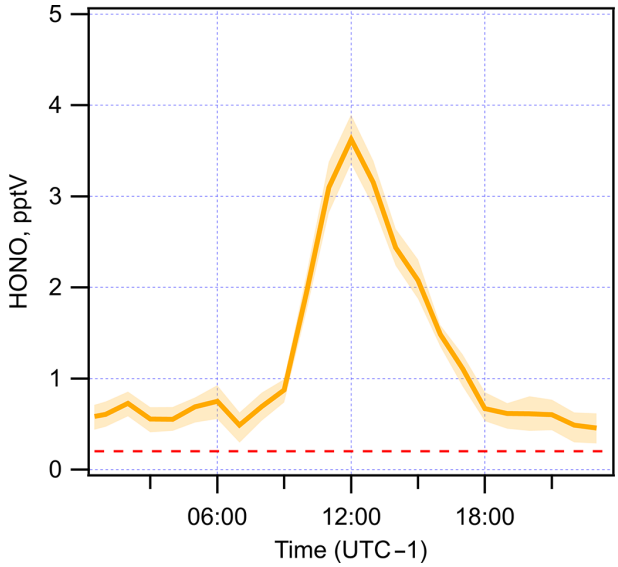

Figure 4.2 – The observed average HONO diurnal measured at CVO during 24 November–3 December 2015. Shaded area indicates standard deviation of data. Dashed red line shows the HONO limit of detection.

indicative of a photolytic source of NO_x and HONO, whereas gas phase chemistry would predict minima in NO_x during daytime and 2 orders of magnitude less HONO.

4.4.2 Box modelling of NO_x sources

Using the box model (Sect. 4.3.3), we explore the observed diurnal variation in NO_x and understand the role of different processes. Classically, the predominant source of NO_x in remote regions is considered to be the thermal decomposition of compounds such as peroxyacetyl nitrate (PAN), which can be produced in regions of high NO_x and transported long distances (Fischer et al., 2014; Jacobi et al., 1999; Moxim et al., 1996). We consider a source of PAN which descends from the free troposphere and then thermally decomposes to NO_2 in the warm MBL. The main sink of NO_x is conversion to HNO_3, which is slightly counterbalanced by a slow conversion of HNO_3 back into NO_x through gas phase photolysis or reaction with OH. Figure 4.3 shows the model with a source of PAN, which results in mixing ratios of 5–8 pptV, consistent with the few measurements made in the marine boundary layer, most notably by Jacobi et al. (1999), who measured levels from < 5 to 22 pptV in the tropical Atlantic, and Lewis et al. (2007), who reported PAN mixing ratios of ~ 10 pptV in the remote mid-Atlantic MBL.

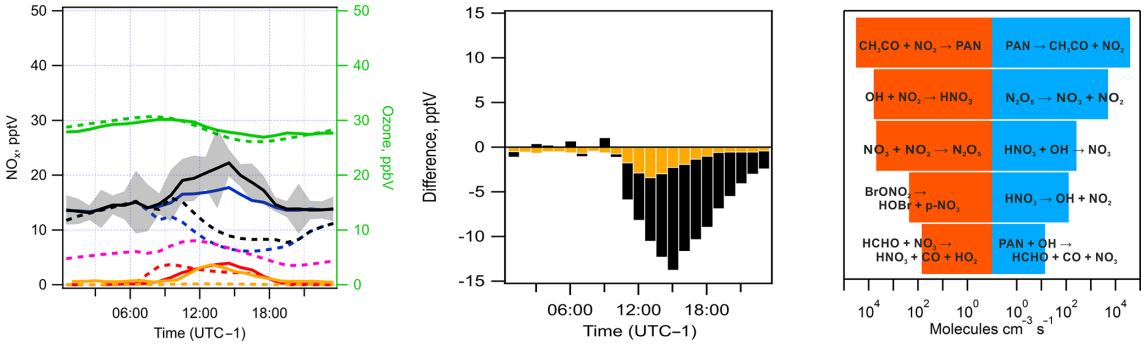

Figure 4.3 – Left shows the measured (solid lines) and modelled (dashed) NO_x and HONO diurnal behaviour at the CVO GAW station where the dominant source of NO_x is a source of PAN descending from the upper troposphere having been transported from polluted regions. Shaded areas are standard error of the observations (NO_x $N = 153$, HONO $N = 10$). O_3 – green; NO_x – black; NO_2 – blue; NO – red; HONO – yellow; PAN – pink. Centre is the difference between measured and modelled NO_x (black) and HONO (yellow). Right shows the rates of production and loss of NO and NO_2 from sources listed in descending order of contribution over a 24 h period accounting for $> 95\,\%$ of the total.

It is evident from the base case model results shown in Fig. 4.3 that the model fails to calculate the NO_x and HONO diurnal cycles. Modelled NO_x concentrations do increase during the night, consistent with the observations, but the model's minimum for NO_x occurs during the day when the observations show a maximum. The modelled and measured HONO is also shown in Fig. 4.3, both peaking during midday with observations reaching 3.5 pptV whilst the model simulates only ~ 0.2 pptV, underestimating HONO at all times. It is clear that long-range transport and thermal decomposition of NO_y species such as PAN alone cannot explain the NO_x diurnal at Cape Verde. A PAN-type continuous thermal decomposition forming NO_x would be inconsistent with the diurnal maximum in NO_x which is observed. The NO_x source necessary to support a noontime maximum would have to show a strong daytime maximum to counter the strong diurnal in the sink.

This need for a diurnal cycle in the NO_x source also suggests that the shipping source of NO_x is unlikely to explain the diurnal cycle. The dominant source of ship NO_x in the region is represented by the large container ships which pass the region on their way to South America or the Cape of Good Hope. It is unlikely that these emissions are systematically higher during the day than during the night, and thus they are unlikely to explain the observed diurnal signal.

There have been a number of studies which have identified much faster photolysis of nitrate within and on aerosol than for gas phase nitric acid. These include studies using real-world natural and artificial surfaces (Baergen and Donaldson, 2013; Ye et al., 2016a,b), laboratory substrates such as organic films and aqueous acid solutions (Handley et al., 2007; Scharko et al., 2014; Zhou et al., 2003), aerosol nitrate (Ndour et al., 2009; Ye et al., 2016b), and a model estimate (Cohan et al., 2008). These studies have found that particulate nitrate photolysis rates can be up to ~ 3 orders of magnitude greater than gas phase HNO_3 photolysis in marine boundary layer conditions (Ye et al., 2016b). There is also broad agreement between different studies on the main photolysis product being nitrous acid (HONO), with NO_2 as a secondary species. The product ratio appears dependent on aerosol pH, with HONO production only occurring at low pH (Scharko et al., 2014). This is shown in Reaction 4.6 as particulate nitrate (p-NO_3) photolysing to HONO and NO_2 in a ratio $x : y$.

$$p\text{-}NO_3 + h\nu \rightarrow x\text{HONO} + y\text{NO}_2 \tag{4.6}$$

There is also evidence that the photolysis rate is positively correlated with relative humidity (Baergen and Donaldson, 2013; Scharko et al., 2014). As such, particulate nitrate photolysis rates appear to increase with increasing aerosol acidity and relative humidity. With the CVO site experiencing relative humidity of 79 % on average (Carpenter et al., 2010) and aerosol containing a significant acidic fraction (Fomba et al., 2014), particulate nitrate photolysis could have a role to play in the NO_x budget at Cape Verde.

In order to explore the implications for Cape Verde NO_x chemistry, we re-ran the base model removing the PAN source but including particulate nitrate (p-NO_3) photolysis (Reaction 4.6) leading to HONO and NO_2 production, scaled to the gas phase photolysis of HNO_3. This parameterization nominally represents photolysis of nitrate within and on aerosol; however, conceptually it includes any additional surface production of HONO and NO_2. We use an aerosol phase concentration of nitrate of $1.1\,\mu g\,m^{-3}$ (equivalent to 400 pptV), which is the mean concentration found in PM_{10} aerosol at Cape Verde, with little apparent seasonal variability (Fomba et al., 2014; Savarino et al., 2013). The branching ratio of HONO to NO_2 production from Reaction 4.6 (x and y) was set to $2 : 1$ in line with the findings of Ye et al. (2016b). We scale the p-NO_3 photolysis rate to gas phase HNO_3 photolysis by factors of 1, 10, 25, 50, 100, and 1000. The study of Ye et al. (2016b) describes enhancements of up to ~ 300 fold. The impact on the summer months

is shown in Fig. 4.4.

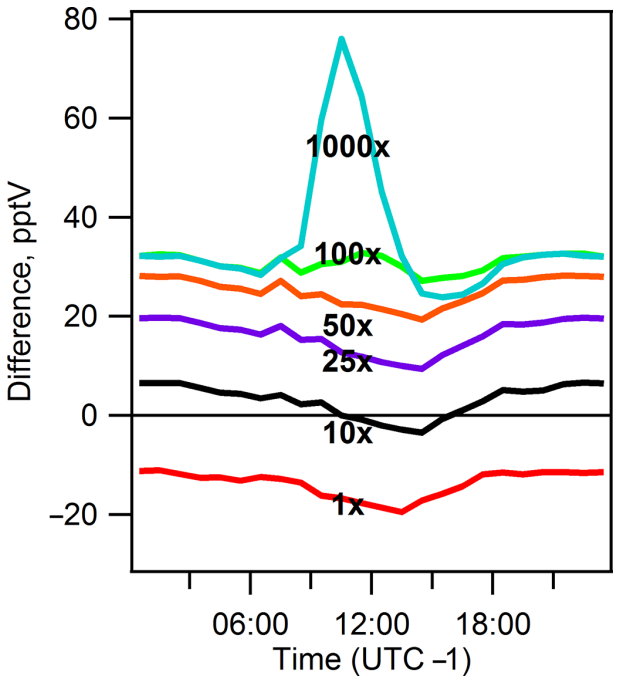

Figure 4.4 – The difference between measured and modelled of NO_x at CVO during summer months when photolysis of nitrate is considered. The rate of particulate nitrate photolysis has been scaled to the rate of HNO_3 photolysis by factors of 1, 10, 25, 50, 100, and 1000.

Including the photolysis of aerosol nitrate changes both the mean concentration and diurnal cycle of NO_x significantly. The diurnal NO_x is now flat or peaks during the daytime, more consistent with observations. We find that the best approximation is achieved when the rate of particulate nitrate photolysis is $\sim$10 times that of HNO_3, which is broadly consistent with laboratory-based observations (Zhou et al., 2003). A wide variability of p-NO_3 photolysis rates on different surfaces is reported (Ye et al., 2016b); thus the photolysis of nitrate is uncertain and likely to be variable with aerosol composition. In all particulate nitrate photolysis-only scenarios, depicted in Figs. 4.4 it is evident that p-NO_3 photolysis alone does not give the observed increase in night-time NO_x observations. Conversely the PAN-only scenario shown in Fig. 4.3 is insufficient to sustain daytime NO_x. It is therefore likely that the actual source of NO_x is a combination of PAN entrainment from the free troposphere and particulate nitrate photolysis.

Combining the free-tropospheric source of PAN and the photolysis of particulate nitrate at a rate of 10 times the gas phase, HNO_3 photolysis (Fig. 4.5) results in a model simulation with roughly twice as much NO_x both at night and during daylight but a roughly flat

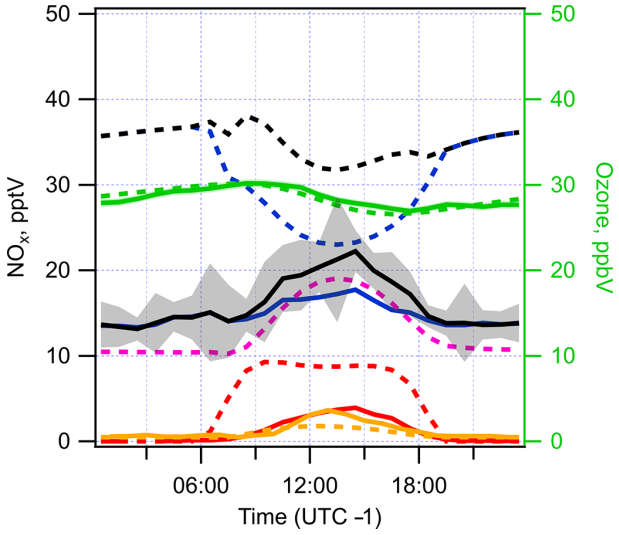

Figure 4.5 – The modelled diurnal profile of NO_x at CVO during summer months when photolysis of nitrate (set at 10× the gas phase HNO_3 photolysis) and a tropospheric PAN source are considered. Shaded areas for NO_x are the standard error of the observation. O_3 – green; NO_x – black; NO_2 – blue; NO – red; HONO – yellow; PAN – pink.

diurnal profile. Simulated HONO peaks at local noon, similar to the observations, though the simulation underestimates the midday peak. Nocturnal HONO mixing ratios agree with observations being non-zero at ~ 0.5 pptV.

Introduction of an additional source of NO_x is able to roughly produce a flat diurnal cycle, though it is not able to simulate a definite peak of NO_x during daytime. With the addition of a source and no change in sinks for NO_x this is unsurprising and leads to relative overestimation of NO_x particularly at night. It is therefore likely that one or more NO_x sinks are absent from the base simulation, which must be explored further.

4.4.3 NO_x sinks

Aside from loss to HNO_3 directly through reaction with OH (Reaction 4.1), NO_x is also lost to nitrate by reaction with halogen oxides (XO) forming halogen nitrates (Reaction 4.7, Keene et al. 2009). Read et al. (2008) showed how halogen oxides mediate ozone formation and loss at Cape Verde, thus also exerting an indirect effect on NO_x.

$$XO + NO_2 + M \rightarrow XONO_2 + M \tag{4.7}$$

Figure 4.6 shows the rates of production and loss analysis for NO_x in this simulation with both PAN thermal decomposition and particulate nitrate photolysis. The largest net source of NO_x after net sinks (such as halogen nitrate cycling) are removed is nitrate photolysis to HONO and NO_2. The major net sink of NO_x is the formation of nitric acid by reaction of NO_2 with OH. However, uptake of HNO_3 onto aerosol and subsequent rapid (compared to gas phase HNO_3) photolysis act to balance this.

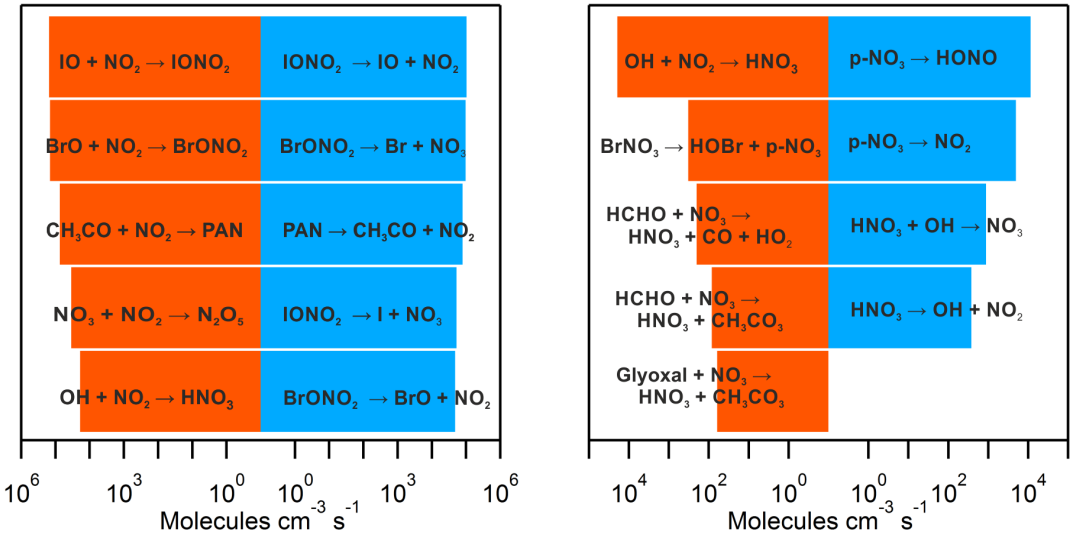

Figure 4.6 – Left is the total production and loss analysis for NO_x of the combined model of particulate nitrate photolysis and PAN decomposition over 24 h. Right is the same analysis discarding the major balanced sinks of fast cycling short-lived species.

The pronounced drop in modelled NO_2 at sunrise is due to the production of halogen nitrates (Reaction 4.7) when HOX rapidly photolyses to produce XO, which can then react with NO_2 to produce $XONO_2$. XO is formed quickly and spikes in concentration, leading to the rapid loss of NO_2. This feature is not observed in the NO_x observations during any season.

The diagnostics in Fig. 4.6 show the role of the different sinks of NO_x. In that simulation these are dominated by the gas phase reaction between NO_2 and OH, but with the rapid formation and subsequent hydrolysis of $BrONO_2$ and $IONO_2$ (Reaction 4.8) playing a major role (Sander et al., 1999). The uptake coefficient (γ) of halogen nitrates onto aerosol therefore could have a strong influence on the NO_x diurnal.

$$XONO_2 + H_2O_{(aer)} \rightarrow HNO_{3(aer)} + X^+ + OH^- \tag{4.8}$$

We perform a sensitivity analysis on the effect of the uptake coefficients on the NO_x and XO diurnals. We do this in a particulate nitrate photolysis-only simulation, without PAN, to isolate the effect of $XONO_2$ hydrolysis on nitrate NO_x cycling. Figure 4.7 shows the effect of changing γ of $XONO_2$ (X = Br, I) within recommended ranges (Burkholder et al., 2015; Saiz-Lopez et al., 2008) on Saharan dust and sea salt – the predominant coarse-mode aerosol by mass at Cape Verde (Carpenter et al., 2010; Fomba et al., 2014), ranging from 0.02 to 0.8.

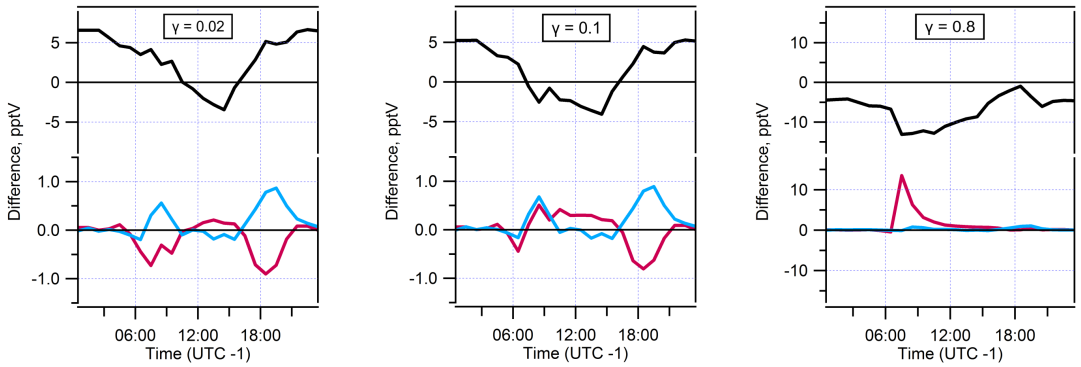

Figure 4.7 – Sensitivity analysis of the effect of changing reactive uptake coefficients (γ) of halogen nitrates , $XONO_2$ (X = Br, I), on NO_x (top), and XO (bottom) diurnal behaviour during summer months at CVO. The difference between measured and modelled values is plotted. Particulate nitrate photolysis is set at 10 times the rate of gaseous HNO_3. NO_x – black; IO – turquoise; BrO – purple

Increasing the γ of $XONO_2$ from 0.02 (the low end of recommended values) to 0.1 results in small changes to both the NO_x and XO diurnals. The loss of NO_x at sunrise becomes more pronounced, whereas the XO diurnals become slightly more 'square' or 'top-hat' as per the observations of Read et al. (2008). Increasing the γ to the upper extreme (γ = 0.8) results in a spike in BrO at sunrise, which consumes the majority of NO_2 though the formation of $BrONO_2$. No combination of uptake coefficients can completely reproduce the characteristic XO diurnals due to poor constraints on heterogeneous halogen chemistry (Abbatt et al., 2012) in addition to gaps in the understanding of gas phase halogen chemistry (Simpson et al., 2015).

The effect on the NO_x diurnal of changing γ is clear in that greater uptake coefficients recommended by Burkholder et al. (2015) result in objectively worse simulation of both the NO_x and XO diurnals. It is therefore likely that information is lacking from the XO–NO_x chemistry scheme as it is currently known.

4.4.4 HOI/HOBr-NO_x chemistry

Recently, IO recycling by reaction with NO_3 has been proposed by Saiz-Lopez et al. (2016), who calculated that the Reaction 4.9 of $HOI + NO_3$ producing IO and HNO_3 has a low enough activation energy and fast enough rate constant to be atmospherically relevant in the troposphere.

$$HOI + NO_3 \rightarrow IO + HNO_3 : k = 2.7 \times 10^{-12}(300/T)^{2.66} \tag{4.9}$$

This mechanism provides a route to nitric acid and thus particulate nitrate at night, whilst also leading to nocturnal IO production leading to loss of NO_2 by $IONO_2$ formation.

Including this new reaction and re-running the model leads to a diurnal profile of IO much more representative of the observations. This however introduces a more pronounced loss of NO_x at sunrise and sunset and also results in NO_x peaking during the day, which fits better with the observations as shown in Fig. 4.8. HONO is still underestimated during daytime though nocturnal values agree well.

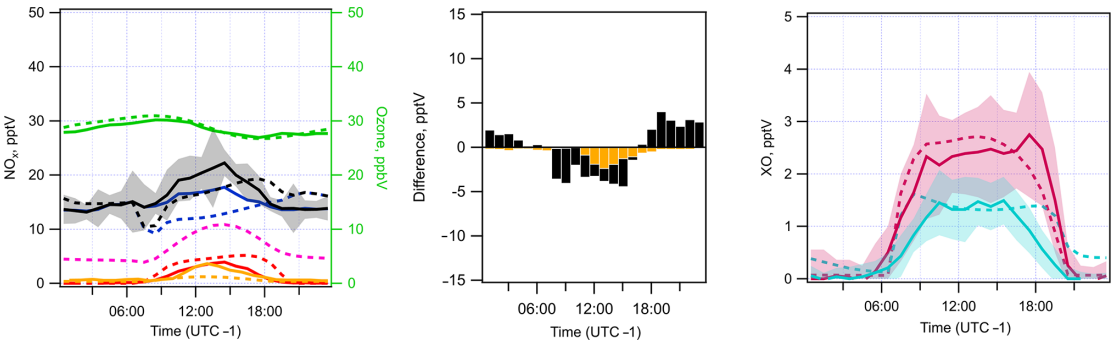

Figure 4.8 – Left is the modelled NO_x and HONO diurnal cycle for the CVO site during summer months with the inclusion of night-time HOI chemistry. Centre shows the difference between measured and modelled values of NO_x (black) and HONO (yellow). Right is the observed (adapted from Read et al. 2008) and modelled IO and BrO. Observations are solid lines, whilst modelled values are shown dashed. Shaded areas are standard error of the observation. O_3 – green; NO_x – black; NO_2 – blue; NO – red; HONO – yellow; PAN – pink; IO – turquoise; BrO – purple.

The inclusion of this HOI + NO_3 reaction reproduces the general NO_x and O_3 diurnals more closely than without; i.e. the model produces a daytime maximum in NO_x. There are also effects on the halogen oxide behaviour. The simulated BrO has a flatter profile, which more closely matches the observations. However, modelled IO is now non-zero at night and the sunrise build-up and sunset decay still occurs more abruptly than the

observations.

Although the NO_x and O_3 diurnals are reproduced more closely with this new chemistry, there is still disagreement with the observed NO_x diurnal at sunrise and sunset especially indicating a missing reaction or reactions. To best approximate the observed diurnal behaviour an analogous HOBr + NO_3 night-time Reaction 4.10 was introduced with a rate 10 times that of $HOI + NO_3$ as calculated by Saiz-Lopez et al. (2016).

$$HOBr + NO_3 \rightarrow BrO + HNO_3 : k = 2.7 \times 10^{-11}(300/T)^{2.66} \tag{4.10}$$

This results in an improved reproduction of the observed NO_x diurnal, Fig. 4.9. This is a purely speculative representation in order to reproduce the observed NO_x diurnal and highlights how some mechanistic knowledge of NO_x–halogen–aerosol systems is still missing.

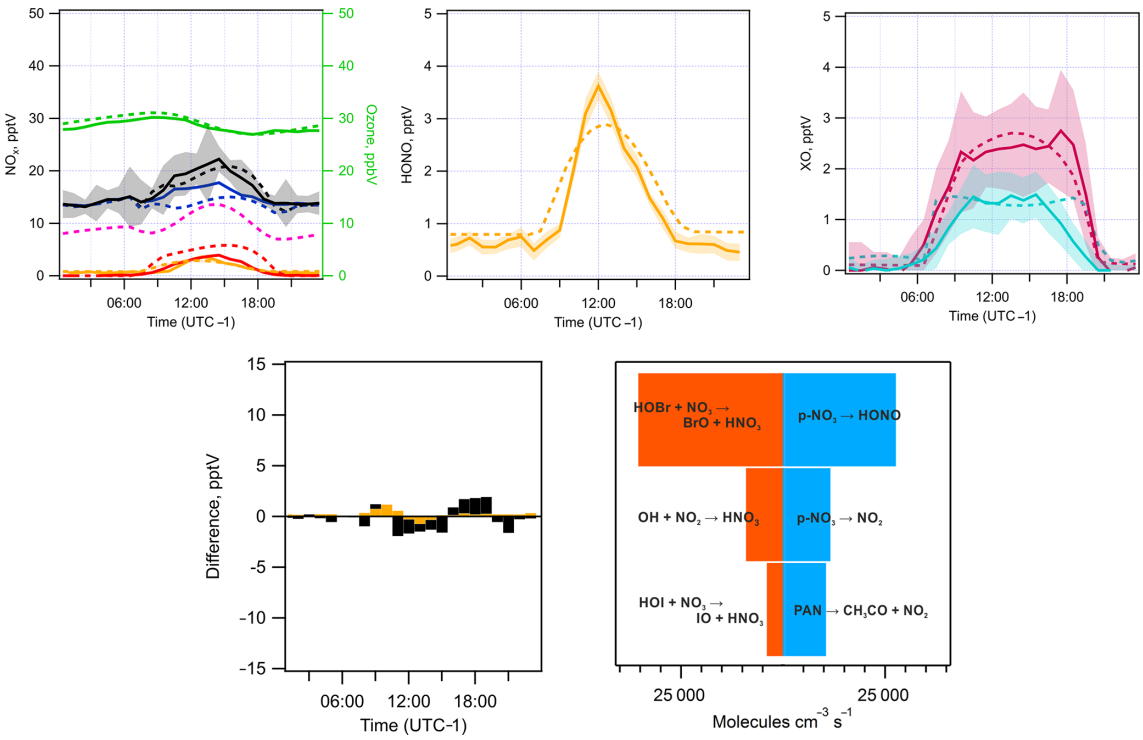

Figure 4.9 – NO_x, O_3, HONO at CVO during summer months compared to model values when HOI and $HOBr + NO_3$ is included in the simulation. Top left: NO_x, O_3, HONO, and PAN diurnal cycles. Top middle: expanded view of modelled and measured HONO. Top right: observed (adapted from Read et al. 2008) and modelled IO and BrO. Bottom left: difference between modelled and measured NO_x and HONO. Bottom right: the net production and loss analysis for NO_x in this simulation. O_3 – green; NO_x – black; NO_2 – blue; NO – red; HONO – yellow; PAN – pink; IO – turquoise; BrO – purple. Measured values are solid lines, modelled values are dashed.

With HOX + NO_3 chemistry included in the model as in Fig. 4.9, significant loss of NO_x at sunrise and sunset is eliminated and agreement is improved over any previous simulation. Greater HONO production is also simulated, with up to ~ 3.0 pptV predicted – in line with the observations shown in Fig. 4.2. This is due to reaction rate of HOBr + NO_3 now being similar to that of OH + NO_3 ($k = 2.00 \times 10^{-11}$) thus the OH + NO reaction forming HONO becomes more important. Halogen oxide modelled diurnal cycles remain broadly consistent with observations. Diagnosis of the net production and loss terms for NO_x reveal that nitrate photolysis to HONO or NO_2 contribute $\sim 80\,\%$ of all NO_x, with decomposition of PAN contributing the remainder. Major net sinks of NO_x are shown to be the reaction with halogen hydroxides and OH to form HNO_3. Nitric acid is then taken up on surfaces and recycled to NO_x through photolysis to NO_2 and HONO.

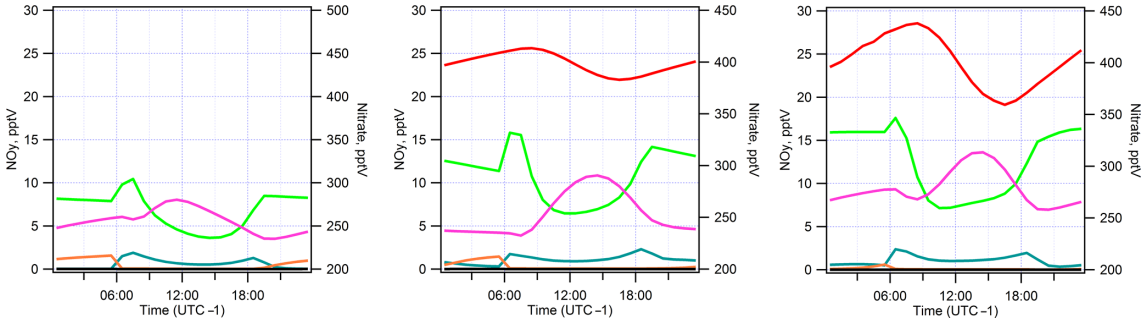

Figure 4.10 – Shown are NO_y diurnals for the CVO site during summer months in the base scenario (left), with HOI + NO_3 chemistry included (centre), and with HOI and HOBr + NO_3 chemistry included (right). $BrONO_2$ – green; $IONO_2$ – teal; PAN – pink; NO_3 – orange; N_2O_5 – black; p-NO_3 – red.

The improvement can be better understood by diagnosing the modelled NO_y distribution. In Fig. 4.10 the distribution of PAN, $IONO_2$, $BrONO_2$, N_2O_5, NO_3, and particulate nitrate (p-NO_3) is shown for the base case scenario (where entrained PAN is the sole source of NO_x in the MBL), for the particulate nitrate photolysis case including HOI + NO_3 chemistry, and for the same case additionally including HOBr + NO_3 chemistry. The major feature changing through the different simulations is the magnitude and shape of the $BrONO_2$ diurnal. From the base run to the inclusion of HOI + NO_3 chemistry and particulate nitrate photolysis, a major increase in $BrONO_2$ mixing ratio is expected at sunrise and sunset. It is this rapid production of $BrONO_2$ which consumes NO_x, resulting in the sharp dips at these times not seen in the observations. In the HOBr and HOI + NO_3 and particulate nitrate photolysis case these features are eliminated and halogen nitrates do

not spike at sunrise or sunset. Nitrate is shown to be conserved by hydrolysis of halogen nitrates on surfaces and uptake of nitric acid. This cycling leads to an NO_x diurnal profile which is more representative of the observations.

In models which included nitrate photolysis a strong diurnal cycle in particulate nitrate presents itself which is depleted during the day and recycles at night, being conserved overall. The daily average concentration remains constant in-line with the integrating filter sample study of Fomba et al. (2014).

Unsurprisingly, the inclusion of $HOX + NO_3$ chemistry results in lower mixing ratios of NO_3 at night. In all cases N_2O_5 (in black) is effectively zero at all times due to very low NO_x mixing ratios in this pristine environment and the relatively high ambient temperatures (24.5 °C) where the N_2O_5 lifetime is $\sim$3 s. This precludes N_2O_5 channels to NO_x (and ultimately nitrate), consistent with the experimental findings of Savarino et al. (2013) at Cape Verde, who found isotope ratios which were incompatible with high production rates of HNO_3 from N_2O_5 hydrolysis and concluded that N_2O_5 and nitryl compound ($ClNO_2$, $BrNO_2$) levels in this region are very low. This is consistent with our own and other studies modelling the pristine marine boundary layer at Cape Verde of Sommariva and Von Glasow (2012). This is in contrast with more polluted regions where N_2O_5 has been shown to be a route to NO_x and $ClNO_2$ (Kim et al., 2014a).

The agreement in modelled and observed NO_x improves, and the modelled values fall within the error of the observations. Additionally the approximate BrO diurnal is achieved without the characteristic "horns"; however, replicating IO observations is still problematic.

A dramatically changing NO_x diurnal could be expected to have an effect on OH and HO_2 mixing ratios. The difference between the base model case, where PAN decomposition is the dominant daytime source, and the final model, where the NO_x is more accurately described by particulate nitrate photolysis and $HOX + NO_3$ chemistry, is shown in Fig. 4.11.

In the case of OH the change from the base model to the final model is an increase of 3.3 % at the maximum; for HO_2 the increase is a more significant 8.6 % (or 1.7 pptV). However, this is well within the uncertainty of measured values Whalley et al. (2010). Figure 4.11 shows that even with dramatic changes in the NO_x simulation, the OH and HO_2 changes very little comparatively despite increased daytime HONO production.

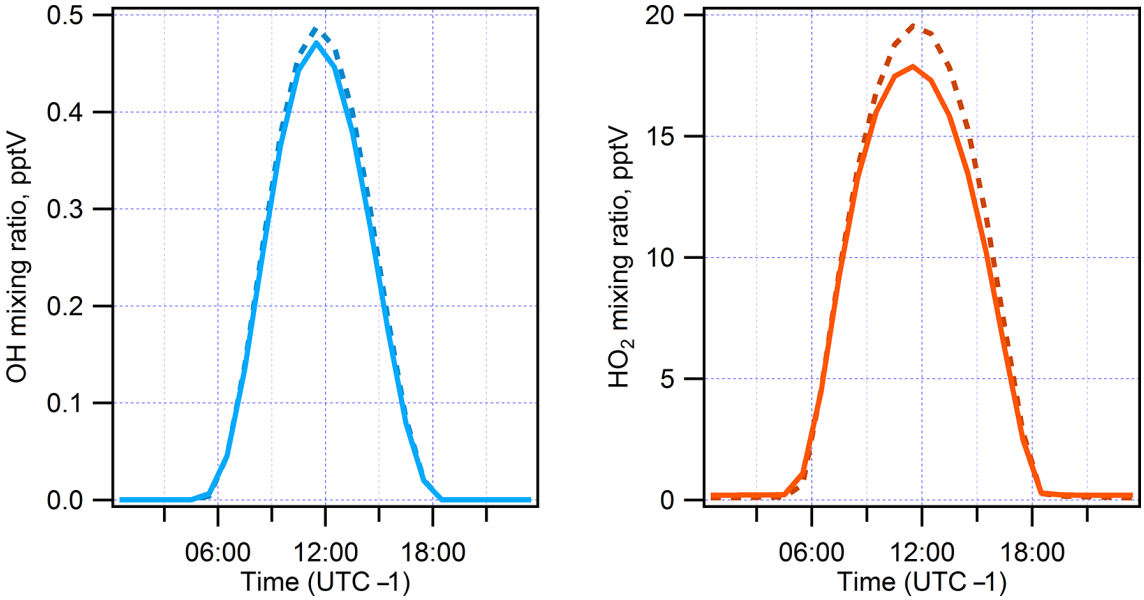

Figure 4.11 – Modelled OH (left) and HO_2 (right) mixing ratios comparing the base case model where PAN decomposition is the dominant source of NO_x in the remote MBL (solid lines) with the final model where the dominant source of NO_x is particulate nitrate photolysis and $HOX + NO_3$ chemistry is included (dashed lines).

From these simulations it would appear that the photolysis of surface-adsorbed nitrate may be the dominant source of NO_x in the marine boundary layer around Cape Verde. Photolysis of aerosol nitrate or nitrate in solution would be capable of producing a diurnal cycle in NO_x, which was consistent with the observations when $HOX + NO_3$ chemistry is considered also. Whilst agreement between model and observation is improved, there is a clear gap in understanding the halogen–NO_x–aerosol system in the remote marine boundary layer.

4.5 Conclusions

Fast aerosol nitrate photolysis is shown to be likely the primary source of NO_x in the remote tropical Atlantic boundary layer. A 0-D model replicated the observed halogen, O_3, OH, NO_x, and HONO levels when including particulate nitrate photolysis at a rate of ~ 10 times that of gas phase nitric acid, consistent with previous laboratory measurements. Model optimization shows that this new source of daytime NO_2 is compatible with observations and currently known chemistry at night and at midday but that at sunrise and sunset there is disagreement due to the treatment of halogen oxides at these times. Recently

suggested halogen hydroxide + nitrate radical chemistry may provide better agreement between model and observation if theoretical reactions can be substantiated.

Chapter 5

Concluding remarks

This thesis aimed to better understand the NO_x budget in the remote marine boundary layer by interpretation of observations from the Cape Verde observatory. To interpret the observations effectively it was first necessary to fully understand the measurement technique, and determine what further observations would be needed in order to achieve that.

In studying the NO_2 photolysis–NO chemiluminescence technique interferences were found that could lead to compromised data, and ultimately misinterpretation. Whilst catalytic converters based on molybdenum have long been shown to convert higher NO_x species (Dunlea et al., 2007; Grosjean and Harrison, 1985; Winer et al., 1974) it was assumed that photolyitc converion would not suffer the same problems. It was shown how measurements of NO_2 made using NO_2 photolysis–NO chemiluminescence may suffer biased towards over-reporting NO_2 in low-NO_x environments. The design of the NO_2 converter was found to promote thermal decomposition of NO_y species to NO_2 resulting in spuriously high NO_2 being reported. Measurements made in remote (i.e. low-NO_x) environments, and where the ambient temperature is lower than that of the NO_2 converter (at high altitude and latitude) were modelled to be especially affected.

The over-reporting of NO_2 results in seemingly high $NO_2 : NO$ ratios and deviations from the photo-stationary steady state which could be interpreted as evidence for a missing oxidant or "compound X". However, without supporting evidence from other measurements of oxidants this missing oxidant must necessarily selectively oxidise NO to NO_2.

This entirely logical but erroneous outcome depends on the supposition that photolytic NO_2 measurements are direct and absolute, however we find that this is not the case.

It has been demonstrated through characterisation of a widespread implementation of photolytic NO_2 measurement that it indeed suffers interference from thermally decomposing NO_y species. Furthermore, it has been demonstrated that the interference can manifest itself as high $NO_2 : NO$ ratios in remote and cold regions which may explain observations made in these regions which exhibit a degree of perculiarity e.g. Hosaynali Beygi et al. 2011; Bauguitte et al. 2012; Frey et al. 2013, 2015; Griffin et al. 2007; Kanaya et al. 2007b; Yang et al. 2004. Measurements made in warm regions where thermally labile NO_y mixing ratios are generally much lower are less affected by interference thus were used in the study of the tropical maine boundary layer here.

Future interpretation of NO_2 measurements made using photolytic instruments can be made incorporating the limitations of the technique, and future measurement systems can be tailored to the environment in which they will be operated with the information provided in chapter 2.

It was found through study of the NO_2 photolysis–NO chemiluminescence technique that an unwanted interference could be exploited in order to quantify another reactive nitrogen species; nitrous acid. Nitrous acid, or HONO, itself also poses questions as to it's origin in many situations as in chapter 4, seemingly emitted by surfaces and bacteria alike. A simple *in-situ* measurement based on photolysis and detection as NO with fast response was built, characterised, and deployed. During an atmospheric simulation chamber comparison, the HONO measured corresponded well with FT-IR measurement. During field tests the photolytic HONO instrument agreed reasonably well with the established LOPAP instrument, though the limitations of having a two-channel sequential measurement were apparent at times, this would be easily overcome in a three-channel concurrent system.

Finally, through interpretation of NO, NO_2, and HONO data collected at the Cape Verde observatory it was shown that fast aerosol nitrate photolysis is likely the primary source of NO_x in the remote tropical Atlantic boundary layer. By using A 0-D model which contains relevant O_x, HO_x, NO_x, halogen and the MCM VOC reaction scheme it was possible to approximate halogen, O_3, OH, NO_x, and HONO observations when particulate nitrate photolysis was included as a source of NO_x at a rate of ~ 10 times that of gas phase nitric

acid. Additionally, the inclusion of newly posited reactions between halogen oxides and the nitrate radical resulted in the best agreement between modelled and observed NO_x and HONO data suggesting a role for these theoretical reactions.

Another study of nitrate photolysis in the remote boundary layer found photolysis rate of surface nitrate ~ 3 orders of magnitude greater than that of gas phase nitric acid Ye et al. (2016b). However, when the same rate is included in the DSMACC model as presented in chapter 4 Fig 4.4 it is clear that there is poor agreement with observations. The Ye et al. 2016b study is based upon laboratory studies of a filter samples collected aboard the NSF/NCAR C-130 aicraft during the Nitrogen, Oxidants, Mercury and Aerosol Distributions, Sources and Sinks (NOMADSS) study. It may be that the nature of sea salt nitrate aerosol collected on these filters in the NOMADSS study offer a much enhanced photolysis rate to the saharan dust nitrate aerosol predominant at Cape Verde.

A further more recent modelling study of Cape Verde data by Ye et al. 2017 sought to interpret NO_x and HONO observations made during the RHaMBLe campaign of 2007. Though the data pre-dates that used in chapter 4, the study is more recent. In the study of Ye et al. (2017) a 0-D model, combined with NO and NO_2 data from the Cape Verde observatory, plus HONO data collected by mist chamber coupled to ion chromatography was set up in order to test the applicability of nitrate photolysis. In that work NO_x and HONO are modelled during daylight hours from 2 hours after sunrise to 2 hours before sunset. Ye et al. (2017) find a nitrate photolysis rate scaled to 15 times that of gas phase nitric acid is sufficient to loosely reproduce the observed NO_x and HONO. This is in line with the 10x used in chaper 4, however Ye et al. (2017) do not consider and transport of reactive nitrogen e.g. PAN which is a sink in their model and the second biggest source in chaper 4. Ye et al. (2017) state that observations of PANs and their precursors featuring a peak at noon to afternoon points to a PAN sink for NO_x, however the model study in chapter 4 shows that this is entirely consistent with PAN being a net source of NO_x at Cape Verde. In fact, without a thermal (from e.g. PAN) or direct source of NO_x it decrease over night – inconsistent with the build-up seen in observations.

The study of Ye et al. (2017) includes cycling of halogen nitrates as a mechanism of NO_x recycling as in chapter 4, however the gamma (γ) used is 0.8 as recommended by JPL (Burkholder et al., 2015) which was shown to result in halogen oxide diurnal profiles which dissagree with what was observed by Mahajan et al. (2010a), though halogen oxides, and

by extension their effect on O_3 are not presented in Ye et al. (2017).

The picture of NO_x chemistry in the remote marine boundary layer can now be updated with this new knowledge from that presented in the introduction (Fig. 1.2) to that shown here in figure 5.1.

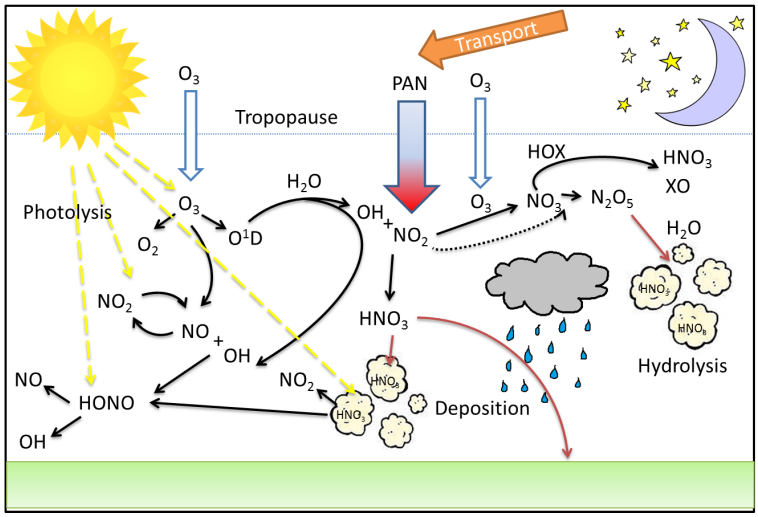

Figure 5.1 – A simplified representation of NO_x chemistry in the remote boundary layer updated to include photolysis of nitrate and HOX + NO_3 reactions.

With more understanding of what NO_x chemistry is occurring, simulation of the coupled oxidation chemistry is improved with respect to the observations. Inclusion of this new chemistry will allow the lifetime of oxidants, and the fate of emissions to be modelled with more certainty.

The implications of nitrate photolysis as a source of NO_x on the wider atmosphere where the effect may be more subtle due to convolution with direct emission deserve further study. It may be that nitrate photolysis is able to explain gaps between models based upon emission inventories and observations, for example. A greater number of measurements of HONO, PAN, NO_x and particulate nitrate in remote regions would help narrow down the range nitrate photolysis rates, whilst global modelling that includes nitrate photolysis will determine what effect its inclusion has on discrepancies between current models and observations.

Furthermore, a new fast response HONO instrument described in chapter 3 of this thesis could prove beneficial in accurately determining HONO fluxes. Further development into a system with two dedicated photolysis channels should eliminated much of the variability

and noise sen with the single switching channel system used in chapter 3. Fast respnse, high sensitivity, and minimal interferneces would be beneficial in polluted areas where surface production of HONO and NO_2 could be significant, albeit subtle, contributors to the overall reactive nitrogen budget. Coupled with fast aerosol nitrate measurements, a fast and accurate HONO measurement would be invaluble in deterimning $HONO : NO_2$ branching ratios from nitrate photolysis *in-situ*.

Appendix A

Tables of chemical reaction rates and reactive uptake coefficients used in the DSMACC model

Rates used in the DSMACC model were primarily taken from IUPAC and JPL recommendations respectively only if both sources recommended a rate. Rates from JPL took preference to those of IUPAC due to their being more up to date.

Table A.1 – Rates of O_x reactions used in DSMACC model.

#	Reaction	K / cm^3 $molecule^{-1}$ s^{-1}	Ref
1	$O^3P + O_2 \rightarrow O_3$	1.40×10^{-14a}	[1,2]
2	$O^3P + O_3 \rightarrow 2\,O_2$	$8.00 \times 10^{-12} e^{(-2060/T)}$	[2]
3	$O^1D + O_2 \rightarrow O^3P + O_2$	$3.30 \times 10^{-11} e^{(55/T)}$	[2]
4	$O^1D + N_2 \rightarrow O^3P + N_2$	$2.15 \times 10^{-11} e^{(110/T)}$	[2]
5	$O^1D + H_2O \rightarrow 2\,OH$	$1.63 \times 10^{-10} e^{(60/T)}$	[2]
6	$O^1D + O_3 \rightarrow O^3P$	2.40×10^{-10b}	[2]

[a] Formally a pressure depedent reaction in the DSMACC model, quoted here at 300 K and 1 bar N_2. See ref 2 for k_o, K_{inf} and F_c.

[b] value independent of temperature over the range 103–393 K.

[1] Atkinson et al. (2004)

[2] Burkholder et al. (2015)

Table A.2 – Rates of HO_x reactions used in DSMACC model.

#	Reaction	K / cm^3 $molecule^{-1}$ s^{-1}	Ref
1	$O + OH \rightarrow H + O_2$	$1.80 \times 10^{-11} e^{(180/T)}$	[2]
2	$O + HO_2 \rightarrow OH + O_2$	$3.00 \times 10^{-11} e^{(200/T)}$	[2]
3	$O + H_2O_2 \rightarrow OH + HO_2$	$1.40 \times 10^{-10} e^{(-2000/T)}$	[2]
4	$H + O_3 \rightarrow OH + O_2$	$1.40 \times 10^{-10} e^{(-470/T)}$	[2]
5	$H + HO_2 \rightarrow 2\,OH$	7.20×10^{-11} [a]	[2]
6	$OH + O_3 \rightarrow HO_2 + O_2$	$1.70 \times 10^{-12} e^{(-940/T)}$	[2]
7	$OH + OH \rightarrow O + H_2O$	1.80×10^{-12} [b]	[2]
8	$OH + HO_2 \rightarrow H_2O + O_2$	$4.80 \times 10^{-11} e^{(250/T)}$	[2]
9	$OH + H_2O_2 \rightarrow HO_2$	$2.90 \times 10^{-12} e^{(-160/T)}$	[1]
10	$OH + H_2 \rightarrow H_2O + H$	$2.80 \times 10^{-12} e^{(-1800/T)}$	[2]
11	$OH + CO \rightarrow HO_2$	$1.44 \times 10^{-13} \times$ KMT05*	[1]
12	$HO_2 + O_3 \rightarrow OH + O_2$	$1.00 \times 10^{-14} e^{(-490/T)}$	[2]
13	$2\,HO_2 \rightarrow H_2O_2$	$2.20 \times 10^{-13} \times$ KMT06* $\times e^{(600/T)} +$ $1.90 \times 10^{-33} \times [M] \times$ KMT06* $\times e^{(980/T)}$	[1]

* See table A.8

[a] value independent of temperature over the range 245–300 K.

[b] value independent of temperature over the range 233–580 K.

[1] Atkinson et al. (2004)

[2] Burkholder et al. (2015)

Table A.3 – Rates of NO_x reactions used in DSMACC model.

#	Reaction	K / cm^3 $molecule^{-1}$ s^{-1}	Ref
1	$O + NO \rightarrow NO_2$	KMT01*	[1]
2	$O + NO_2 \rightarrow NO_3$	KMT02*	[1]
3	$O + NO_3 \rightarrow NO_2 + O_2$	$1.00 \times 10^{-11 a}$	[2]
4	$O + NO_2 \rightarrow NO + O_2$	$5.10 \times 10^{-12} e^{(210/T)}$	[2]
5	$H + NO_2 \rightarrow OH + NO$	$4.00 \times 10^{-10} e^{(-3400/T)}$	[2]
6	$OH + HONO \rightarrow NO_2 + H_2O$	$2.50 \times 10^{-12} e^{(260/T)}$	[1]
7	$HO_2 + NO \rightarrow OH + NO_2$	$3.30 \times 10^{-12} e^{(270/T)}$	[2]
8	$HO_2 + NO_2 \rightarrow HO_2NO_2$	KMT09*	[1]
9	$HO_2 + NO_3 \rightarrow OH + NO_2$	$4.00 \times 10^{-12 b}$	[1]
10	$NO + O_3 \rightarrow NO_2 + O_2$	$3.00 \times 10^{-12} e^{(-1500/T)}$	[2]
11	$NO + NO_3 \rightarrow NO_2 + NO_2$	$1.50 \times 10^{-11} e^{(170/T)}$	[2]
12	$NO_2 + O_3 \rightarrow NO_3$	$1.20 \times 10^{-13} e^{(-2450/T)}$	[2]
13	$NO_2 + NO_3 \rightarrow NO + NO_2 + O_2$	$4.50 \times 10^{-14} e^{(1260/T)}$	[2]
14	$2\,NO_3 \rightarrow 2\,NO_2 + O_2$	$8.50 \times 10^{-13} e^{(-2450/T)}$	[2]
15	$NO_2 + NO_3 \rightarrow N_2O_5$	KMT03*	[1]
16	$N_2O_5 \rightarrow NO_2 + NO_3$	KMT04*	[1]
17	$OH + NO \rightarrow HONO$	KMT07*	[1]
18	$OH + NO_2 \rightarrow HNO_3$	KMT08*	[1]
19	$OH + NO_3 \rightarrow HO_2 + NO_2$	$2.00 \times 10^{-11 c}$	[1]
20	$HO_2NO_2 \rightarrow HO_2 + NO_2$	KMT10*	[1]
21	$OH + HNO_3 \rightarrow NO_3 + H_2O$	KMT11*	[1]
22	$OH + HO_2NO_2 \rightarrow NO_2 + prods$	$3.20 \times 10^{-12} e^{(690/T)}$	[1]

* See table A.8

[a] value independent of temperature over the range 298–329 K.

[b] at 298 K.

[c] at 298 K.

[1] Atkinson et al. (2004)

[2] Burkholder et al. (2015)

Table A.4 – Rates of Bromine reactions used in DSMACC model.

#	Reaction	K / cm^3 $molecule^{-1}$ s^{-1}	Ref
1	$Br + O_3 \rightarrow BrO + O_2$	$1.70 \times 10^{-11} e^{(-800/T)}$	[1]
2	$BrO + NO_2 + M \rightarrow BrNO_3 + M$	$5.20 \times 10^{-31} (T/300)^{-3.2}$	[2]
3	$BrNO_3 \rightarrow BrO + NO_2$	$2.00 \times 10^{13} e^{(-12360/T)}$	[3]
4	$BrO + HO_2 \rightarrow HOBr + O_2$	$4.50 \times 10^{-12} e^{(500/T)}$	[1]
5	$Br + HO_2 \rightarrow HBr + O_2$	$4.80 \times 10^{-12} e^{(-310/T)}$	[2]
6	$HBr + OH \rightarrow Br + H_2O$	$6.70 \times 10^{-12} e^{(155/T)}$	[1]
7	$BrO + NO \rightarrow Br + NO_2$	$8.70 \times 10^{-12} e^{(260/T)}$	[1]
8	$2\,BrO \rightarrow 2\,Br + O_2$	2.70×10^{-12} [a]	[1]
9	$2\,BrO \rightarrow Br_2 + O_2$	$2.90 \times 10^{-14} e^{(840/T)}$	[1]
10	$Br + HCHO \rightarrow HBr + HO_2$	$1.70 \times 10^{-11} e^{(-800/T)}$	[2]
11	$Br + NO_3 \rightarrow BrO + NO_2$	1.60×10^{-11} [b]	[1,2]
12	$HOBr + NO_3 \rightarrow BrO + HNO_3$	$2.70 \times 10^{-11} e^{(300/T)^{2.66}}$	*This work*

[a] value independent of temperature over the range 250–390 K.

[b] at 298 K.

[1] Atkinson et al. (2007)

[2] Burkholder et al. (2015)

[3] Orlando and Tyndall (1996)

Table A.5 – Rates of Iodine reactions used in DSMACC model.

#	Reaction	K / cm^3 $molecule^{-1}$ s^{-1}	Ref
1	$I + HO_2 \rightarrow HI + O_2$	$1.50 \times 10^{-11} e^{(-1190/T)}$	[1]
2	$IO + NO_2 + M \rightarrow INO_3 + M$	$7.70 \times 10^{-31} (T/300)^{-5}$	[1]
3	$INO_3 \rightarrow IO + NO_2$	$1.10 \times 10^{15} e^{(-12060/T)}$	[1]
4	$OH + HI \rightarrow I + H_2O$	$1.60 \times 10^{-11} e^{(440/T)}$	[3]
5	$IO + NO \rightarrow NO_2 + I$	$7.15 \times 10^{-12} e^{(300/T)}$	[1]
6	$I + O_3 \rightarrow IO + O_2$	$2.30 \times 10^{-11} e^{(-870/T)}$	[3]
7	$IO + HO_2 \rightarrow HOI + O_2$	$1.40 \times 10^{-11} e^{(540/T)}$	[1]
8	$HOI + OH \rightarrow IO + H_2O$	5.00×10^{-12} [a]	[4]
9	$2\,IO \rightarrow I + OIO$	$0.38 \times (5.40 \times 10^{-11} e^{(180/T)})$	[1,2]
10	$2\,IO \rightarrow 2\,I + O_2$	$0.11 \times (5.40 \times 10^{-11} e^{(180/T)})$	[1,2]
11	$OIO + NO \rightarrow IO + NO_2$	$1.10 \times 10^{-12} e^{(542/T)}$	[5]
12	$I_2 + NO_3 \rightarrow INO_3 + I$	1.50×10^{-12} [b]	[1]
13	$I + NO_3 \rightarrow IO + NO_2$	1.00×10^{-10} [c]	[1]
14	$HOI + NO_3 \rightarrow IO + HNO_3$	$2.70 \times 10^{-12} e^{(300/T)^{2.66}}$	[6]

[a] at 320 K.

[b] value independent of temperature over the range 292–423 K.

[c] at 298 K.

[1] Atkinson et al. (2007)

[2] Bloss et al. (2001)

[3] Burkholder et al. (2015)

[4] Riffault et al. (2005)

[5] Plane et al. (2006)

[6] Saiz-Lopez et al. (2016)

Table A.6 – Rates of mixed halogen reactions used in DSMACC model.

#	Reaction	K / cm^3 $molecule^{-1}$ s^{-1}	Ref
1	$BrO + IO \rightarrow Br + 0.8\,OIO + 0.2\,I$	$1.5 \times 10^{-11} e^{(510/T)}$	[1]
2	$I + BrO \rightarrow IO + Br$	1.20×10^{-11} [a]	[2]
3	$Br + IO \rightarrow BrO + I$	2.50×10^{-11} [a]	[3]

[a] at 298 K.

[1] Atkinson et al. (2007)

[2] Burkholder et al. (2015)

[3] Bedjanian et al. (1998)

Table A.7 – Aerosol reactive uptake coefficients (γ) used in DSMACC model in the form UPTAKE(γ, T, Surface Area, Mass).

#	Reaction	γ	Ref
1	$N_2O_5 \rightarrow 2\,p{-}NO_3$	0.02	[2][a]
2	$HNO_3 \rightarrow p{-}NO_3$	0.15	[2][a]
3	$NO_3 \rightarrow p{-}NO_3$	0.012	[2][a]
4	$HOBr \rightarrow 0.5\,Br_2$	0.02–0.80[b]	[3]
5	$BrNO_3 \rightarrow HOBr + p{-}NO_3$	0.02–0.80[b]	[1,3]
6	$HBr \rightarrow 0.5\,Br_2$	0.02–0.80[b]	[3]
7	$HOI \rightarrow 0.5\,I_2$	0.02–0.80[b]	[3]
8	$HI \rightarrow 0.5\,I_2$	0.02–0.80[b]	[3]
9	$INO_3 \rightarrow HOI + p{-}NO_3$	0.02–0.80[b]	[1,3]

[a] Data from IUPAC datasheets of uptake coefficients on Saharan dust.

[b] Sensitivity analysis performed on uptake coefficients.

[1] Burkholder et al. (2015)

[2] Crowley et al. (2010)

[3] Saiz-Lopez et al. (2008)

Table A.8 – Complex rate coefficients of pressure dependent reactions used in the DSMACC model taken from the MCM model.

#			Ref
KMT01	K_0	$1.00 \times 10^{-31} \times [M] \times (T/300)^{-1.6}$	[1]
	K_{inf}	$3.00 \times 10^{-11} \times (T/300)^{0.3}$	
	F_c	0.85	
KMT02	K_0	$1.30 \times 10^{-31} \times [M] \times (T/300)^{-1.5}$	[1]
	K_{inf}	$2.30 \times 10^{-11} \times (T/200)^{0.24}$	
	F_c	0.6	
KMT03	K_0	$3.60 \times 10^{-30} \times (T/300)^{-4.1} \times [M]$	[1]
	K_{inf}	$1.90 \times 10^{-12} \times (T/300)^{0.2}$	
	F_c	0.35	
KMT04	K_0	$1.00 \times 10^{-3} \times (T/300)^{-3.5 \times e^{(-11000/T)} \times [M]}$	[1]
	K_{inf}	$9.70 \times 10^{14} \times (T/300)^{0.1 \times e^{(-11080/T)}}$	
	F_c	0.35	
KMT05	K_0	$1 + ((0.6 \times [M])/(2.652 \times 10^{19} \times (300/T)))$	[1]
KMT06	K_0	$1 + (1.40 \times 10^{-21} \times e^{(2200/T)} \times [H_2O])$	[1]
KMT07	K_0	$7.40 \times 10^{-31} \times (T/300)^{-2.4} \times [M]$	[1]
	K_{inf}	$3.30 \times 10^{-11} \times (T/300)^{-0.3}$	
	F_c	$e^{(-T/1420)}$	
KMT08	K_0	$3.30 \times 10^{-30} \times (T/300)^{-3.0} \times [M]$	[1]
	K_{inf}	4.10×10^{-11}	
	F_c	0.4	
KMT09	K_0	$1.80 \times 10^{-31} \times (T/300)^{-3.2} \times [M]$	[1]
	K_{inf}	4.70×10^{-12}	
	F_c	0.6	

Continued overleaf...

Table A.8 - continued.

#			Ref
KMT10	K_0	$4.10 \times 10^{-5} \times e^{(-10650/T)} \times [M]$	[1]
	K_{inf}	$4.80 \times 10^{15} \times e^{(-11170/T)}$	
	F_c	0.5	
KMT11	$K_1 + K_2$		[1]
	K_1	$2.40 \times 10^{-14} \times e^{(460/T)}$	
	K_2	$(K_3 \times [M])/(1 + (K_3 \times [M]/K_4)$	
	K_3	$6.50 \times 10^{-34} \times e^{(1335/T)}$	
	K_4	$2.70 \times 10^{-17} \times e^{(2199/T)}$	

[1] Atkinson et al. (2004)

NOTE: The chemical mechanistic information was taken from the Master Chemical Mechanism, MCM v3.3.1 (Jenkin et al., 1997; Saunders et al., 2003), via website: http://mcm.leeds.ac.uk/MCM

Abbreviations

AIM-IC	ambient ion monitor ion chromatography
ANs	alkyl nitrates
AQD	Air Quality Design Inc.
ASTEX	Atlantic Stratocumulus Transition Experiment
BLC	blue light converter
BOC	British Oxygen Company
CAPS	cavity attenuated phase shift
cps	counts per second
CRDS	cavity ring-down spectroscopy
CVO	Cape Verde Atmospheric Observatory
DOAS	differential optical absorption spectroscopy
DSMACC	Dynamically Simple Model of Atmospheric Chemical Complexity
EPA	Environmental Protection Agency
FAGE	fluorescence assay by gas expansion
FT-IR	Fourier transform-infra red
GAW	Global Atmospheric Watch
HIRAC	highly instrumented reactor for atmospheric chemistry
HPLC	high pressure liquid chromatography
Hz	hertz

IBBCEAS	incoherent broadband cavity enhanced absorption spectroscopy
ICOZA	Integrated chemistry of ozone in the atmosphere
ID-CIMS	ion drift chemical ionisation mass spectrometry
IUPAC	International Union of Pure and Applied Chemistry
JPL	(NASA) Jet Propulsion Laboratory
KPP	Kinetic Pre-processor
LED	light emitting diode
LIF	laser-induced fluorescence
LOD	limit of detection
LOPAP	LOng Path Absorption Photometer
LT	local time
MBL	marine boundary layer
MCM	Master Chemical Mechanism
MFC	mass flow controller
NI-PT-CIMS	negative-ion proton-transfer chemical ionisation mass spectrometry
NIST	National Institute of Standards and Technology
PAG	pure air generator
PAN	peroxy acetyl nitrate
PAN-GC	peroxy acetyl nitrate gas chromatograph
PERCA	PEroxy Radical Chemical Amplification
PFA	perfluoroalkoxy alkane
pHONO	photolytic HONO

PLC	photolytic converter
PM	particulate matter
PMT	photomultiplier tube
PNs	peroxy nitrates
ppb	parts per billion
ppt	parts per trillion
PSS	photo-stationary steady state
QCL	quantum cascade laser
QC-TILDAS	quantum cascade tunable infra-red laser differential absorption spectroscopy
RHaMBLe	Reactive Halogens in the Marine Boundary Layer
SATP	standard atmospheric temperature and pressure
SC-AP	stripping coil–visible absorption photometry
TD-LIF	thermal dissociation laser-induced fluorescence
TUV	Tropospheric Ultraviolet and Visible model
UHP	ultra-high purity
UTC	Coordinated Universal Time
UTLS	upper troposphere–lower stratosphere
UV	ultra violet
UV-LED	ultra violet-light emitting diode
VOC	volatile organic compounds
WAO	Weybourne Atmospheric Observatory
WMO	World Meteorological Organization

References

Abbatt, J. P. D., Lee, A. K. Y., and Thornton, J. A.: Quantifying trace gas uptake to tropospheric aerosol: recent advances and remaining challenges, Chemical Society Reviews, 41, 6555, doi:10.1039/c2cs35052a, 2012.

Acker, K., Möller, D., Auel, R., Wieprecht, W., and Kalaß, D.: Concentrations of nitrous acid, nitric acid, nitrite and nitrate in the gas and aerosol phase at a site in the emission zone during ESCOMPTE 2001 experiment, Atmospheric Research, 74, 507–524, doi:10.1016/j.atmosres.2004.04.009, 2005.

Acker, K., Möller, D., Wieprecht, W., Meixner, F. X., Bohn, B., Gilge, S., Plass-Dülmer, C., and Berresheim, H.: Strong daytime production of OH from HNO_2 at a rural mountain site, Geophysical Research Letters, 33, 2–5, doi:10.1029/2005GL024643, 2006.

Ainsworth, E. A., Yendrek, C. R., Sitch, S., Collins, W. J., and Emberson, L. D.: The Effects of Tropospheric Ozone on Net Primary Productivity and Implications for Climate Change, Annual Review of Plant Biology, 63, 637–661, doi:10.1146/annurev-arplant-042110-103829, 2012.

Ashmore, M. R.: Assessing the future global impacts of ozone on vegetation, Plant, Cell and Environment, 28, 949–964, doi:10.1111/j.1365-3040.2005.01341.x, 2005.

Atkinson, R.: Atmospheric chemistry of VOCs and NO_x, Atmospheric Environment, 34, 2063–2101, doi:10.1016/S1352-2310(99)00460-4, 2000.

Atkinson, R., Baulch, D. L., Cox, R. A., Crowley, J. N., Hampson, R. F., Hynes, R. G., Jenkin, M. E., Rossi, M. J., and Troe, J.: Evaluated kinetic and photochemical data for atmospheric chemistry: Volume I - gas phase reactions of O_x, HO_x, NO_x and SO_x species, Atmospheric Chemistry and Physics, 4, 1461–1738, doi:10.5194/acp-4-1461-2004, 2004.

Atkinson, R., Baulch, D. L., Cox, R. A., Crowley, J. N., Hampson, R. F., Hynes, R. G., Jenkin, M. E., Rossi, M. J., and Troe, J.: Evaluated kinetic and photochemical data for atmospheric chemistry: Volume II – gas phase reactions of organic species, Atmospheric Chemistry and Physics, 6, 3625–4055, doi:10.5194/acp-6-3625-2006, 2006.

Atkinson, R., Baulch, D. L., Cox, R. A., Crowley, J. N., Hampson, R. F., Hynes, R. G., Jenkin, M. E., Rossi, M. J., and Troe, J.: Evaluated kinetic and photochemical data for atmospheric chemistry: Volume III - gas phase reactions of inorganic halogens, Atmospheric Chemistry and Physics, 7, 981–1191, doi:10.5194/acp-7-981-2007, 2007.

Baergen, A. M. and Donaldson, D. J.: Photochemical renoxification of nitric acid on real urban grime, Environmental Science & Technology, 47, 815–820, doi:10.1021/es3037862, 2013.

Baergen, A. M. and Donaldson, D. J.: Formation of reactive nitrogen oxides from urban grime photochemistry, Atmospheric Chemistry and Physics, 16, 6355–6363, doi:10.5194/acp-16-6355-2016, 2016.

Barney, W. S., Wingen, L. M., Lakin, M. J., Brauers, T., Stutz, J., and Finlayson-Pitts, B. J.: Infrared Absorption Cross-Section Measurements for Nitrous Acid (HONO) at Room Temperature, The Journal of Physical Chemistry A, 104, 1692–1699, doi:10.1021/jp9930503, 2000.

Barry, R. G., Chorley, R. J., and Serreze, M. C.: Atmosphere, Weather and Climate, Taylor & Francis Ltd, 2009.

Bauguitte, S. J. B., Bloss, W. J., Evans, M. J., Salmon, R. A., Anderson, P. S., Jones, A. E., Lee, J. D., Saiz-Lopez, A., Roscoe, H. K., Wolff, E. W., and Plane, J. M. C.: Summertime NO_x measurements during the CHABLIS campaign: Can source and sink estimates unravel observed diurnal cycles?, Atmospheric Chemistry and Physics, 12, 989–1002, doi:10.5194/acp-12-989-2012, 2012.

Bedjanian, Y., le Bras, G., and Poulet, G.: Kinetic study of the reactions Br + IBr $\rightarrow$ I + Br_2 and I + Br_2 $\rightarrow$ Br + IBr, International Journal of Chemical Kinetics, 30, 933–940, doi:10.1002/(sici)1097-4601(1998)30:12<933::aid-kin8>3.0.co;2-y, 1998.

Beine, H., Colussi, A. J., Amoroso, A., Esposito, G., Montagnoli, M., and Hoffmann,

M. R.: HONO emissions from snow surfaces, Environmental Research Letters, 3, 045 005, doi:10.1088/1748-9326/3/4/045005, 2008.

Beine, H. J., Amoroso, A., Dominé, F., King, M. D., Nardino, M., Ianniello, A., and France, J. L.: Surprisingly small HONO emissions from snow surfaces at Browning Pass, Antarctica, Atmospheric Chemistry and Physics, 6, 2569–2580, doi:10.5194/acp-6-2569-2006, 2006.

Beirle, S., Platt, U., von Glasow, R., Wenig, M., and Wagner, T.: Estimate of nitrogen oxide emissions from shipping by satellite remote sensing, Geophysical Research Letters, 31, 4–7, doi:10.1029/2004GL020312, 2004.

Bey, I., Jacob, D. J., Yantosca, R. M., Logan, J. A., Field, B. D., Fiore, A. M., Li, Q., Liu, H. Y., Mickley, L. J., and Schultz, M. G.: Global modeling of tropospheric chemistry with assimilated meteorology: Model description and evaluation, Journal of Geophyscial Research, 106, 23 073–23 095, doi:10.1029/2001JD000807, 2001.

Bloss, C., Wagner, V., Jenkin, M. E., Volkamer, R., Bloss, W. J., Lee, J. D., Heard, D. E., Wirtz, K., Martin-Reviejo, M., Rea, G., Wenger, J. C., and Pilling, M. J.: Development of a detailed chemical mechanism (MCMv3.1) for the atmospheric oxidation of aromatic hydrocarbons, Atmospheric Chemistry and Physics, 5, 641–664, doi:10.5194/acp-5-641-2005, 2005.

Bloss, W. J., Rowley, D. M., Cox, R. A., and Jones, R. L.: Kinetics and Products of the IO Self-Reaction, The Journal of Physical Chemistry A, 105, 7840–7854, doi:10.1021/jp0044936, 2001.

Boggs, P. T., Byrd, R. H., and Schnabel, R. B.: A Stable and Efficient Algorithm for Nonlinear Orthogonal Distance Regression, SIAM Journal on Scientific and Statistical Computing, 8, 1052–1078, doi:10.1137/0908085, 1987.

Bridier, I., Caralp, F., Loirat, H., Lesclaux, R., Veyret, B., Becker, K. H., Reimer, A., and Zabel, F.: Kinetic and theoretical studies of the reactions acetylperoxy + nitrogen dioxide + $M \rightleftharpoons$ acetyl peroxynitrate + M between 248 and 393 K and between 30 and 760 torr, The Journal of Physical Chemistry, 95, 3594–3600, doi:10.1021/j100162a031, 1991.

Bröske, R., Kleffmann, J., and Wiesen, P.: Heterogeneous conversion of NO_2 on secondary organic aerosol surfaces: A possible source of nitrous acid (HONO) in the atmosphere?, Atmospheric Chemistry and Physics, 3, 469–474, doi:10.5194/acp-3-469-2003, 2003.

Brown, S. S., Dibb, J. E., Stark, H., Aldener, M., Vozella, M., Whitlow, S., Williams, E. J., Lerner, B. M., Jakoubek, R., Middlebrook, A. M., DeGouw, J. A., Warneke, C., Goldan, P. D., Kuster, W. C., Angevine, W. M., Sueper, D. T., Quinn, P. K., Bates, T. S., Meagher, J. F., Fehsenfeld, F. C., and Ravishankara, A. R.: Nighttime removal of NO_x in the summer marine boundary layer, Geophysical Research Letters, 31, 2–6, doi:10.1029/2004GL019412, 2004.

Brown, S. S., Osthoff, H. D., Stark, H., Dubé, W. P., Ryerson, T. B., Warneke, C., de Gouw, J. A., Wollny, A. G., Parrish, D. D., Fehsenfeld, F. C., and Ravishankara, A. R.: Aircraft observations of daytime NO_3 and N_2O_5 and their implications for tropospheric chemistry, Journal of Photochemistry and Photobiology A: Chemistry, 176, 270–278, doi:10.1016/j.jphotochem.2005.10.004, 2005.

Browne, E. C., Perring, A. E., Wooldridge, P. J., Apel, E., Hall, S. R., Huey, L. G., Mao, J., Spencer, K. M., Clair, J. M. S., Weinheimer, A. J., Wisthaler, A., and Cohen, R. C.: Global and regional effects of the photochemistry of $CH_3O_2NO_2$: evidence from ARCTAS, Atmospheric Chemistry and Physics, 11, 4209–4219, doi:10.5194/acp-11-4209-2011, 2011.

Buhr, M.: Measurement of NO_2 in ambient air using a solid-state photolytic converter, in: Symposium on Air Quality Measurement Methods and Technology 2004. 20 - 22 April 2004, pp. 165–171, 2004.

Buhr, M.: Solid-state light source photolytic nitrogen dioxide converter, US 7238328 B2, United States, USTPO, 2007.

Burkert, J., Andrés-Hernández, M.-D., Stbener, D., Burrows, J. P., Weissenmayer, M., and Kraus, A.: Peroxy radical and related trace gas measurements in the boundary layer above the Atlantic Ocean, Journal of Geophysical Research: Atmospheres, 106, 5457–5477, doi:10.1029/2000jd900613, 2001.

Burkholder, J. B., Sander, S. P., Abbatt, J., Barker, J. R., Huie, R. E., Kolb, C. E., Kurylo, M. J., Orkin, V. L., Wilmouth, D. M., and Wine, P. H.: Chemical Kinetics and

Photochemical Data for Use in Atmospheric Studies, Evaluation No. 18, JPL Publication 15-10, 15, 2015.

Cantrell, C. A., Shetter, R. E., Calvert, J. G., Eisele, F. L., Williams, E., Baumann, K., Brune, W. H., Stevens, P. S., and Mather, J. H.: Peroxy radicals from photostationary state deviations and steady state calculations during the Tropospheric OH Photochemistry Experiment at Idaho Hill, Colorado, 1993, Journal of Geophyscial Research, 102, 6369, doi:10.1029/96JD01703, 1997.

Cantrell, C. A., Mauldin, L., Zondlo, M., Eisele, F. L., Kosciuch, E., Shetter, R. E., Lefer, B., Hall, S., Campos, T. L., Ridley, B., Walega, J. G., Fried, A., Wert, B., Flocke, F. M., Weinheimer, A. J., Hannigan, J., Coffey, M., Atlas, E., Stephens, S., Heikes, B. G., Snow, J., Blake, D. R., Blake, N., Katzenstein, A., Lopez, J., Browell, E. V., Dibb, J. E., Scheuer, E., Seid, G., and Talbot, R. W.: Steady state free radical budgets and ozone photochemistry during TOPSE, Journal of Geophysical Research, 108, doi:10.1029/2002JD002198, 2003.

Carbajo, P. G. and Orr-Ewing, A. J.: NO_2 quantum yields from ultraviolet photodissociation of methyl and isopropyl nitrate, Physical Chemistry Chemical Physics, 12, 6084, doi:10.1039/c001425g, 2010.

Carpenter, L. J., Fleming, Z. L., Read, K. A., Lee, J. D., Moller, S. J., Hopkins, J. R., Purvis, R. M., Lewis, A. C., Müller, K., Heinold, B., Herrmann, H., Fomba, K. W., Pinxteren, D., Müller, C., Tegen, I., Wiedensohler, A., Müller, T., Niedermeier, N., Achterberg, E. P., Patey, M. D., Kozlova, E. A., Heimann, M., Heard, D. E., Plane, J. M. C., Mahajan, A., Oetjen, H., Ingham, T., Stone, D., Whalley, L. K., Evans, M. J., Pilling, M. J., Leigh, R. J., Monks, P. S., Karunaharan, A., Vaughan, S., Arnold, S. R., Tschritter, J., Pöhler, D., Frieß, U., Holla, R., Mendes, L. M., Lopez, H., Faria, B., Manning, A. J., and Wallace, D. W. R.: Seasonal characteristics of tropical marine boundary layer air measured at the Cape Verde Atmospheric Observatory, Journal of Atmospheric Chemistry, 67, 87–140, doi:10.1007/s10874-011-9206-1, 2010.

Carroll, R. J. and Ruppert, D.: The Use and Misuse of Orthogonal Regression in Linear Errors-in-Variables Models, The American Statistician, 50, 1–6, doi:10.1080/00031305.1996.10473533, 1996.

Carsey, T. P., Churchill, D. D., Farmer, M. L., Fischer, C. J., Pszenny, A. A., Ross, V. B.,

Saltzman, E. S., Springer-Young, M., Bonsang, B., Boss, V. B., Saltzmann, E. S., Springer-Young, M., and Bonsang, B.: Nitrogen oxides and ozone production in the North Atlantic marine boundary layer, Journal of Geophyscial Research, 102, 653–665, doi:10.1029/96JD03511, 1997.

Carslaw, D.: Evidence of an increasing NO_2/NO_x emissions ratio from road traffic emissions, Atmospheric Environment, 39, 4793–4802, doi:10.1016/j.atmosenv.2005.06.023, 2005.

Carslaw, N., Carpenter, L. J., Plane, J. M. C., Allan, B. J., Burgess, R. A., Clemitshaw, K. C., Coe, H., and Penkett, S. A.: Simultaneous observations of nitrate and peroxy radicals in the marine boundary layer, Journal of Geophysical Research: Atmospheres, 102, 18 917–18 933, doi:10.1029/97jd00399, 1997.

Chameides, W. L. and Davis, D. D.: Iodine: Its possible role in tropospheric photochemistry, Journal of Geophysical Research: Oceans, 85, 7383–7398, doi:10.1029/jc085ic12p07383, 1980.

Clemitshaw, K. C.: A Review of Instrumentation and Measurement Techniques for Ground-Based and Airborne Field Studies of Gas-Phase Tropospheric Chemistry, Critical Reviews in Environmental Science and Technology, 34, 1–108, doi:10.1080/10643380490265117, 2004.

Clemitshaw, K. C., Carpenter, L. J., Penkett, S. A., and Jenkin, M. E.: A calibrated peroxy radical chemical amplifier for ground-based tropospheric measurements, Journal of Geophysical Research, 102, 25 405–25 416, doi:10.1029/97JD01902, 1997.

Cleveland, W. S.: Robust Locally Weighted Regression and Smoothing Scatterplots, Journal of the American Statistical Association, 74, 829, doi:10.2307/2286407, 1979.

Clough, P. N. and Thrush, B. A.: Mechanism of chemiluminescent reaction between nitric oxide and ozone, Transactions of the Faraday Society, 63, 915, doi:10.1039/tf9676300915, 1967.

Clyne, M. A. A., Thrush, B. A., and Wayne, R. P.: Kinetics of the chemiluminescent reaction between nitric oxide and ozone, Transactions of the Faraday Society, 60, 359, doi:10.1039/tf9646000359, 1964.

Cohan, A., Chang, W., Carreras-Sospedra, M., and Dabdub, D.: Influence of sea-salt activated chlorine and surface-mediated renoxification on the weekend effect in the South Coast Air Basin of California, Atmospheric Environment, 42, 3115–3129, doi:10.1016/j.atmosenv.2007.11.046, 2008.

Cooper, O. R., Parrish, D. D., Ziemke, J., Balashov, N. V., Cupeiro, M., Galbally, I. E., Gilge, S., Horowitz, L., Jensen, N. R., Lamarque, J.-F., Naik, V., Oltmans, S. J., Schwab, J., Shindell, D. T., Thompson, A. M., Thouret, V., Wang, Y., and Zbinden, R. M.: Global distribution and trends of tropospheric ozone: An observation-based review, Elementa: Science of the Anthropocene, 2, 000 029, doi:10.12952/journal.elementa.000029, 2014.

Crowley, J. N., Ammann, M., Cox, R. A., Hynes, R. G., Jenkin, M. E., Mellouki, A., Rossi, M. J., Troe, J., and Wallington, T. J.: Evaluated kinetic and photochemical data for atmospheric chemistry: Volume V -heterogeneous reactions on solid substrates, Atmospheric Chemistry and Physics, 10, 9059–9223, doi:10.5194/acp-10-9059-2010, 2010.

Crutzen, P. J.: The Role of NO and NO_2 in the Chemistry of the Troposphere and Stratosphere, Annual Review of Earth and Planetary Sciences, 7, 443–472, doi:10.1146/annurev.ea.07.050179.002303, 1979.

Dalsøren, S. B. and Isaksen, I. S. A.: CTM study of changes in tropospheric hydroxyl distribution 1990–2001 and its impact on methane, Geophysical Research Letters, 33, L23 811, doi:10.1029/2006GL027295, 2006.

Damian, V., Sandu, A., Damian, M., Potra, F., and Carmichael, G. R.: The kinetic preprocessor KPP-a software environment for solving chemical kinetics, Computers & Chemical Engineering, 26, 1567–1579, doi:10.1016/S0098-1354(02)00128-X, 2002.

Dari-Salisburgo, C., Di Carlo, P., Giammaria, F., Kajii, Y., and D'Altorio, A.: Laser induced fluorescence instrument for NO_2 measurements: Observations at a central Italy background site, Atmospheric Environment, 43, 970–977, doi:10.1016/j.atmosenv.2008.10.037, 2009.

Day, D. A., Wooldridge, P. J., Dillon, M. B., Thornton, J. A., and Cohen, R. C.: A thermal dissociation laser-induced fluorescence instrument for in situ detection of NO_2, peroxy nitrates, alkyl nitrates, and HNO_3, Journal of Geophysical Research, 107, ACH 4–1–ACH 4–14, doi:10.1029/2001JD000779, 2002.

Del Negro, L. A., Fahey, D. W., Gao, R. S., Donnelly, S. G., Keim, E. R., Neuman, J. A., Cohen, R. C., Perkins, K. K., Koch, L. C., Salawitch, R. J., Lloyd, S. A., Proffitt, M. H., Margitan, J. J., Stimpfle, R. M., Bonne, G. P., Voss, P. B., Wennberg, P. O., McElroy, C. T., Swartz, W. H., Kusterer, T. L., Anderson, D. E., Lait, L. R., and Bui, T. P.: Comparison of modeled and observed values of NO_2 and JNO_2 during the Photochemistry of Ozone Loss in the Arctic Region in Summer (POLARIS) mission, Journal of Geophyscial Research, 104, 26 687–26 703, doi:10.1029/1999JD900246, 1999.

Dentener, F. J. and Crutzen, P. J.: Reaction of N_2O_5 on tropospheric aerosols: Impact on the global distributions of NO_x, O_3, and OH, Journal of Geophysical Research, 94, 7149–7163, doi:10.1029/92JD02979, 1993.

Di Carlo, P., Aruffo, E., Busilacchio, M., Giammaria, F., Dari-Salisburgo, C., Biancofiore, F., Visconti, G., Lee, J., Moller, S., Reeves, C. E., Bauguitte, S., Forster, G., Jones, R. L., and Ouyang, B.: Aircraft based four-channel thermal dissociation laser induced fluorescence instrument for simultaneous measurements of NO_2, total peroxy nitrate, total alkyl nitrate, and HNO_3, Atmospheric Measurement Techniques, 6, 971–980, doi:10.5194/amt-6-971-2013, 2013.

Dickerson, R. R., Rhoads, K. P., Carsey, T. P., Oltmans, S. J., Burrows, J. P., and Crutzen, P. J.: Ozone in the remote marine boundary layer: A possible role for halogens, Journal of Geophyscial Research, 104, 21,385–21,395, doi:10.1029/1999JD900023, 1999.

Dooly, G., Fitzpatrick, C., and Lewis, E.: Deep UV based DOAS system for the monitoring of nitric oxide using ratiometric separation techniques, Sensors and Actuators B: Chemical, 134, 317 – 323, doi:10.1016/j.snb.2008.05.011, 2008.

Drummond, J. W., Volz, A., and Ehhalt, D. H.: An optimized chemiluminescence detector for tropospheric NO measurements, Journal of Atmospheric Chemistry, 2, 287–306, doi:10.1007/BF00051078, 1985.

Dunlea, E. J., Herndon, S. C., Nelson, D. D., Volkamer, R. M., San Martini, F., Sheehy, P. M., Zahniser, M. S., Shorter, J. H., Wormhoudt, J. C., Lamb, B. K., Allwine, E. J., Gaffney, J. S., Marley, N. A., Grutter, M., Marquez, C., Blanco, S., Cardenas, B., Retama, A., Ramos Villegas, C. R., Kolb, C. E., Molina, L. T., and Molina, M. J.: Evaluation of nitrogen dioxide chemiluminescence monitors in a polluted urban environment, Atmospheric Chemistry and Physics, 7, 2691–2704, doi:10.5194/acp-7-2691-2007, 2007.

Elshorbany, Y. F., Kurtenbach, R., Wiesen, P., Lissi, E., Rubio, M., Villena, G., Gramsch, E., Rickard, A. R., Pilling, M. J., and Kleffmann, J.: Oxidation capacity of the city air of Santiago, Chile, Atmospheric Chemistry and Physics, 9, 2257–2273, doi:10.5194/acp-9-2257-2009, 2009.

Emmerson, K. M. and Evans, M. J.: Comparison of tropospheric gas-phase chemistry schemes for use within global models, Atmospheric Chemistry and Physics, pp. 1831–1845, doi:10.5194/acpd-8-19957-2008, 2009.

Evans, M. J. and Jacob, D. J.: Impact of new laboratory studies of N_2O_5 hydrolysis on global model budgets of tropospheric nitrogen oxides, ozone, and OH, Geophysical Research Letters, 32, L09 813, doi:10.1029/2005GL022469, 2005.

Farman, J. C., Gardiner, B. G., and Shanklin, J. D.: Large losses of total ozone in Antarctica reveal seasonal ClO_x/NO_x interaction, Nature, 315, 207–210, doi:10.1038/315207a0, 1985.

Febo, A., Perrino, C., and Cortiello, M.: A denuder technique for the measurement of nitrous acid in urban atmospheres, Atmospheric Environment. Part A. General Topics, 27, 1721–1728, doi:10.1016/0960-1686(93)90235-Q, 1993.

Febo, A., Perrino, C., Gherardi, M., and Sparapani, R.: Evaluation of a High-Purity and High-Stability Continuous Generation System for Nitrous Acid, Environmental Science & Technology, 29, 2390–2395, doi:10.1021/es00009a035, 1995.

Febo, A., Perrino, C., and Allegrini, I.: Measurement of Nitrous Acid in Milan, Italy, By Doas and Diffusion Denuders, Atmospheric Environment, 30, 3599–3609, doi:10.1016/1352-2310(96)00069-6, 1996.

Fehsenfeld, F. C., Dickerson, R. R., Hobler, G., Luke, W. T., Nunnermacker, L. J., Roberts, J. M., Curran, C. M., Eubank, C. S., Fahey, D. W., Mindplay, P. C., and Pickering, K. E.: A Ground-Based Intercomparison of NO, NO_x, and NO_y Measurement Techniques, Journal of Geophysical Research, 92, 710–722, doi:10.1029/JD092iD12p14710, 1987.

Fehsenfeld, F. C., Drummond, J. W., Roychowdhury, U. K., Galvin, P. J., Williams, E. J., Burr, M. P., Parrish, D. D., Hobler, G., Langford, A. O., Calvert, J. G., Ridley, B. A., Heikes, B. G., Kok, G. L., Shetier, J. D., Walega, J. G., Elsworth, C. M.,

and Mohnen, V. A.: Intercomparison of NO_2 Measurement Techniques, Journal of Geophysical Research, 95, 3579–3597, doi:10.1029/JD095iD04p03579, 1990.

Finlayson-Pitts, B. J., Wingen, L. M., Sumner, A. L., Syomin, D., and Ramazan, K. A.: The heterogeneous hydrolysis of NO_2 in laboratory systems and in outdoor and indoor atmospheres: An integrated mechanism, Physical Chemistry Chemical Physics, 5, 223–242, doi:10.1039/b208564j, 2003.

Fischer, E. V., Jacob, D. J., Yantosca, R. M., Sulprizio, M. P., Millet, D. B., Mao, J., Paulot, F., Singh, H. B., Roiger, A.-E., Ries, L., Talbot, R., Dzepina, K., and Pandey Deolal, S.: Atmospheric peroxyacetyl nitrate (PAN): a global budget and source attribution, Atmospheric Chemistry and Physics, 14, 2679–2698, doi:10.5194/acp-14-2679-2014, 2014.

Fischer, G. and Nwankwoala, A. U.: A spectroscopic study of the thermal decomposition of peroxyacetyl nitrate (PAN), Atmospheric Environment, 29, 3277–3280, doi:10.1016/1352-2310(95)00252-T, 1995.

Fisher, J. A., Jacob, D. J., Travis, K. R., Kim, P. S., Marais, E. A., Chan Miller, C., Yu, K., Zhu, L., Yantosca, R. M., Sulprizio, M. P., Mao, J., Wennberg, P. O., Crounse, J. D., Teng, A. P., Nguyen, T. B., St. Clair, J. M., Cohen, R. C., Romer, P., Nault, B. A., Wooldridge, P. J., Jimenez, J. L., Campuzano-Jost, P., Day, D. A., Hu, W., Shepson, P. B., Xiong, F., Blake, D. R., Goldstein, A. H., Misztal, P. K., Hanisco, T. F., Wolfe, G. M., Ryerson, T. B., Wisthaler, A., and Mikoviny, T.: Organic nitrate chemistry and its implications for nitrogen budgets in an isoprene- and monoterpene-rich atmosphere: constraints from aircraft (SEAC^{4}RS) and ground-based (SOAS) observations in the Southeast US, Atmospheric Chemistry and Physics, 16, 5969–5991, doi:10.5194/acp-16-5969-2016, 2016.

Flocke, F. M., Weinheimer, A. J., Swanson, A. L., Roberts, J. M., Schmitt, R., and Shertz, S.: On the measurement of PANs by gas chromatography and electron capture detection, Journal of Atmospheric Chemistry, 52, 19–43, doi:10.1007/s10874-005-6772-0, 2005.

Fomba, K. W., Müller, K., Van Pinxteren, D., Poulain, L., Van Pinxteren, M., and Herrmann, H.: Long-term chemical characterization of tropical and marine aerosols at the Cape Verde Atmospheric Observatory (CVAO) from 2007 to 2011, Atmospheric Chemistry and Physics, 14, 8883–8904, doi:10.5194/acp-14-8883-2014, 2014.

Fontijn, A., Sabadell, A. J., and Ronco, R. J.: Homogeneous chemiluminescent measurement of nitric oxide with ozone. Implications for continuous selective monitoring of gaseous air pollutants, Analytical chemistry, 42, 575–579, doi:10.1021/ac60288a034, 1970.

Frey, M. M., Brough, N., France, J. L., Anderson, P. S., Traulle, O., King, M. D., Jones, A. E., Wolff, E. W., and Savarino, J.: The diurnal variability of atmospheric nitrogen oxides (NO and NO_2) above the Antarctic Plateau driven by atmospheric stability and snow emissions, Atmospheric Chemistry and Physics, 13, 3045–3062, doi:10.5194/acp-13-3045-2013, 2013.

Frey, M. M., Roscoe, H. K., Kukui, A., Savarino, J., France, J. L., King, M. D., Legrand, M., and Preunkert, S.: Atmospheric nitrogen oxides (NO and NO_2) at Dome C, East Antarctica, during the OPALE campaign, Atmospheric Chemistry and Physics, 15, 7859–7875, doi:10.5194/acp-15-7859-2015, 2015.

Fuchs, H., Dub, W. P., Lerner, B. M., Wagner, N. L., Williams, E. J., and Brown, S. S.: A Sensitive and Versatile Detector for Atmospheric NO_2 and NO_x Based on Blue Diode Laser Cavity Ring-Down Spectroscopy, Environmental Science & Technology, 43, 7831–7836, doi:10.1021/es902067h, pMID: 19921901, 2009.

Gao, R. S., Keim, E. R., Woodbridge, E. L., Ciciora, S. J., Proffitt, M. H., Thompson, T. L., Mclaughlin, R. J., and Fahey, D. W.: New photolysis system for NO_2 measurements in the lower stratosphere, Journal of Geophysical Research, 99, 673–681, doi:10.1029/94JD01521, 1994.

Gardner, E. P., Sperry, P. D., and Calvert, J. G.: Primary quantum yields of NO_2 photodissociation, Journal of Geophysical Research, 92, 6642–6652, doi:10.1029/JD092iD06p06642, 1987.

Geyer, A., Alicke, B., Konrad, S., Schmitz, T., Stutz, J., and Platt, U.: Chemistry and oxidation capacity of the nitrate radical in the continental boundary layer near Berlin, Journal of Geophysical Research: Atmospheres, 106, 8013–8025, doi:10.1029/2000jd900681, 2001.

Gligorovski, S.: Nitrous acid (HONO): An emerging indoor pollutant, Journal of Photochemistry and Photobiology A: Chemistry, 314, 1–5, doi:10.1016/j.jphotochem.2015.06.008, 2016.

Glowacki, D. R., Goddard, A., Hemavibool, K., Malkin, T. L., Commane, R., Anderson, F., Bloss, W. J., Heard, D. E., Ingham, T., Pilling, M. J., and Seakins, P. W.: Design of and initial results from a Highly Instrumented Reactor for Atmospheric Chemistry (HIRAC), Atmospheric Chemistry and Physics, 7, 5371–5390, doi:10.5194/acp-7-5371-2007, 2007a.

Glowacki, D. R., Goddard, A., and Seakins, P. W.: Design and performance of a throughput-matched, zero-geometric-loss, modified three objective multipass matrix system for FT-IR spectrometry, Applied Optics, 46, 7872, doi:10.1364/AO.46.007872, 2007b.

Griffin, R. J., Beckman, P. J., Talbot, R. W., Sive, B. C., and Varner, R. K.: Deviations from ozone photostationary state during the International Consortium for Atmospheric Research on Transport and Transformation 2004 campaign: Use of measurements and photochemical modeling to assess potential causes, Journal of Geophyscial Research, 112, 1–16, doi:10.1029/2006JD007604, 2007.

Grosjean, D. and Harrison, J.: Response of chemiluminescence NO_x analyzers and ultraviolet ozone analyzers to organic air pollutants, Environmental Science & Technology, 19, 862–865, doi:10.1021/es00139a016, 1985.

Gutzwiller, L., Arens, F., Baltensperger, U., Gäggeler, H. W., and Ammann, M.: Significance of semivolatile diesel exhaust organics for secondary HONO formation, Environmental Science & Technology, 36, 677–682, doi:10.1021/es015673b, 2002.

Handley, S. R., Clifford, D., and Donaldson, D. J.: Photochemical Loss of Nitric Acid on Organic Films: a Possible Recycling Mechanism for NO_x, Environmental Science & Technology, 41, 3898–3903, doi:10.1021/es062044z, 2007.

Heland, J., Kleffmann, J., Kurtenbach, R., and Wiesen, P.: A new instrument to measure gaseous nitrous acid (HONO) in the atmosphere, Environmental Science & Technology, 35, 3207–3212, doi:10.1021/es000303t, 2001.

Hendrick, F., Clémer, K., Wang, P., De Mazière, M., Fayt, C., Gielen, C., Hermans, C., Ma, J. Z., Pinardi, G., Stavrakou, T., Vlemmix, T., and Van Roozendael, M.: Four years of ground-based MAX-DOAS observations of HONO and NO_2 in the Beijing area, Atmospheric Chemistry and Physics, 14, 765–781, doi:10.5194/acp-14-765-2014, 2014.

Hoell, J. M., Gregory, G. L., McDougal, D. S., Carroll, M. A., McFarland, M., Ridley, B. A., Davis, D. D., Bradshaw, J., Rodgers, M. O., and Torres, A. L.: An intercomparison of nitric oxide measurement techniques, Journal of Geophysical Research: Atmospheres, 90, 12 843–12 851, doi:10.1029/JD090iD07p12843, 1985.

Hoell, J. M., Gregory, G. L., McDougal, D. S., Torres, A. L., Davis, D. D., Bradshaw, J., Rodgers, M. O., Ridley, B. A., and Carroll, M. A.: Airborne intercomparison of nitric oxide measurement techniques, Journal of Geophysical Research: Atmospheres, 92, 1995–2008, doi:10.1029/JD092iD02p01995, 1987.

Hollaway, M. J., Arnold, S. R., Challinor, A. J., and Emberson, L. D.: Intercontinental trans-boundary contributions to ozone-induced crop yield losses in the Northern Hemisphere, Biogeosciences, 9, 271–292, doi:10.5194/bg-9-271-2012, 2012.

Hosaynali Beygi, Z., Fischer, H., Harder, H. D., Martinez, M., Sander, R., Williams, J., Brookes, D. M., Monks, P. S., and Lelieveld, J.: Oxidation photochemistry in the Southern Atlantic boundary layer: Unexpected deviations of photochemical steady state, Atmospheric Chemistry and Physics, 11, 8497–8513, doi:10.5194/acp-11-8497-2011, 2011.

Huntrieser, H., Schlager, H., Roiger, A., Lichtenstern, M., Schumann, U., Kurz, C., Brunner, D., Schwierz, C., Richter, A., and Stohl, A.: Lightning-produced NO_x over Brazil during TROCCINOX: airborne measurements in tropical and subtropical thunderstorms and the importance of mesoscale convective systems, Atmospheric Chemistry and Physics, 7, 2987–3013, doi:10.5194/acp-7-2987-2007, 2007.

Ianniello, A., Beine, H. J., Landis, M. S., Stevens, R. K., Esposito, G., Amoroso, A., and Allegrini, I.: Comparing field performances of denuder techniques in the high Arctic, Atmospheric Environment, 41, 1604–1615, doi:10.1016/j.atmosenv.2006.10.040, 2007.

Isaksen, I. S. A. and Hov, Ø.: Calculation of trends in the tropospheric concentration of O_3, OH, CO, CH_4 and NO_x, Tellus B, 39B, 271–285, doi:10.1111/j.1600-0889.1987.tb00099.x, 1987.

Jacobi, H.-W. W., Weller, R., Bluszcz, T., and Schrems, O.: Latitudinal distribution of peroxyacetyl nitrate (PAN) over the Atlantic Ocean, Journal of Geophysical Research, 104, 26 901–26 912, doi:10.1029/1999JD900462, 1999.

Jaeglé, L., Jacob, D. J., Brune, W. H., Tan, D., Faloona, I. C., Weinheimer, A. J., Ridley, B. A., Campos, T. L., and Sachse, G. W.: Sources of HO_x and production of ozone in the upper troposphere over the United States, Geophysical Research Letters, 25, 1709–1712, doi:10.1029/98GL00041, 1998.

Jaeglé, L., Steinberger, L., Martin, R. V., and Chance, K.: Global partitioning of NO_x sources using satellite observations: Relative roles of fossil fuel combustion, biomass burning and soil emissions, Faraday Discussions, 130, 407, doi:10.1039/b502128f, 2005.

Jenkin, M. E., Saunders, S. M., and Pilling, M. J.: The tropospheric degradation of volatile organic compounds: a protocol for mechanism development, Atmospheric Environment, 31, 81–104, doi:10.1016/S1352-2310(96)00105-7, 1997.

Jenkin, M. E., Saunders, S. M., Wagner, V., and Pilling, M. J.: Protocol for the development of the Master Chemical Mechanism, MCM v3 (Part B): tropospheric degradation of aromatic volatile organic compounds, Atmospheric Chemistry and Physics, 3, 181–193, doi:10.5194/acp-3-181-2003, 2003.

Jenkin, M. E., Young, J. C., and Rickard, A. R.: The MCM v3.3.1 degradation scheme for isoprene, Atmospheric Chemistry and Physics, 15, 11 433–11 459, doi:10.5194/acp-15-11433-2015, 2015.

Kanaya, Y., Cao, R., Akimoto, H., Fukuda, M., Komazaki, Y., Yokouchi, Y., Koike, M., Tanimoto, H., Takegawa, N., and Kondo, Y.: Urban photochemistry in central Tokyo: 1. Observed and modeled OH and HO_2 radical concentrations during the winter and summer of 2004, Journal of Geophysical Research, 112, D21 312, doi:10.1029/2007JD008670, 2007a.

Kanaya, Y., Tanimoto, H., Matsumoto, J., Furutani, H., Hashimoto, S., Komazaki, Y., Tanaka, S., Yokouchi, Y., Kato, S., Kajii, Y., and Akimoto, H.: Diurnal variations in H_2O_2, O_3, PAN, HNO_3 and aldehyde concentrations and NO/NO_2 ratios at Rishiri Island, Japan: Potential influence from iodine chemistry, Science of The Total Environment, 376, 185–197, doi:10.1016/j.scitotenv.2007.01.073, 2007b.

Kebabian, P. L. and Freedman, A.: System and method for trace species detection using cavity attenuated phase shift spectroscopy with an incoherent light source, US 7301639 B1, United States, USTPO, 2007.

Kebabian, P. L., Herndon, S. C., and Freedman, A.: Detection of Nitrogen Dioxide by Cavity Attenuated Phase Shift Spectroscopy, Analytical Chemistry, 77, 724–728, doi:10.1021/ac048715y, 2005.

Kebabian, P. L., Wood, E. C., Herndon, S. C., and Freedman, A.: A Practical Alternative to Chemiluminescence-Based Detection of Nitrogen Dioxide: Cavity Attenuated Phase Shift Spectroscopy, Environmental Science & Technology, 42, 6040–6045, doi:10.1021/es703204j, 2008.

Keene, W. C., Long, M. S., Pszenny, A. A. P., Sander, R., Maben, J. R., Wall, A. J., O'Halloran, T. L., Kerkweg, A., Fischer, E. V., and Schrems, O.: Latitudinal variation in the multiphase chemical processing of inorganic halogens and related species over the eastern North and South Atlantic Oceans, Atmospheric Chemistry and Physics, 9, 11 889–11 950, doi:10.5194/acpd-9-11889-2009, 2009.

Kelly, T. J., Stedman, D. H., Ritter, J. A., and Harvey, R. B.: Measurements of oxides of nitrogen and nitric acid in clean air, Journal of Geophysical Research, 85, 7417–7425, doi:10.1029/JC085iC12p07417, 1980.

Kim, M. J., Farmer, D. K., and Bertram, T. H.: A controlling role for the air-sea interface in the chemical processing of reactive nitrogen in the coastal marine boundary layer, Proceedings of the National Academy of Sciences, 111, 1–6, doi:10.1073/pnas.1318694111, 2014a.

Kim, S., VandenBoer, T. C., Young, C. J., Riedel, T. P., Thornton, J. A., Swarthout, B., Sive, B., Lerner, B. M., Gilman, J. B., Warneke, C., Roberts, J. M., Guenther, A., Wagner, N. L., Dubé, W. P., Williams, E. J., and Brown, S. S.: The primary and recyling sources of OH during the NACHTT-2011 campaign: HONO as an important OH primary source in the wintertime, Journal of Geophyscial Research, 119, 6886–6896, doi:10.1002/2013JD019784, 2014b.

Kleffmann, J.: Daytime sources of nitrous acid (HONO) in the atmospheric boundary layer, ChemPhysChem, 8, 1137–1144, doi:10.1002/cphc.200700016, 2007.

Kleffmann, J. and Wiesen, P.: Technical note: Quantification of interferences of wet chemical HONO LOPAP measurements under simulated polar conditions, Atmospheric Chemistry and Physics, 8, 6813–6822, doi:10.5194/acp-8-6813-2008, 2008.

Kleffmann, J., Lörzer, J., Wiesen, P., Kern, C., Trick, S., Volkamer, R., Rodenas, M., and Wirtz, K.: Intercomparison of the DOAS and LOPAP techniques for the detection of nitrous acid (HONO), Atmospheric Environment, 40, 3640–3652, doi:10.1016/j.atmosenv.2006.03.027, 2006.

Kleffmann, J., Villena Tapia, G., Bejan, I., Kurtenbach, R., and Wiesen, P.: Disposal of Dangerous Chemicals in Urban Areas and Mega Cities, vol. 120 of *NATO Science for Peace and Security Series C: Environmental Security*, Springer Netherlands, doi:10.1007/978-94-007-5034-0, 2013.

Kleindienst, T. E.: Recent developments in the chemistry and biology of peroxyacetyl nitrate, Research on Chemical Intermediates, 20, 335–384, doi:10.1163/156856794X00379, 1994.

Kley, D., Drummond, J. W., McFarland, M., and Liu, S. C.: Tropospheric profiles of NO_x, Journal of Geophysical Research, 86, 3153–3161, doi:10.1029/JC086iC04p03153, 1981.

Koepke, P., Garhammer, M., Hess, M., and Roeth, E. P.: NO_2 photolysis frequencies in street canyons, Atmospheric Chemistry and Physics, 10, 7457–7466, doi:10.5194/acp-10-7457-2010, 2010.

Lammel, G. and Cape, J. N.: Nitrous acid and nitrite in the atmosphere, Chemical Society Reviews, 25, 361, doi:10.1039/cs9962500361, 1996.

Lee, B. H., Santoni, G. W., Wood, E. C., Herndon, S. C., Miake-Lye, R. C., Zahniser, M. S., Wofsy, S. C., and Munger, J. W.: Measurements of nitrous acid in commercial aircraft exhaust at the alternative aviation fuel experiment, Environmental Science & Technology, 45, 7648–7654, doi:10.1021/es200921t, 2011a.

Lee, B. H., Wood, E. C., Zahniser, M. S., McManus, J. B., Nelson, D. D., Herndon, S. C., Santoni, G. W., Wofsy, S. C., and Munger, J. W.: Simultaneous measurements of atmospheric HONO and NO_2 via absorption spectroscopy using tunable mid-infrared continuous-wave quantum cascade lasers, Applied Physics B, 102, 417–423, doi:10.1007/s00340-010-4266-5, 2011b.

Lee, G., Choi, H.-S., Lee, T., Choi, J., Park, J. S., and Ahn, J. Y.: Variations of regional background peroxyacetyl nitrate in marine boundary layer

over Baengyeong Island, South Korea, Atmospheric Environment, 61, 533–541, doi:10.1016/j.atmosenv.2012.07.075, 2012.

Lee, J. D., Moller, S. J., Read, K. A., Lewis, A. C., Mendes, L., and Carpenter, L. J.: Year-round measurements of nitrogen oxides and ozone in the tropical North Atlantic marine boundary layer, Journal of Geophysical Research, 114, D21 302, doi:10.1029/2009JD011878, 2009.

Lee, J. D., Whalley, L. K., Heard, D. E., Stone, D., Dunmore, R. E., Hamilton, J. F., Young, D. E., Allan, J. D., Laufs, S., and Kleffmann, J.: Detailed budget analysis of HONO in central London reveals a missing daytime source, Atmospheric Chemistry and Physics, 16, 2747–2764, doi:10.5194/acp-16-2747-2016, 2016.

Leighton, P. A.: Photochemistry of air pollution, Physical chemistry, Academic Press, 1961.

Lelieveld, J., Dentener, F. J., Peters, W., and Krol, M. C.: On the role of hydroxyl radicals in the self-cleansing capacity of the troposphere, Atmospheric Chemistry and Physics, 4, 2337–2344, doi:10.5194/acp-4-2337-2004, 2004.

Levy, H.: Normal Atmosphere: Large Radical and Formaldehyde Concentrations Predicted, Science, 173, 141–143, doi:10.1126/science.173.3992.141, 1971.

Levy, H.: Photochemistry of the lower troposphere, Planetary and Space Science, 20, 919–935, doi:10.1016/0032-0633(72)90177-8, 1972.

Levy, H.: Photochemistry of minor constituents in the troposphere, Planetary and Space Science, 21, 575–591, doi:10.1016/0032-0633(73)90071-8, 1973.

Levy, M., Zhang, R., Zheng, J., Zhang, A. L., Xu, W., Gomez-Hernandez, M., Wang, Y., and Olaguer, E.: Measurements of nitrous acid (HONO) using ion drift-chemical ionization mass spectrometry during the 2009 SHARP field campaign, Atmospheric Environment, 94, 231–240, doi:10.1016/j.atmosenv.2014.05.024, 2014.

Lewis, A. C., Evans, M. J., Methven, J., Watson, N., Lee, J. D., Hopkins, J. R., Purvis, R. M., Arnold, S. R., McQuaid, J. B., Whalley, L. K., Pilling, M. J., Heard, D. E., Monks, P. S., Parker, A. E., Reeves, C. E., Oram, D. E., Mills, G., Bandy, B. J., Stewart, D., Coe, H., Williams, P., and Crosier, J.: Chemical composition observed

over the mid-Atlantic and the detection of pollution signatures far from source regions, Journal of Geophysical Research, 112, D10S39, doi:10.1029/2006JD007584, 2007.

Li, S., Matthews, J., and Sinha, A.: Atmospheric Hydroxyl Radical Production from Electronically Excited NO_2 and H_2O, Science, 319, 1657–1660, doi:10.1126/science.1151443, 2008.

Li, X., Rohrer, F., Hofzumahaus, A., Brauers, T., Haseler, R., Bohn, B., Broch, S., Fuchs, H., Gomm, S., Holland, F., Jager, J., Kaiser, J., Keutsch, F. N., Lohse, I., Lu, K., Tillmann, R., Wegener, R., Wolfe, G. M., Mentel, T. F., Kiendler-Scharr, A., and Wahner, A.: Missing Gas-Phase Source of HONO Inferred from Zeppelin Measurements in the Troposphere, Science, 344, 292–296, doi:10.1126/science.1248999, 2014.

Logan, J. A., Prather, M. J., Wofsy, S. C., and McElroy, M. B.: Tropospheric chemistry: A global perspective, Journal of Geophysical Research, 86, 7210, doi:10.1029/JC086iC08p07210, 1981.

Madronich, S.: UV radiation in the natural and perturbed atmosphere, in: UV-B radiation and ozone depletion: effects on humans, animals, plants, microorganisms, and materials, edited by Tevini, M., chap. UV radiation in the natural and perturbed atmosphere, pp. 17–61, Lewis Publishers, Boca Raton, FL, USA, 1993.

Mahajan, A. S., Plane, J. M. C., Oetjen, H., Mendes, L., Saunders, R. W., Saiz-Lopez, A., Jones, C. E., Carpenter, L. J., and McFiggans, G. B.: Measurement and modelling of tropospheric reactive halogen species over the tropical Atlantic Ocean, Atmospheric Chemistry and Physics, 10, 4611–4624, doi:10.5194/acp-10-4611-2010, 2010a.

Mahajan, A. S., Whalley, L. K., Kozlova, E., Oetjen, H., Mendez, L., Furneaux, K. L., Goddard, A., Heard, D. E., Plane, J. M. C., and Saiz-Lopez, A.: DOAS observations of formaldehyde and its impact on the HO_x balance in the tropical Atlantic marine boundary layer, Journal of Atmospheric Chemistry, 66, 167–178, doi:10.1007/s10874-011-9200-7, 2010b.

Mannschreck, K., Gilge, S., Plass-Duelmer, C., Fricke, W., and Berresheim, H.: Assessment of the applicability of NO-NO_2-O_3 photostationary state to long-term measurements at the Hohenpeissenberg GAW Station, Germany, Atmospheric Chemistry and Physics, 4, 1265–1277, doi:10.5194/acp-4-1265-2004, 2004.

Markovic, M. Z., VandenBoer, T. C., and Murphy, J. G.: Characterization and optimization of an online system for the simultaneous measurement of atmospheric water-soluble constituents in the gas and particle phases, Journal of Environmental Monitoring, 14, 1872, doi:10.1039/c2em00004k, 2012.

Matsumi, Y. and Kawasaki, M.: Photolysis of Atmospheric Ozone in the Ultraviolet Region, Chemical Reviews, 103, 4767–4782, doi:10.1021/cr0205255, 2003.

Matsumoto, J. and Kajii, Y.: Improved analyzer for nitrogen dioxide by laser-induced fluorescence technique, Atmospheric Environment, 37, 4847–4851, doi:10.1016/j.atmosenv.2003.08.023, 2003.

Matsumoto, J., Hirokawa, J., Akimoto, H., and Kajii, Y.: Direct measurement of NO_2 in the marine atmosphere by laser-induced fluorescence technique, Atmospheric Environment, 35, 2803–2814, doi:10.1016/S1352-2310(01)00078-4, 2001.

Mauzerall, D. L., Sultan, B., Kim, N., and Bradford, D. F.: NO emissions from large point sources: variability in ozone production, resulting health damages and economic costs, Atmospheric Environment, 39, 2851–2866, doi:10.1016/j.atmosenv.2004.12.041, 2005.

Mazely, T. L., Friedl, R. R., and Sander, S. P.: Production of NO_2 from Photolysis of Peroxyacetyl Nitrate, The Journal of Physical Chemistry, 99, 8162–8169, doi:10.1021/j100020a044, 1995.

McClenny, W. A., Williams, E. J., Cohen, R. C., and Stutz, J.: Preparing to Measure the Effects of the NO_x SIP Call— Methods for Ambient Air Monitoring of NO, NO_2, NO_y, and Individual NO_z Species, Journal of the Air & Waste Management Association, 52, 542–562, doi:10.1080/10473289.2002.10470801, 2002.

Meyrahn, H., Helas, G., and Warneck, P.: Gas chromatographic determination of peroxyacetyl nitrate: Two convenient calibration techniques, Journal of Atmospheric Chemistry, 5, 405–415, doi:10.1007/BF00113903, 1987.

Mills, G. P., Sturges, W. T., Salmon, R. A., Bauguitte, S. J.-B., Read, K. A., and Bandy, B. J.: Seasonal variation of peroxyacetylnitrate (PAN) in coastal Antarctica measured with a new instrument for the detection of sub-part per trillion mixing ratios of PAN, Atmospheric Chemistry and Physics, 7, 4589–4599, doi:10.5194/acp-7-4589-2007, 2007.

Mogili, P. K., Kleiber, P. D., Young, M. A., and Grassian, V. H.: NO_5 hydrolysis on the components of mineral dust and sea salt aerosol: Comparison study in an environmental aerosol reaction chamber, Atmospheric Environment, 40, 7401–7408, doi:10.1016/j.atmosenv.2006.06.048, 2006.

Monks, P. S., Carpenter, L. J., Penkett, S. A., Ayers, G. P., Gillett, R. W., Galbally, I. E., and Meyer, C. P.: Fundamental ozone photochemistry in the remote marine boundary layer: The SOAPEX experiment, measurement and theory, Atmospheric Environment, 32, 3647–3664, doi:10.1016/S1352-2310(98)00084-3, 1998.

Moore, R. M. and Blough, N. V.: A marine source of methyl nitrate, Geophysical Research Letters, 29, 27–1–27–4, doi:10.1029/2002GL014989, 2002.

Moxim, W. J., Levy, H., and Kasibhatla, P. S.: Simulated global tropospheric PAN: Its transport and impact on NO_x, Journal of Geophyscial Research, 101, 12 621–12 638, doi:10.1029/96JD00338, 1996.

Nakamura, K., Kondo, Y., Chen, G., Crawford, J. H., Takegawa, N., Koike, M., Kita, K., Miyazaki, Y., Shetter, R. E., Lefer, B. L., Avery, M., and Matsumoto, J.: Measurement of NO_2 by the photolysis conversion technique during the Transport and Chemical Evolution Over the Pacific (TRACE-P) campaign, Journal of Geophyscial Research, 108, ACH 1 – ACH 11, doi:10.1029/2003JD003712, 2003.

Nault, B. A., Garland, C., Pusede, S. E., Wooldridge, P. J., Ullmann, K., Hall, S. R., and Cohen, R. C.: Measurements of $CH_3O_2NO_2$ in the upper troposphere, Atmospheric Measurement Techniques, 8, 987–997, doi:10.5194/amt-8-987-2015, 2015.

Ndour, M., Conchon, P., D'Anna, B., Ka, O., and George, C.: Photochemistry of mineral dust surface as a potential atmospheric renoxification process, Geophysical Research Letters, 36, L05 816, doi:10.1029/2008GL036662, 2009.

Neu, J. L., Lawler, M. J., Prather, M. J., and Saltzman, E. S.: Oceanic alkyl nitrates as a natural source of tropospheric ozone, Geophysical Research Letters, 35, L13 814, doi:10.1029/2008GL034189, 2008.

Orlando, J. J. and Tyndall, G. S.: Rate Coefficients for the Thermal Decomposition of $BrONO_2$ and the Heat of Formation of $BrONO_2$, The Journal of Physical Chemistry, 100, 19 398–19 405, doi:10.1021/jp9620274, 1996.

Osthoff, H. D., Brown, S. S., Ryerson, T. B., Fortin, T. J., Lerner, B. M., Williams, E. J., Pettersson, A., Baynard, T., Dubé, W. P., Ciciora, S. J., and Ravishankara, A. R.: Measurement of atmospheric NO_2 by pulsed cavity ring-down spectroscopy, Journal of Geophysical Research, 111, D12 305, doi:10.1029/2005JD006942, 2006.

Oswald, R., Behrendt, T., Ermel, M., Wu, D., Su, H., Cheng, Y., Breuninger, C., Moravek, A., Mougin, E., Delon, C., Loubet, B., Pommerening-Roser, A., Sorgel, M., Poschl, U., Hoffmann, T., Andreae, M. O., Meixner, F. X., and Trebs, I.: HONO Emissions from Soil Bacteria as a Major Source of Atmospheric Reactive Nitrogen, Science, 341, 1233–1235, doi:10.1126/science.1242266, 2013.

Pandey, S. K., Kim, K. H., Chung, S. Y., Cho, S. J., Kim, M. Y., and Shon, Z. H.: Long-term study of NO_x behavior at urban roadside and background locations in Seoul, Korea, Atmospheric Environment, 42, 607–622, doi:10.1016/j.atmosenv.2007.10.015, 2008.

Penkett, S., Gilge, S., Plass-Duelmer, C., Galbally, I., Brough, N., Bottenheim, J. W., Flocke, F. M., Gerwig, H., Lee, J. D., Milton, M., Roher, F., Ryerson, T. B., Steinbacher, M., Torseth, K., Wielgosz, R., Suda, K., Akimoto, H., and Tarasova, O.: WMO/GAW Expert Workshop on Global Long-term Measurements of Nitrogen Oxides and Recommendations for GAW Nitrogen Oxides Network, Tech. Rep. 195, 2009.

Penkett, S. A., Plane, J. M. C., Comes, F. J., Clemitshaw, K. C., and Coe, H.: The Weybourne Atmospheric Observatory, Journal of Atmospheric Chemistry, 33, 107–110, doi:10.1023/A:1026428102821, 1999.

Perner, D. and Platt, U.: Detection of nitrous acid in the atmosphere by differential optical absorption, Geophysical Research Letters, 6, 917–920, doi:10.1029/gl006i012p00917, 1979.

Peterson, C. and Honrath, R. E.: NO_x and NO_y over the northwestern North Atlantic: Measurements and measurement accuracy, Journal of Geophyscial Research, 104, 11 695–11 707, doi:10.1029/1998JD100088, 1999.

Plane, J. M. C., Joseph, D. M., Allan, B. J., Ashworth, S. H., and Francisco, J. S.: An Experimental and Theoretical Study of the Reactions OIO + NO and OIO + OH, The Journal of Physical Chemistry A, 110, 93–100, doi:10.1021/jp055364y, 2006.

Platt, U.: Modern methods of the measurement of atmospheric trace gases Invited Lecture, Physical Chemistry Chemical Physics, 1, 5409–5415, doi:10.1039/a906810d, 1999.

Pollack, I. B., Lerner, B. M., and Ryerson, T. B.: Evaluation of ultraviolet light-emitting diodes for detection of atmospheric NO_2 by photolysis - chemiluminescence, Journal of Atmospheric Chemistry, 65, 111–125, doi:10.1007/s10874-011-9184-3, 2011.

Pusede, S. E., Gentner, D. R., Wooldridge, P. J., Browne, E. C., Rollins, A. W., Min, K.-E., Russell, A. R., Thomas, J., Zhang, L., Brune, W. H., Henry, S. B., DiGangi, J. P., Keutsch, F. N., Harrold, S. A., Thornton, J. A., Beaver, M. R., St. Clair, J. M., Wennberg, P. O., Sanders, J., Ren, X., VandenBoer, T. C., Markovic, M. Z., Guha, A., Weber, R., Goldstein, A. H., and Cohen, R. C.: On the temperature dependence of organic reactivity, nitrogen oxides, ozone production, and the impact of emission controls in San Joaquin Valley, California, Atmospheric Chemistry and Physics, 14, 3373–3395, doi:10.5194/acp-14-3373-2014, 2014.

Ramazan, K. A., Syomin, D., and Finlayson-Pitts, B. J.: The photochemical production of HONO during the heterogeneous hydrolysis of NO_2, Physical Chemistry Chemical Physics, 6, 3836, doi:10.1039/b402195a, 2004.

Rappenglück, B., Lubertino, G., Alvarez, S., Golovko, J., Czader, B., and Ackermann, L.: Radical precursors and related species from traffic as observed and modeled at an urban highway junction, Journal of the Air & Waste Management Association, 63, 1270–1286, doi:10.1080/10962247.2013.822438, 2013.

Rattigan, O., Lutman, E., Jones, R. L., Cox, R. A., Clemitshaw, K., and Williams, J.: Temperature-dependent absorption cross-sections of gaseous nitric acid and methyl nitrate, Journal of Photochemistry and Photobiology, A: Chemistry, 66, 313–326, doi:10.1016/1010-6030(92)80003-E, 1992.

Read, K. A., Mahajan, A. S., Carpenter, L. J., Evans, M. J., Faria, B. V. E., Heard, D. E., Hopkins, J. R., Lee, J. D., Moller, S. J., Lewis, A. C., Mendes, L., McQuaid, J. B., Oetjen, H., Saiz-Lopez, A., Pilling, M. J., and Plane, J. M. C.: Extensive halogen-mediated ozone destruction over the tropical Atlantic Ocean, Nature, 453, 1232–1235, doi:10.1038/nature07035, 2008.

Read, K. A., Carpenter, L. J., Arnold, S. R., Beale, R., Nightingale, P. D., Hopkins, J. R., Lewis, A. C., Lee, J. D., Mendes, L., and Pickering, S. J.: Multiannual observations

of acetone, methanol, and acetaldehyde in remote tropical atlantic air: implications for atmospheric OVOC budgets and oxidative capacity., Environmental Science & Technology, 46, 11 028–39, doi:10.1021/es302082p, 2012.

Reed, C., Brumby, C. A., Crilley, L. R., Kramer, L. J., Bloss, W. J., Seakins, P. W., Lee, J. D., and Carpenter, L. J.: HONO measurement by differential photolysis, Atmospheric Measurement Techniques, 9, 2483–2495, doi:10.5194/amt-9-2483-2016, 2016a.

Reed, C., Evans, M. J., Di Carlo, P., Lee, J. D., and Carpenter, L. J.: Interferences in photolytic NO_2 measurements: explanation for an apparent missing oxidant?, Atmospheric Chemistry and Physics, 16, 4707–4724, doi:10.5194/acp-16-4707-2016, 2016b.

Reed, C., Evans, M. J., Crilley, L. R., Bloss, W. J., Sherwen, T., Read, K. A., Lee, J. D., and Carpenter, L. J.: Evidence for renoxification in the tropical marine boundary layer, Atmospheric Chemistry and Physics, 17, 4081–4092, doi:10.5194/acp-17-4081-2017, 2017.

Ren, X., Gao, H., Zhou, X., Crounse, J. D., Wennberg, P. O., Browne, E. C., LaFranchi, B. W., Cohen, R. C., McKay, M., Goldstein, A. H., and Mao, J.: Measurement of atmospheric nitrous acid at Blodgett Forest during BEARPEX2007, Atmospheric Chemistry and Physics, 10, 6501, doi:10.5194/acp-10-6283-2010, 2010.

Ren, X., Sanders, J. E., Rajendran, A., Weber, R. J., Goldstein, A. H., Pusede, S. E., Browne, E. C., Min, K. E., and Cohen, R. C.: A relaxed eddy accumulation system for measuring vertical fluxes of nitrous acid, Atmospheric Measurement Techniques, 4, 2093–2103, doi:10.5194/amt-4-2093-2011, 2011.

Ridley, B. A., Carroll, M. A., Torres, A. L., Condon, E. P., Sachse, G. W., Hill, G. F., and Gregory, G. L.: An intercomparison of results from ferrous sulphate and photolytic converter techniques for measurements of NO_x made during the NASA GTE/CITE 1 aircraft program, Journal of Geophysical Research, 93, 15 803–15 811, doi:10.1029/JD093iD12p15803, 1988.

Ridley, D. A., Heald, C. L., and Prospero, J. M.: What controls the recent changes in African mineral dust aerosol across the Atlantic?, Atmospheric Chemistry and Physics, 14, 5735–5747, doi:10.5194/acp-14-5735-2014, 2014.

Riemer, N., Vogel, H., Vogel, B., Schell, B., Ackermann, I., Kessler, C., and Hass, H.: Impact of the heterogeneous hydrolysis of N_2O_5 on Chemistry and Nitrate Aerosol Formation in the Lower Troposphere Under Photosmog Conditions, Journal of Geophysical Research, 108, 1–21, doi:10.1029/2002JD002436, 2003.

Riffault, V., Bedjanian, Y., and Poulet, G.: Kinetic and mechanistic study of the reactions of OH with IBr and HOI, Journal of Photochemistry and Photobiology A: Chemistry, 176, 155 – 161, doi:10.1016/j.jphotochem.2005.09.002, 2005.

Roberts, J. M., Marchewka, M., Bertman, S. B., Sommariva, R., Warneke, C., de Gouw, J., Kuster, W., Goldan, P., Williams, E., Lerner, B. M., Murphy, P., and Fehsenfeld, F. C.: Measurements of PANs during the New England Air Quality Study 2002, Journal of Geophysical Research, 112, D20 306, doi:10.1029/2007JD008667, 2007.

Roberts, J. M., Veres, P., Warneke, C., Neuman, J. A., Washenfelder, R. A., Brown, S. S., Baasandorj, M., Burkholder, J. B., Burling, I. R., Johnson, T. J., Yokelson, R. J., and De Gouw, J.: Measurement of HONO, HNCO, and other inorganic acids by negative-ion proton-transfer chemical-ionization mass spectrometry (NI-PT-CIMS): Application to biomass burning emissions, Atmospheric Measurement Techniques, 3, 981–990, doi:10.5194/amt-3-981-2010, 2010.

Ródenas, M., Muñoz, A., Alacreu, F., Brauers, T., Dorn, H.-P., Kleffmann, J., and Bloss, W.: Assessment of HONO Measurements: The FIONA Campaign at EUPHORE, vol. 120 of *NATO Science for Peace and Security Series C: Environmental Security*, Springer Netherlands, doi:10.1007/978-94-007-5034-0_4, 2013.

Roumelis, N. and Glavas, S.: Thermal decomposition of peroxyacetyl nitrate in the presence of O_2, NO_2 and NO, Monatshefte fur Chemie Chemical Monthly, 123, 63–72, doi:10.1007/BF01045298, 1992.

Ryerson, T. B., Williams, E. J., and Fehsenfeld, F. C.: An efficient photolysis system for fast-response NO_2 measurements, Journal of Geophysical Research, 105, 26,447–26,461, doi:10.1029/2000JD900389, 2000.

Sadanaga, Y., Fukumori, Y., Kobashi, T., Nagata, M., Takenaka, N., and Bandow, H.: Development of a selective light-emitting diode photolytic NO_2 converter for continuously measuring NO_2 in the atmosphere, Analytical Chemistry, 82, 9234–9239, doi:10.1021/ac101703z, 2010.

Sadanaga, Y., Suzuki, K., Yoshimoto, T., and Bandow, H.: Direct measurement system of nitrogen dioxide in the atmosphere using a blue light-emitting diode induced fluorescence technique, Review of Scientific Instruments, 85, 064 101, doi:10.1063/1.4879821, 2014.

Saiz-Lopez, A., Plane, J. M. C., Mahajan, A. S., Anderson, P. S., Bauguitte, S. J.-B., Jones, A. E., Roscoe, H. K., Salmon, R. A., Bloss, W. J., Lee, J. D., and Heard, D. E.: On the vertical distribution of boundary layer halogens over coastal Antarctica: implications for O_3, HO_x, NO_x and the Hg lifetime, Atmospheric Chemistry and Physics, 8, 887–900, doi:10.5194/acp-8-887-2008, 2008.

Saiz-Lopez, A., Plane, J. M. C., Cuevas, C. A., Mahajan, A. S., Lamarque, J.-F., and Kinnison, D. E.: Nighttime atmospheric chemistry of iodine, Atmospheric Chemistry and Physics, 16, 15 593–15 604, doi:10.5194/acp-16-15593-2016, 2016.

Sander, R., Rudich, Y., von Glasow, R., and Crutzen, P. J.: The role of $BrNO_3$ in marine tropospheric chemistry: A model study, Geophysical Research Letters, 26, 2857–2860, doi:10.1029/1999GL900478, 1999.

Sandu, A. and Sander, R.: Technical note: Simulating chemical systems in Fortran90 and Matlab with the Kinetic PreProcessor KPP-2.1, Atmospheric Chemistry and Physics, 6, 187–195, doi:10.5194/acp-6-187-2006, 2006.

Saunders, S. M., Jenkin, M. E., Derwent, R. G., and Pilling, M. J.: Protocol for the development of the Master Chemical Mechanism, MCM v3 (Part A): tropospheric degradation of non-aromatic volatile organic compounds, Atmospheric Chemistry and Physics, 3, 161–180, doi:10.5194/acp-3-161-2003, 2003.

Savarino, J., Morin, S., Erbland, J., Grannec, F., Patey, M. D., Vicars, W., Alexander, B., and Achterberg, E. P.: Isotopic composition of atmospheric nitrate in a tropical marine boundary layer, Proceedings of the National Academy of Sciences, 110, 17 668–17 673, doi:10.1073/pnas.1216639110, 2013.

Scharko, N. K., Berke, A. E., and Raff, J. D.: Release of Nitrous Acid and Nitrogen Dioxide from Nitrate Photolysis in Acidic Aqueous Solutions, Environmental Science & Technology, 48, 11 991–12 001, doi:10.1021/es503088x, 2014.

Schott: Schott UG5 UV-passing filter, DIN BP 318/173, Tech. rep., Schott AG., 1997.

Sherwen, T., Evans, M. J., Carpenter, L. J., Andrews, S. J., Lidster, R. T., Dix, B., Koenig, T. K., Sinreich, R., Ortega, I., Volkamer, R., Saiz-Lopez, A., Prados-Roman, C., Mahajan, A. S., and Ordóñez, C.: Iodine's impact on tropospheric oxidants: A global model study in GEOS-Chem, Atmospheric Chemistry and Physics, 16, 1161–1186, doi:10.5194/acp-16-1161-2016, 2016a.

Sherwen, T., Evans, M. J., Carpenter, L. J., Schmidt, J. A., and Mickely, L. J.: Halogen chemistry reduces tropospheric O_3 radiative forcing, Atmospheric Chemistry and Physics, pp. 1–18, doi:10.5194/acp-2016-688, 2016b.

Simpson, W. R., Brown, S. S., Saiz-Lopez, A., Thornton, J. A., and Von Glasow, R.: Tropospheric Halogen Chemistry: Sources, Cycling, and Impacts, Chemical Reviews, 115, 4035–4062, doi:10.1021/cr5006638, 2015.

Singh, H. B., Salas, L. J., Ridley, B. A., Shetter, J. D., Donahue, N. M., Fehsenfeld, F. C., Fahey, D. W., Parrish, D. D., Williams, E. J., Liu, S. C., Hübler, G., and Murphy, P. C.: Relationship between peroxyacetyl nitrate and nitrogen oxides in the clean troposphere, Nature, 318, 347–349, doi:10.1038/318347a0, 1985.

Singh, H. B., Kanakidou, M., Crutzen, P. J., and Jacob, D. J.: High concentrations and photochemical fate of oxygenated hydrocarbons in the global troposphere, Nature, 378, 50–54, doi:10.1038/378050a0, 1995.

Skalska, K., Miller, J. S., and Ledakowicz, S.: Trends in NO_x abatement: A review, Science of The Total Environment, 408, 3976–3989, doi:10.1016/j.scitotenv.2010.06.001, 2010.

Sommariva, R. and Von Glasow, R.: Multiphase halogen chemistry in the tropical atlantic ocean, Environmental Science & Technology, 46, 10 429–10 437, doi:10.1021/es300209f, 2012.

Sörgel, M., Regelin, E., Bozem, H., Diesch, J.-M., Drewnick, F., Fischer, H., Harder, H., Held, A., Hosaynali-Beygi, Z., Martinez, M., and Zetzsch, C.: Quantification of the unknown HONO daytime source and its relation to NO_2, Atmospheric Chemistry and Physics, 11, 10 433–10 447, doi:10.5194/acp-11-10433-2011, 2011.

Spataro, F. and Ianniello, A.: Sources of atmospheric nitrous acid: State of the science, current research needs, and future prospects, Journal of the Air & Waste Management Association, 64, 1232–1250, doi:10.1080/10962247.2014.952846, 2014.

Stark, H., Lerner, B. M., Schmitt, R., Jakoubek, R., Williams, E. J., Ryerson, T. B., Sueper, D. T., Parrish, D. D., and Fehsenfeld, F. C.: Atmospheric in situ measurement of nitrate radical (NO_3) and other photolysis rates using spectroradiometry and filter radiometry, Journal of Geophyscial Research, 112, 1–11, doi:10.1029/2006jd007578, 2007.

Stieb, D. M., Judek, S., and Burnett, R. T.: Meta-Analysis of Time-Series Studies of Air Pollution and Mortality: Effects of Gases and Particles and the Influence of Cause of Death, Age, and Season, Journal of the Air & Waste Management Association, 52, 470–484, doi:10.1080/10473289.2002.10470794, 2002.

Stutz, J., Alicke, B., Ackermann, R., Geyer, A., Wang, S., White, A. B., Williams, E. J., Spicer, C. W., and Fast, J. D.: Relative humidity dependence of HONO chemistry in urban areas, Journal of Geophysical Research, 109, D03 307, doi:10.1029/2003JD004135, 2004.

Stutz, J., Oh, H. J., Whitlow, S. I., Anderson, C., Dibb, J. E., Flynn, J. H., Rappenglück, B., and Lefer, B.: Simultaneous DOAS and mist-chamber IC measurements of HONO in Houston, TX, Atmospheric Environment, 44, 4090–4098, doi:10.1016/j.atmosenv.2009.02.003, 2010.

Su, H., Cheng, Y., Oswald, R., Behrendt, T., Trebs, I., Meixner, F. X., Andreae, M. O., Cheng, P., Zhang, Y., and Poschl, U.: Soil Nitrite as a Source of Atmospheric HONO and OH Radicals, Science, 333, 1616–1618, doi:10.1126/science.1207687, 2011.

Taira, M. and Kanda, Y.: Continuous generation system for low-concentration gaseous nitrous acid, Analytical Chemistry, 633, 630–633, doi:10.1021/ac00205a018, 1990.

Talukdar, R. K., Burkholder, J. B., Hunter, M., Gilles, M. K., Roberts, J. M., and Ravishankara, A. R.: Atmospheric fate of several alkyl nitrates Part 2: UV absorption cross-sections and photodissociation quantum yields, Journal of the Chemical Society, Faraday Transactions, 93, 2797–2805, doi:10.1039/a701781b, 1997.

Thornton, J. A., Wooldridge, P. J., and Cohen, R. C.: Atmospheric NO_2 : In Situ Laser-Induced Fluorescence Detection at Parts per Trillion Mixing Ratios, Analytical Chemistry, 72, 528–539, doi:10.1021/ac9908905, 2000.

Trebs, I., Mayol-Bracero, O. L., Pauliquevis, T., Kuhn, U., Sander, R., Ganzeveld, L., Meixner, F. X., Kesselmeier, J., Artaxo, P., and Andreae, M. O.: Impact of the Manaus urban plume on trace gas mixing ratios near the surface in the Amazon Basin: Implications for the NO-NO_2-O_3 photostationary state and peroxy radical levels, Journal of Geophyscial Research, 117, D05 307, doi:10.1029/2011JD016386, 2012.

Tuazon, E. C., Carter, W. P. L., and Atkinson, R.: Thermal decomposition of peroxyacetyl nitrate and reactions of acetyl peroxy radicals with NO and NO_2 over the temperature range 283-313 K, Journal of Physical Chemistry, 95, 2434–2437, doi:10.1021/j100159a059, 1991.

Tuzson, B., Zeyer, K., Steinbacher, M., McManus, J. B., Nelson, D. D., Zahniser, M. S., and Emmenegger, L.: Selective measurements of NO, NO_2 and NO_y in the free troposphere using quantum cascade laser spectroscopy, Atmospheric Measurement Techniques, 6, 927–936, doi:10.5194/amt-6-927-2013, 2013.

Val Martin, M., Honrath, R. E., Owen, R. C., and Li, Q. B.: Seasonal variation of nitrogen oxides in the central North Atlantic lower free troposphere, Journal of Geophysical Research, 113, D17 307, doi:10.1029/2007JD009688, 2008.

VandenBoer, T. C., Markovic, M. Z., Sanders, J. E., Ren, X., Pusede, S. E., Browne, E. C., Cohen, R. C., Zhang, L., Thomas, J., Brune, W. H., and Murphy, J. G.: Evidence for a nitrous acid (HONO) reservoir at the ground surface in Bakersfield, CA, during CalNex 2010, Journal of Geophyscial Research, 119, 9093–9106, doi:10.1002/2013jd020971, 2014.

Villena, G., Bejan, I., Kurtenbach, R., Wiesen, P., and Kleffmann, J.: Development of a new Long Path Absorption Photometer (LOPAP) instrument for the sensitive detection of NO_2 in the atmosphere, Atmospheric Measurement Techniques, 4, 1663–1676, doi:10.5194/amt-4-1663-2011, 2011.

Villena, G., Bejan, I., Kurtenbach, R., Wiesen, P., and Kleffmann, J.: Interferences of commercial NO_2 instruments in the urban atmosphere and in a smog chamber, Atmospheric Measurement Techniques, 5, 149–159, doi:10.5194/amt-5-149-2012, 2012.

Vogt, R., Sander, R., Von Glasow, R., and Crutzen, P. J.: Iodine chemistry and its role in halogen activation and ozone loss in the marine boundary layer: A model study, Journal of Atmospheric Chemistry, 32, 375–395, doi:10.1023/A:1006179901037, 1999.

Volkamer, R., Spietz, P., Burrows, J., and Platt, U.: High-resolution absorption cross-section of glyoxal in the UV-vis and IR spectral ranges, Journal of Photochemistry and Photobiology A: Chemistry, 172, 35–46, doi:10.1016/j.jphotochem.2004.11.011, 2005.

Volz-Thomas, A., Ptz, H.-W., Houben, N., Konrad, S., Mihelcic, D., Klpfel, T., and Perner, D.: Inorganic trace gases and peroxy radicals during BERLIOZ at Pabstthum: An investigation of the photostationary state of NO_x and O_3, Journal of Geophysical Research, 108, 8248, doi:10.1029/2001JD001255, 2003.

Wang, W. C., Liang, X. Z., Dudek, M. P., Pollard, D., and Thompson, S. L.: Atmospheric ozone as a climate gas, Atmospheric Research, 37, 247–256, doi:10.1016/0169-8095(94)00080-W, 1995.

Warneck, P. and Zerbach, T.: Synthesis of peroxyacetyl nitrate in air by acetone photolysis, Environmental Science & Technology, 26, 74–79, doi:10.1021/es00025a005, 1992.

Wayne, R., Barnes, I., Biggs, P., Burrows, J., Canosa-Mas, C., Hjorth, J., Bras, G. L., Moortgat, G., Perner, D., Poulet, G., Restelli, G., and Sidebottom, H.: The nitrate radical: Physics, chemistry, and the atmosphere, Atmospheric Environment. Part A. General Topics, 25, 1–203, doi:10.1016/0960-1686(91)90192-a, 1991.

Weber, B., Wu, D., Tamm, A., Ruckteschler, N., Rodríguez-Caballero, E., Steinkamp, J., Meusel, H., Elbert, W., Behrendt, T., Sörgel, M., Cheng, Y., Crutzen, P. J., Su, H., and Pöschl, U.: Biological soil crusts accelerate the nitrogen cycle through large NO and HONO emissions in drylands, Proceedings of the National Academy of Sciences, 112, 15 384–15 389, doi:10.1073/pnas.1515818112, 2015.

Whalley, L. K., Lewis, A. C., McQuaid, J. B., Purvis, R. M., Lee, J. D., Stemmler, K., Zellweger, C., and Ridgeon, P.: Two high-speed, portable GC systems designed for the measurement of non-methane hydrocarbons and PAN: results from the Jungfraujoch High Altitude Observatory., Journal of Environmental Monitoring, 6, 234–41, doi:10.1039/b310022g, 2004.

Whalley, L. K., Furneaux, K. L., Goddard, A., Lee, J. D., Mahajan, A., Oetjen, H., Read, K. A., Kaaden, N., Carpenter, L. J., Lewis, A. C., Plane, J. M. C., Saltzman, E. S., Wiedensohler, A., and Heard, D. E.: The chemistry of OH and HO_2 radicals in the boundary layer over the tropical Atlantic Ocean, Atmospheric Chemistry and Physics, 10, 1555–1576, doi:10.5194/acp-10-1555-2010, 2010.

Whalley, L. K., Blitz, M. A., Desservettaz, M., Seakins, P. W., and Heard, D. E.: Reporting the sensitivity of laser-induced fluorescence instruments used for HO_2 detection to an interference from RO_2 radicals and introducing a novel approach that enables HO_2 and certain RO_2 types to be selectively measured, Atmospheric Measurement Techniques, 6, 3425–3440, doi:10.5194/amt-6-3425-2013, 2013.

Williams, E. J., Baumann, K., Roberts, J. M., Bertman, S. B., Norton, R. B., Fehsenfeld, F. C., Sprinston, S. R., Nunnermacker, L. J., Newman, L., Olszyna, K., Meagher, J. F., Hartsell, B., Edgerton, E. S., Pearson, J. R., and Rodgers, M. O.: Intercomparison of ground-based NO_y measurement techniques, Journal of Geophysical Research, 103, 22 261–22 280, doi:10.1029/98JD00074, 1998.

Williams, J. E., Le Bras, G., Kukui, A., Ziereis, H., and Brenninkmeijer, C. A. M.: The impact of the chemical production of methyl nitrate from the NO + CH_3O_2 reaction on the global distributions of alkyl nitrates, nitrogen oxides and tropospheric ozone: a global modelling study, Atmospheric Chemistry and Physics, 14, 2363–2382, doi:10.5194/acp-14-2363-2014, 2014.

Winer, A. M., Peters, J. W., Smith, J. P., and Pitts Jr, J. N.: Response of Commercial Chemiluminescent NO-NO_2 , Analyzers to Other Nitrogen-Containing Compounds, Environmental Science & Technology, 8, 1118–1121, doi:10.1021/es60098a004, 1974.

Wojtal, P., Halla, J. D., and McLaren, R.: Pseudo steady states of HONO measured in the nocturnal marine boundary layer: A conceptual model for HONO formation on aqueous surfaces, Atmospheric Chemistry and Physics, 11, 3243–3261, doi:10.5194/acp-11-3243-2011, 2011.

Yang, J., Honrath, R. E., Peterson, M. C., Parrish, D. D., and Warshawsky, M.: Photostationary state deviation–estimated peroxy radicals and their implications for HO_x and ozone photochemistry at a remote northern Atlantic coastal site, Journal of Geophysical Research, 109, D02 312, doi:10.1029/2003JD003983, 2004.

Yang, X., Cox, R. A., Warwick, N. J., Pyle, J. A., Carver, G. D., O'Connor, F. M., and Savage, N. H.: Tropospheric bromine chemistry and its impacts on ozone: A model study, Journal of Geophysical Research, 110, D23 311, doi:10.1029/2005JD006244, 2005.

Ye, C., Gao, H., Zhang, N., and Zhou, X.: Photolysis of Nitric Acid and Nitrate on

Natural and Artificial Surfaces, Environmental Science & Technology, 50, 3530–3536, doi:10.1021/acs.est.5b05032, 2016a.

Ye, C., Zhou, X., Pu, D., Stutz, J., Festa, J., Spolaor, M., Tsai, C., Cantrell, C., Mauldin, R. L., Campos, T., Weinheimer, A., Hornbrook, R. S., Apel, E. C., Guenther, A., Kaser, L., Yuan, B., Karl, T., Haggerty, J., Hall, S., Ullmann, K., Smith, J. N., Ortega, J., and Knote, C.: Rapid cycling of reactive nitrogen in the marine boundary layer, Nature, 532, 489–491, doi:10.1038/nature17195, 2016b.

Ye, C., Heard, D. E., and Whalley, L. K.: Evaluation of Novel Routes for NO_x Formation in Remote Regions, Environmental Science & Technology, 51, 7442–7449, doi:10.1021/acs.est.6b06441, pMID: 28581733, 2017.

Zabielski, M. F., Seery, D. J., and Dodge, L. G.: Influence of mass transport and quenching on nitric oxide chemiluminescent analysis, Environmental Science & Technology, 18, 88–92, doi:10.1021/es00120a007, 1984.

Zhang, L., Wiebe, A., Vet, R., Mihele, C., O'Brien, J. M., Iqbal, S., and Liang, Z.: Measurements of reactive oxidized nitrogen at eight Canadian rural sites, Atmospheric Environment, 42, 8065–8078, doi:10.1016/j.atmosenv.2008.06.034, 2008.

Zhang, N., Zhou, X., Shepson, P. B., Gao, H., Alaghmand, M., and Stirm, B.: Aircraft measurement of HONO vertical profiles over a forested region, Geophysical Research Letters, 36, 1–5, doi:10.1029/2009GL038999, 2009.

Zhang, N., Zhou, X., Bertman, S., Tang, D., Alaghmand, M., Shepson, P. B., and Carroll, M. A.: Measurements of ambient HONO concentrations and vertical HONO flux above a northern Michigan forest canopy, Atmospheric Chemistry and Physics, 12, 8285–8296, doi:10.5194/acp-12-8285-2012, 2012.

Zhou, X., Beine, H. J., Honrath, R. E., Fuentes, J. D., Simpson, W., Shepson, P. B., and Bottenheim, J. W.: Snowpack Photochemical Production of HONO: a Major Source of OH in the Arctic Boundary Layer, Geophysical Research Letters, 28, 4087–4090, doi:10.1029/2001GL013531, 2001.

Zhou, X., Civerolo, K., Dai, H., Huang, G., Schwab, J., and Demerjian, K.: Summertime nitrous acid chemistry in the atmospheric boundary layer at a rural site

in New York State, Journal of Geophyscial Research, 107, ACH 13–1–ACH 13–11, doi:10.1029/2001JD001539, 2002.

Zhou, X., Gao, H., He, Y., Huang, G., Bertman, S., Civerolo, K., and Schwab, J.: Nitric acid photolysis on surfaces in low-NO_x environments: significant atmospheric implications, Geophysical Research Letters, 30, ASC 12/1–ASC 12/4, doi:10.1029/2003GL018620, 2003.